

THE SPECTROSCOPIC ANALYSIS OF VATERITE  
AND OTHER FORMS OF CALCIUM CARBONATE

CENTRE FOR NEWFOUNDLAND STUDIES

---

**TOTAL OF 10 PAGES ONLY  
MAY BE XEROXED**

(Without Author's Permission)

MARK JOSEPH HOLLETT







## **INFORMATION TO USERS**

This manuscript has been reproduced from the microfilm master. UMI films the text directly from the original or copy submitted. Thus, some thesis and dissertation copies are in typewriter face, while others may be from any type of computer printer.

**The quality of this reproduction is dependent upon the quality of the copy submitted. Broken or indistinct print, colored or poor quality illustrations and photographs, print bleedthrough, substandard margins, and improper alignment can adversely affect reproduction.**

In the unlikely event that the author did not send UMI a complete manuscript and there are missing pages, these will be noted. Also, if unauthorized copyright material had to be removed, a note will indicate the deletion.

Oversize materials (e.g., maps, drawings, charts) are reproduced by sectioning the original, beginning at the upper left-hand corner and continuing from left to right in equal sections with small overlaps.

Photographs included in the original manuscript have been reproduced xerographically in this copy. Higher quality 6" x 9" black and white photographic prints are available for any photographs or illustrations appearing in this copy for an additional charge. Contact UMI directly to order.

**Bell & Howell Information and Learning  
300 North Zeeb Road, Ann Arbor, MI 48106-1346 USA  
800-521-0600**

**UMI<sup>®</sup>**



National Library  
of Canada

Acquisitions and  
Bibliographic Services

395 Wellington Street  
Ottawa ON K1A 0N4  
Canada

Bibliothèque nationale  
du Canada

Acquisitions et  
services bibliographiques

395, rue Wellington  
Ottawa ON K1A 0N4  
Canada

*Your file* *Votre référence*

*Our file* *Notre référence*

The author has granted a non-exclusive licence allowing the National Library of Canada to reproduce, loan, distribute or sell copies of this thesis in microform, paper or electronic formats.

The author retains ownership of the copyright in this thesis. Neither the thesis nor substantial extracts from it may be printed or otherwise reproduced without the author's permission.

L'auteur a accordé une licence non exclusive permettant à la Bibliothèque nationale du Canada de reproduire, prêter, distribuer ou vendre des copies de cette thèse sous la forme de microfiche/film, de reproduction sur papier ou sur format électronique.

L'auteur conserve la propriété du droit d'auteur qui protège cette thèse. Ni la thèse ni des extraits substantiels de celle-ci ne doivent être imprimés ou autrement reproduits sans son autorisation.

0-612-54921-6

Canada

**The Spectroscopic Analysis of Vaterite  
and Other Forms of Calcium Carbonate**

By

Mark Joseph Hollett

A thesis submitted to the  
School of Graduate Studies  
in partial fulfillment of the  
requirements for the degree of  
Master of Science

Department of Chemistry  
Memorial University of Newfoundland

March, 2000

St. John's, Newfoundland

## **Abstract**

Precipitation of calcium carbonate from supersaturated solutions of  $\text{CaCl}_2$  with  $\text{K}_2\text{CO}_3$ ,  $\text{Na}_2\text{CO}_3$  and  $(\text{NH}_4)_2(\text{CO}_3)$  was studied in detail. In the course of our studies on the natural and synthetic vaterite forms of calcium carbonate, it has been possible to prepare, isolate and characterize the calcite, vaterite and aragonite forms of  $\text{CaCO}_3$ , as well as the hydrates,  $\text{CaCO}_3 \cdot 6\text{H}_2\text{O}$  and  $\text{CaCO}_3 \cdot 1\text{H}_2\text{O}$ . The precipitation reactions were found to be unexpectedly complex, with a number of different possible products. This is in contrast to the fact that calcite is the only thermodynamically stable solid in equilibrium with the saturated solution under ambient conditions.

The existence of each form was confirmed by various analytical and spectroscopic techniques. The crystalline forms, calcite, vaterite and aragonite, were characterized by such methods as differential scanning calorimetry (DSC), micro-Raman spectroscopy, Fourier-transform infrared spectroscopy (FT-IR), scanning electron microscopy (SEM), thermogravimetry with evolved gas analysis (TG-EGA) and powder X-ray diffraction (XRD), whereas the hydrated forms,  $\text{CaCO}_3 \cdot 6\text{H}_2\text{O}$  and  $\text{CaCO}_3 \cdot 1\text{H}_2\text{O}$ , were only characterized by DSC and Raman. It was also found that the various forms could be distinguished visually by the appearance of the solutions upon mixing and by the crystal habits observed under the microscope.

Optimum precipitation conditions were determined for the formation of each

polycrystalline form. The tendency for the metastable phases to precipitate from various aqueous, supersaturated solutions was dependent upon factors such as the temperature, concentration of reactants, duration of precipitation, as well as the stirring rate. However, it has been determined through the course of several repeated experiments that these kinetically-controlled precipitations were mainly dependent upon the temperature and the initial concentrations of the reactants.

Raman and infrared spectroscopic studies of natural and synthetic vaterite indicate an extremely complicated crystal structure in which the carbonate ions appear to occupy a number of different crystallographic sites. The spectroscopic results are consistent with the structure reported by Meyer (1969). However, we suggest that the disordered stacking sequence is not random over the 12 carbonates of the unit cell, but rather follows a pattern characteristic to that of an incommensurate phase. A detailed unit cell group analysis was not possible because the vibrational spectrum is further complicated by intermolecular coupling of carbonate ions on different lattice sites. Raman and infrared spectra for the regions of the internal modes of the carbonate ions indicate that the different sites fall into three major groups with differing occupancies. For example, in the  $\nu_1$  region, three peaks were observed at 1075.0, 1081.4 and 1090.9  $\text{cm}^{-1}$  with relative intensities 0.40:0.19:1.00. These multiple site effects were confirmed by studies of  $^{18}\text{O}$  and  $^{13}\text{C}$  carbonate impurities. It would appear that the vaterite structure is similar to the incommensurate phase of  $\gamma\text{-Na}_2\text{CO}_3$ . Trace amounts of water were detected in the freshly prepared vaterite, but are not believed to be necessary for kinetic stability. Laser fluorescence measurements were also employed to estimate the

concentration of manganese(II) impurities in the precipitates.

This research has permitted clarification of previous studies and has led to a more in-depth understanding of the mechanism of metastable crystal growth.

## **Acknowledgments**

I am very grateful to Dr. Murray H. Brooker for his excellent knowledge of Raman and infrared spectroscopy, fruitful guidance, friendship, timely encouragement and financial support.

I am grateful to Dr. Peter Tremaine for his advice and the use of his laboratory.

I am also grateful to Dr. Roger A. Mason for his advice.

I would like to thank the Chemistry Department for the use of their differential scanning calorimeter and Fourier-transform infrared spectrometer.

I would like to thank Dr. Kim Kasperski and CWRC-Natural Resources Canada for the use of their thermogravimeter.

I would like to thank the Biology Department for the use of their scanning electron microscope.

I would like to thank the Earth Sciences Department for the use of their X-ray diffractometer.

I would like to thank Mr. Gary Hancock for his advise and friendship.

I would also like to thank the Chemistry Department and Graduate Studies at Memorial University of Newfoundland for financial support.

## Table of Contents

<b>Abstract</b>	.....(ii)
<b>Acknowledgments</b>	.....(v)
<b>List of Tables</b>	.....(xi)
<b>List of Figures</b>	.....(xiii)
<b>List of Abbreviations and Symbols Used</b>	.....(xxii)
<b>Chapter 1 Introduction</b>	.....(1)
1.1 The Phases of Calcium Carbonate and its Hydrates	.....(2)
1.2 Problems with the Preparation and Analysis of the Several Forms	...(3)
1.3 Advances in Spectroscopic Techniques as Related to Vaterite	...(4)
1.4 The Possible Incommensurate Phase of Calcium Carbonate	.....(6)
<b>Chapter 2 Experimental</b>	.....(8)
2.1 The Preparation of $\text{CaCO}_3 \cdot 6\text{H}_2\text{O}$	.....(9)
2.2 The Preparation of $\text{CaCO}_3 \cdot 1\text{H}_2\text{O}$	.....(9)
2.3 The Preparation of Calcite	.....(10)
2.4 The Preparation of Vaterite	.....(10)
2.5 The Preparation of Aragonite	.....(10)
2.6 Raman Spectroscopic Measurements	.....(11)
2.7 Infrared Spectroscopic Measurements	.....(12)

2.8	<b>Morphological Investigations</b>	.....(13)
2.9	<b>Thermoanalytical Measurements</b>	.....(14)
2.10	<b>Structural Investigations</b>	.....(15)
<b>Chapter 3 Theory</b>		.....(16)
3.1	<b>Phase Transformations</b>	.....(16)
3.1.1	<b>Thermodynamic/Macroscopic Concepts: Transformation Orders</b>	.....(16)
3.1.1.1	<b>First-Order Transformations</b>	.....(17)
3.1.1.2	<b>Second-Order Transformations</b>	.....(17)
3.1.1.3	<b>Lambda-Order Transformations</b>	.....(18)
3.1.2	<b>Structural/Microscopic Considerations</b>	.....(18)
3.1.2.1	<b>Displacive Phase Transformations</b>	.....(19)
3.1.2.2	<b>Reconstructive Phase Transformations</b>	.....(19)
3.1.2.3	<b>Order-Disorder Phase Transformations</b>	.....(20)
3.1.3	<b>Kinetic Theory of Phase Transformations</b>	.....(20)
3.1.3.1	<b>Thermodynamics of Metastable Phases</b>	.....(21)
3.1.3.2	<b>Precipitation of Metastable Phases</b>	.....(22)
3.1.4	<b>Experimental Methods Used to Study Phase Transformations.</b>	(23)
3.1.4.1	<b>Thermal Investigations</b>	.....(24)
3.1.4.2	<b>Spectroscopic Studies</b>	.....(24)
3.1.4.3	<b>Diffraction Studies</b>	.....(24)



4.2.2	<b>Morphological Studies</b>	.....(55)
4.2.3	<b>Raman Spectroscopic Data</b>	.....(55)
4.2.4	<b>Thermoanalytical Measurements</b>	.....(57)
4.3	<b>Calcite</b>	.....(57)
4.3.1	<b>Preparation</b>	.....(57)
4.3.2	<b>Morphological Studies</b>	.....(58)
4.3.3	<b>Raman Spectroscopic Data</b>	.....(58)
4.4	<b>Vaterite</b>	.....(59)
4.4.1	<b>Preparation</b>	.....(59)
4.4.2	<b>Morphological Studies</b>	.....(60)
4.4.3	<b>Raman Spectroscopic Data</b>	.....(60)
4.4.4	<b>Thermoanalytical Measurements</b>	.....(61)
4.5	<b>Aragonite</b>	.....(61)
4.5.1	<b>Preparation</b>	.....(61)
4.5.2	<b>Morphological Studies</b>	.....(62)
4.5.3	<b>Raman Spectroscopic Data</b>	.....(62)
4.6	<b>A Detailed Spectroscopic Analysis of Vaterite</b>	.....(62)
4.6.1	<b>External Lattice Modes</b>	.....(63)
4.6.2	<b>Internal Vibrational Modes</b>	.....(64)
	4.6.2.1 $\nu_4$ - Antisymmetric Bend	.....(64)
	4.6.2.2 $\nu_2$ - Out-of-Plane Deformation	.....(65)

4.6.2.3 $\nu_1$ - Symmetric Stretch	.....(66)
4.6.2.4 $\nu_3$ - Antisymmetric Stretch	.....(69)
4.6.2.5 $2\nu_2$ - Overtone of The Out-of-Plane Deformation	
Mode ( $\nu_2$ )	.....(69)
4.6.2.6 $[\nu_4+\nu_1]$ - Combination Band	.....(70)
4.6.2.7 Water and Manganese(II) Impurities	.....(70)
<b>Chapter 5 Conclusions</b>	.....(152)
<b>Bibliography</b>	.....(155)

## List of Tables

Table 3.1	Character table for the $D_{2h}^{16}$ space group of aragonite	.....(37)
Table 3.2	Table used to correlate the site symmetry of the calcium ions ( $C_2$ ), as well as the carbonate ions ( $C_3$ ), to the symmetry of the unit cell ( $D_{2h}$ ) in aragonite	.....(38)
Table 3.3	Table used to correlate the point group symmetry of the free carbonate ions ( $D_{3h}$ ) to their site symmetry ( $C_3$ ) in aragonite	...(39)
Table 3.4	Character table for the $D_{3d}^6$ space group of calcite	.....(40)
Table 3.5	Table used to correlate the site symmetry of the calcium ions ( $S_6$ ) to the symmetry of the unit cell ( $D_{3d}$ ) in calcite	.....(41)
Table 3.6	Table used to correlate the point group symmetry of the free carbonate ions ( $D_{3h}$ ) to their site symmetry ( $D_3$ ) in calcite	.....(42)
Table 3.7	Table used to correlate the site symmetry of the carbonate ions ( $D_3$ ) to the symmetry of the unit cell ( $D_{3d}$ ) in calcite	.....(43)
Table 4.1	Observed Raman vibrational frequencies ( $cm^{-1}$ ) for $CaCO_3 \cdot 6H_2O$ at 25 °C	.....(73)
Table 4.2	DSC analysis results for the dehydration reaction: $CaCO_3 \cdot 6H_2O \rightarrow CaCO_3 \cdot 1H_2O$	.....(74)
Table 4.3	Observed Raman vibrational frequencies ( $cm^{-1}$ ) for $CaCO_3 \cdot 1H_2O$	

	at 25 °C .....	(75)
Table 4.4	<b>DSC analysis results for the transformation reaction:</b>	
	<b>CaCO<sub>3</sub>·1H<sub>2</sub>O → vaterite .....</b>	<b>(76)</b>
Table 4.5	<b>Observed Raman vibrational frequencies (cm<sup>-1</sup>) for calcite at 25 °C</b>	
	<b>and comparison with literature .....</b>	<b>(77)</b>
Table 4.6	<b>DSC analysis results for the polymorphic transformation reaction:</b>	
	<b>vaterite – calcite .....</b>	<b>(78)</b>
Table 4.7	<b>Observed Raman vibrational frequencies (cm<sup>-1</sup>) for aragonite at</b>	
	<b>25 °C and comparison with literature .....</b>	<b>(79)</b>
Table 4.8	<b>Observed Raman vibrational frequencies (cm<sup>-1</sup>) for vaterite at</b>	
	<b>25 °C and comparison with literature .....</b>	<b>(80)</b>
Table 4.9	<b>Observed infrared vibrational frequencies (cm<sup>-1</sup>) for vaterite at</b>	
	<b>25 °C and comparison with literature .....</b>	<b>(81)</b>

## List of Figures

- Figure 3.1 Reaction profile diagram showing how the potential energy of the reactant(s) change during the course of a chemical reaction .....(44)
- Figure 3.2 Schematic representation (Adapted from Tolédano and Tolédano, 1987) of the distinguishing features of an incommensurate phase ...(45)
- Figure 3.3 Correlation between the site symmetry of the calcium ions ( $C_5$ ) and the symmetry of the unit cell ( $D_{2h}$ ) in aragonite .....(46)
- Figure 3.4 Correlation (external vibrational modes only) between the point group symmetry of the free carbonate ions ( $D_{3h}$ ), their site symmetry ( $C_5$ ) and the symmetry of the unit cell ( $D_{2h}$ ) in aragonite .....(47)
- Figure 3.5 Correlation (internal vibrational modes only) between the point group symmetry of the free carbonate ions ( $D_{3h}$ ), their site symmetry ( $C_5$ ) and the symmetry of the unit cell ( $D_{2h}$ ) in aragonite .....(48)
- Figure 3.6 Correlation between the site symmetry of the calcium ions ( $S_6$ ) and the symmetry of the unit cell ( $D_{3d}$ ) in calcite .....(49)
- Figure 3.7 Correlation (external vibrational modes only) between the point group symmetry of the free carbonate ions ( $D_{3h}$ ), their site symmetry ( $D_3$ ) and the symmetry of the unit cell ( $D_{3d}$ ) in calcite .....(50)
- Figure 3.8 Correlation (internal vibrational modes only) between the point

group symmetry of the free carbonate ions ( $D_{3h}$ ), their site symmetry ( $D_3$ ) and the symmetry of the unit cell ( $D_{3d}$ ) in calcite .....(51)

Figure 4.1 Photomicrograph (10x magnification) of  $\text{CaCO}_3 \cdot 6\text{H}_2\text{O}$  collected immediately after the precipitation showing the hexagonal shape of the crystals .....(82)

Figure 4.2 Photomicrograph (50x magnification) of  $\text{CaCO}_3 \cdot 6\text{H}_2\text{O}$  collected immediately after the precipitation showing the hexagonal shape of the crystals .....(83)

Figure 4.3 Raman spectrum of the external lattice mode region and  $\nu_4$  internal vibrational mode region of  $\text{CaCO}_3 \cdot 6\text{H}_2\text{O}$  at 25 °C .....(84)

Figure 4.3a Curve fit of the Raman spectrum of the wagging vibrations of water and the  $\nu_4$  internal vibrational mode region of  $\text{CaCO}_3 \cdot 6\text{H}_2\text{O}$  at 25 °C .....(85)

Figure 4.4 Raman spectrum of the  $\nu_1$  internal vibrational mode region of  $\text{CaCO}_3 \cdot 6\text{H}_2\text{O}$  at 25 °C .....(86)

Figure 4.4a Curve fit of the Raman spectrum of the  $\nu_1$  internal vibrational mode region of  $\text{CaCO}_3 \cdot 6\text{H}_2\text{O}$  at 25 °C .....(87)

Figure 4.5 Raman spectrum of the  $\nu_3$  internal vibrational mode region and  $2\nu_2$  overtone region of  $\text{CaCO}_3 \cdot 6\text{H}_2\text{O}$ , as well as the  $\nu_2$  region of water, at 25 °C .....(88)

Figure 4.5a Curve fit of the Raman spectrum of the  $\nu_3$  internal vibrational mode

	region and $2\nu_2$ overtone region of $\text{CaCO}_3 \cdot 6\text{H}_2\text{O}$ , as well as the $\nu_2$ region of water, at 25 °C .....	(89)
Figure 4.6	Overview Raman spectrum of $\text{CaCO}_3 \cdot 6\text{H}_2\text{O}$ at 25 °C displaying the region from 1000-4000 $\text{cm}^{-1}$ .....	(90)
Figure 4.6a	Raman spectrum of the O-H stretching region of $\text{CaCO}_3 \cdot 6\text{H}_2\text{O}$ at 25 °C .....	(91)
Figure 4.6b	Curve fit of the Raman spectrum of the O-H stretching region of $\text{CaCO}_3 \cdot 6\text{H}_2\text{O}$ at 25 °C .....	(92)
Figure 4.7	DSC analysis spectrum for the dehydration reaction, $\text{CaCO}_3 \cdot 6\text{H}_2\text{O} \rightarrow \text{CaCO}_3 \cdot \text{H}_2\text{O}$ , from 25-120 °C at a rate of 10 °C/minute .....	(93)
Figure 4.8	Photomicrograph (20x magnification) of $\text{CaCO}_3 \cdot \text{H}_2\text{O}$ produced by dehydration of $\text{CaCO}_3 \cdot 6\text{H}_2\text{O}$ showing the cloudy appearance and distorted, hexagonal shape of the crystals .....	(94)
Figure 4.9	Raman spectrum of the external lattice mode region and $\nu_4$ internal vibrational mode region of $\text{CaCO}_3 \cdot \text{H}_2\text{O}$ at 25 °C .....	(95)
Figure 4.9a	Curve fit of the Raman spectrum of the $\nu_4$ internal vibrational mode region of $\text{CaCO}_3 \cdot \text{H}_2\text{O}$ at 25 °C .....	(96)
Figure 4.10	Raman spectrum of the $\nu_1$ internal vibrational mode region of $\text{CaCO}_3 \cdot \text{H}_2\text{O}$ at 25 °C .....	(97)
Figure 4.10a	Curve fit of the Raman spectrum of the $\nu_1$ internal vibrational mode	

	region of $\text{CaCO}_3 \cdot \text{H}_2\text{O}$ at 25 °C .....	(98)
Figure 4.11	Raman spectrum of the $\nu_3$ internal vibrational mode region and $2\nu_2$ overtone region of $\text{CaCO}_3 \cdot \text{H}_2\text{O}$ , as well as the $\nu_2$ region of water, at 25 °C .....	(99)
Figure 4.11a	Curve fit of the Raman spectrum of the $\nu_3$ internal vibrational mode region and $2\nu_2$ overtone region of $\text{CaCO}_3 \cdot \text{H}_2\text{O}$ , as well as the $\nu_2$ region of water, at 25 °C .....	(100)
Figure 4.12	Overview Raman spectrum of $\text{CaCO}_3 \cdot \text{H}_2\text{O}$ at 25 °C displaying the region from 1000-4000 $\text{cm}^{-1}$ .....	(101)
Figure 4.12a	Raman spectrum of the O-H stretching region of $\text{CaCO}_3 \cdot \text{H}_2\text{O}$ at 25 °C .....	(102)
Figure 4.12b	Curve fit of the Raman spectrum of the O-H stretching region of $\text{CaCO}_3 \cdot \text{H}_2\text{O}$ at 25 °C .....	(103)
Figure 4.13	SEM micrograph of $\text{CaCO}_3$ collected 24 hours after the precipitation, showing calcite rhombs associated with spherulites of vaterite .....	(104)
Figure 4.14	SEM micrograph of calcite prepared by the transformation reactions, $\text{CaCO}_3 \cdot 6\text{H}_2\text{O} \rightarrow \text{CaCO}_3 \cdot \text{H}_2\text{O} \rightarrow \text{calcite}$ , showing the well-defined, hexagonal shape of the crystals .....	(105)
Figure 4.15	Overview Raman spectrum of calcite at 25 °C displaying the region from 100-1150 $\text{cm}^{-1}$ .....	(106)

Figure 4.16	Raman spectrum of the $\nu_3$ internal vibrational mode region and $2\nu_2$ overtone region of calcite at 25 °C .....	(107)
Figure 4.17	Photomicrograph (20x magnification) of vaterite removed immediately after the precipitation showing the spherical shape of the aggregated crystals .....	(108)
Figure 4.18	Photomicrograph (50x magnification) of vaterite removed immediately after the precipitation showing the spherical shape of the aggregated crystals .....	(109)
Figure 4.19	SEM micrograph (low magnification) of vaterite removed immediately after the precipitation showing the spherical shape of the aggregated crystals .....	(110)
Figure 4.20	SEM micrograph (high magnification) of vaterite removed immediately after the precipitation showing the spherical shape of the aggregated crystals .....	(111)
Figure 4.21	Overview Raman spectrum of vaterite at 25 °C displaying the region from 100-1150 $\text{cm}^{-1}$ .....	(112)
Figure 4.22	Raman spectrum of the $\nu_3$ internal vibrational mode region and $2\nu_2$ overtone region of vaterite at 25 °C .....	(113)
Figure 4.23	DSC analysis spectrum for the polymorphic transformation reaction, vaterite $\rightarrow$ calcite, from 25-550 °C at a rate of 10 °C/minute .....	(114)
Figure 4.24	Overview Raman spectra of vaterite performed before [a] (note the	

	presence of the water band at $\approx 3400\text{ cm}^{-1}$ ) and after [b] heating to $220\text{ }^{\circ}\text{C}$ , showing the removal of water and the increase in fluorescence due to manganese(II) impurities .....	(115)
Figure 4.24a	Raman spectra of the $\nu_1$ internal vibrational mode region of vaterite performed before [a] and after [b] heating to $220\text{ }^{\circ}\text{C}$ .....	(116)
Figure 4.25	Photomicrograph (20x magnification) of aragonite removed immediately after the precipitation showing the "needle-like" shape of the crystals .....	(117)
Figure 4.26	Photomicrograph (50x magnification) of aragonite removed immediately after the precipitation showing the "needle-like" shape of the crystals .....	(118)
Figure 4.27	Overview Raman spectrum of aragonite at $25\text{ }^{\circ}\text{C}$ displaying the region from $100\text{-}1150\text{ cm}^{-1}$ .....	(119)
Figure 4.28	Raman spectrum of the $\nu_3$ internal vibrational mode region and $2\nu_2$ overtone region of aragonite at $25\text{ }^{\circ}\text{C}$ .....	(120)
Figure 4.29	Raman spectrum of the external lattice mode region of vaterite at $25\text{ }^{\circ}\text{C}$ .....	(121)
Figure 4.29a	Curve fit of the Raman spectrum of the external lattice mode region of vaterite at $25\text{ }^{\circ}\text{C}$ .....	(122)
Figure 4.30	Raman spectrum of the $\nu_4$ internal vibrational mode region of vaterite at $25\text{ }^{\circ}\text{C}$ .....	(123)

Figure 4.30a	Curve fit of the Raman spectrum of the $\nu_4$ internal vibrational mode region of vaterite at 25 °C	.....(124)
Figure 4.31	Infrared spectrum of the $\nu_4$ internal vibrational mode region (lower $\text{cm}^{-1}$ region) of vaterite at 25 °C	.....(125)
Figure 4.31a	Curve fit of the infrared spectrum of the $\nu_4$ internal vibrational mode region (lower $\text{cm}^{-1}$ region) of vaterite at 25 °C	.....(126)
Figure 4.32	Infrared spectrum of the $\nu_4$ internal vibrational mode region (higher $\text{cm}^{-1}$ region) of vaterite at 25 °C	.....(127)
Figure 4.32a	Curve fit of the infrared spectrum of the $\nu_4$ internal vibrational mode region (higher $\text{cm}^{-1}$ region) of vaterite at 25 °C	.....(128)
Figure 4.33	Raman spectrum of the $\nu_2$ internal vibrational mode region of vaterite at 25 °C	.....(129)
Figure 4.33a	Curve fit of the Raman spectrum of the $\nu_2$ internal vibrational mode region of vaterite at 25 °C	.....(130)
Figure 4.34	Infrared spectrum of the $\nu_2$ internal vibrational mode region of vaterite at 25 °C	.....(131)
Figure 4.34a	Curve fit of the infrared spectrum of the $\nu_2$ internal vibrational mode region of vaterite at 25 °C	.....(132)
Figure 4.35	Infrared spectrum of the $^{13}\text{C}$ region of the $\nu_2$ internal vibrational mode region of vaterite at 25 °C	.....(133)
Figure 4.36	Raman spectrum of the $\nu_1$ internal vibrational mode region of	

	vaterite at 25 °C	.....(134)
Figure 4.36a	Curve fit of the Raman spectrum of the $\nu_1$ internal vibrational mode region of vaterite at 25 °C	.....(135)
Figure 4.37	Infrared spectrum of the $\nu_1$ internal vibrational mode region of vaterite at 25 °C	.....(136)
Figure 4.37a	Curve fit of the infrared spectrum of the $\nu_1$ internal vibrational mode region of vaterite at 25 °C	.....(137)
Figure 4.38	Raman spectrum of the $^{18}\text{O}$ region of the $\nu_1$ internal vibrational mode region of vaterite at 25 °C	.....(138)
Figure 4.39	Raman spectrum of the $\nu_3$ internal vibrational mode region of vaterite at 25 °C	.....(139)
Figure 4.39a	Curve fit of the Raman spectrum of the $\nu_3$ internal vibrational mode region of vaterite at 25 °C	.....(140)
Figure 4.40	Infrared spectrum of the $\nu_3$ internal vibrational mode region of vaterite at 25 °C	.....(141)
Figure 4.40a	Curve fit of the infrared spectrum of the $\nu_3$ internal vibrational mode region of vaterite at 25 °C	.....(142)
Figure 4.41	Raman spectrum of the $2\nu_2$ overtone region of vaterite at 25 °C	...(143)
Figure 4.41a	Curve fit of the Raman spectrum of the $2\nu_2$ overtone region of vaterite at 25 °C	.....(144)
Figure 4.42	Infrared spectrum of the $[\nu_4+\nu_1]$ combination band region of	

	vaterite at 25 °C	.....(145)
Figure 4.42a	Infrared spectrum of the $[\nu_4+\nu_1]$ combination band region (lower $\text{cm}^{-1}$ region) of vaterite at 25 °C	.....(146)
Figure 4.42b	Curve fit of the infrared spectrum of the $[\nu_4+\nu_1]$ combination band region (lower $\text{cm}^{-1}$ region) of vaterite at 25 °C	.....(147)
Figure 4.42c	Infrared spectrum of the $[\nu_4+\nu_1]$ combination band region (higher $\text{cm}^{-1}$ region) of vaterite at 25 °C	.....(148)
Figure 4.42d	Curve fit of the infrared spectrum of the $[\nu_4+\nu_1]$ combination band region (higher $\text{cm}^{-1}$ region) of vaterite at 25 °C	.....(149)
Figure 4.43	Infrared spectra of spectroscopically pure KBr alone [a], and in combination with vaterite [b], showing the presence and relative amount of water impurities	.....(150)
Figure 4.44	Overview Raman spectra of calcite performed before [a] (note the presence of the water band at $\approx 3400 \text{ cm}^{-1}$ ) and after [b] heating to 220 °C, showing the removal of water and the increase in fluorescence due to manganese(II) impurities	.....(151)

## List of Abbreviations and Symbols Used

$a_{\text{Ca}^{2+}}$	-	activity of the calcium ion.
$a_{\text{CO}_3^{2-}}$	-	activity of the carbonate ion.
a, b, c	-	unit cell edge lengths.
$a^*$ , $b^*$ , $c^*$	-	reciprocal point translations corresponding to a, b and c respectively.
CCD	-	charge coupled device.
$C_p$	-	specific heat capacity.
DSC	-	differential scanning calorimetry.
FT-IR	-	Fourier-transform infrared.
FWHH	-	full width at half height.
G	-	Gibb's free energy.
$\Delta G_a$	-	free energy of activation.
H	-	enthalpy.
$H_t$	-	enthalpy at the transformation temperature.
$h, k, l$	-	integers in a Miller index.
k	-	wave vector.
K	-	kelvin.
$m$	-	integer.

N	-	number of atoms.
P	-	pressure.
PMT	-	photo-multiplier tube.
Q	-	supersaturation activity product.
$q_i$	-	temperature-based coordinate.
r	-	equilibrium bond length.
S	-	entropy.
S	-	supersaturation state.
SEM	-	scanning electron microscopy.
S/N	-	signal-to-noise.
T	-	temperature.
TG	-	thermogravimeter.
TG-EGA	-	thermogravimetry with evolved gas analysis.
$T_{INC}$	-	incommensurate phase transition temperature.
$T_{Lock-in}$	-	lock-in phase transition temperature.
$T_\lambda$	-	lambda-point temperature.
V	-	molar volume.
XRD	-	X-ray diffraction.
Z	-	number of formula units present in the unit cell.
$\alpha$	-	coefficient of thermal expansion.
$\overset{z}{\alpha}$	-	polarizability tensor.

$\beta$	-	isothermal compressibility factor.
$\gamma$	-	mean activity coefficient of a divalent ion.
$\Delta$	-	change.
$K_{\text{calcite}}$	-	solubility product of calcite.
$K_{\text{sp}}$	-	solubility product.
$\vec{\mu}$	-	dipole moment vector.
$\nu$	-	frequency in wavenumbers ( $\text{cm}^{-1}$ ).

# **Chapter 1**

## **Introduction**

Calcium carbonate is a very common, but important mineral. It is the principle chemical component of limestone and exists in small amounts in most rocks. Surface  $\text{CaCO}_3$  is one of the more dynamic minerals since it dissolves and reforms in normal weathering reactions. Different polymorphic modifications are formed naturally as the minerals vaterite and aragonite, as well various hydrates may precipitate under appropriate conditions (Blackburn and Dennen, 1994; Putnis, 1992). With the ever increasing levels of  $\text{CO}_2$  in the atmosphere, there is the hope that  $\text{CaCO}_3$  may act as a natural sink to immobilize atmospheric  $\text{CO}_2$  (Maciejewski *et al.*, 1994). Formation of  $\text{CaCO}_3$  by living organisms is a major source of calcite and aragonite forms of limestone. Calcium carbonate in different modifications has been identified in human gallstones, otoconia of sharks, otoliths of fish, avian eggshells and mollusk shells (Chakraborty *et al.*, 1994; Gaudie, 1993; Gaudie<sup>1</sup>, 1996; Gaudie<sup>2</sup>, 1996; Gaudie *et al.*, 1997; Nassrallah-Aboukaïs *et al.*, 1998). The commercial importance of  $\text{CaCO}_3$  is also well-known as it is a basic raw material in the manufacture of paints, textiles, rubbers, mortars and concretes (Chakraborty *et al.*, 1994). In industrial boilers and water cooling systems, the deposition of  $\text{CaCO}_3$ , commonly known as scale formation, leads to decreased system efficiencies and an increased need for the frequency of chemical cleaning (Brooks *et al.*, 1950; Simpson, 1998). In order to achieve effective scale inhibition, chemical

additives are required and considerable research has to be undertaken to elucidate the mechanism of the formation, growth and stability of the various forms of  $\text{CaCO}_3$ .

In the present work, the solubility, precipitation and stability of the several forms of calcium carbonate were investigated. The DSC analyses and vibrational spectra of the hydrates encountered in the precipitation reactions were also studied, as well as a detailed spectroscopic analysis of vaterite.

### **1.1 The Phases of Calcium Carbonate and its Hydrates**

Calcium carbonate exhibits polymorphism. At ordinary temperatures and pressures, it occurs in three distinct, anhydrous crystalline forms. The two most well-known forms are calcite and aragonite, but there is also a less common form known as vaterite, or  $\mu\text{-CaCO}_3$ . All three exist in nature as naturally occurring minerals, but calcite and aragonite have received much more extensive research than has vaterite. Even though vaterite has been classified as a distinct form of calcium carbonate that is easily prepared in the laboratory, there is little information available on the factors governing its precipitation in pure form, without calcite impurities (Maciejewski *et al.*, 1994).

At temperatures near  $0^\circ\text{C}$ , calcium carbonate hexahydrate occurs in the form of well-defined hexagonal crystals. For  $\text{CaCO}_3 \cdot 6\text{H}_2\text{O}$ , information on its properties has already been established in the literature such as the crystallographic data (Johnston *et al.*, 1916), powder X-ray diffraction pattern (Brooks *et al.*, 1950) and the density (Mackenzie, 1923).

Calcium carbonate monohydrate, or amorphous calcium carbonate (Brooks *et al.*, 1950), exists at temperatures below  $25^\circ\text{C}$  and occurs in the form of relatively distorted

hexagonal crystals. Even though the X-ray powder pattern (Brooks *et al.*, 1950) has already been determined, there is still much confusion as to the crystal structure and properties.

Two other possible hydrates,  $\text{CaCO}_3 \cdot 5\text{H}_2\text{O}$ , or hydrocalcite, and  $\text{CaCO}_3 \cdot 3\text{H}_2\text{O}$ , or subhydrocalcite, have been proposed (Copisarow, 1923), but no microscopic or visible evidence, or spectroscopic or X-ray data were reported.

## **1.2 Problems with the Preparation and Analysis of the Several Forms**

A number of methods for the preparation of the various forms of calcium carbonate have been proposed. Some methods involved the addition of chemical reagents such as calgon (Brooks *et al.*, 1951), a glassy form of sodium phosphate, while others involved the addition of compounds such as KOH,  $\text{MgCl}_2 \cdot 6\text{H}_2\text{O}$  and NaCl (Johnston *et al.*, 1916), HCl and NaOH (Kralj *et al.*, 1997), sucrose (Mackenzie, 1923) and amino or carboxyl group organic derivatives (Matsushita *et al.*, 1996). Unfortunately, these methods tended to be unreliable and have led to inconsistent results because of the complexity caused by the effects of additives on the precipitation process.

The form of  $\text{CaCO}_3$  that precipitates from aqueous solutions of  $\text{Ca}^{2+}$  and  $\text{CO}_3^{2-}$  ions depends on many factors. Not only are the temperature, pressure and concentrations of the reactants important, but there are other contributing factors such as the stirring rate, Oswald ripening and filtration speed, absorbed and trapped surface impurities, and humidity. The form that precipitates initially is determined by the first crystal to nucleate. Therefore, the formation of each nucleus will be determined by a set of unique parameters from those listed above.

The inconsistency and unreliability of these methods is also evident in the analysis of

the calcium carbonate forms. In particular, the XRD patterns of vaterite obtained by these methods had been very difficult to analyse because the diffraction peaks of impurities, such as calcite (Perić *et al.*, 1996) and calgon (Brooks *et al.*, 1950), have appeared along with the diffraction peaks of the vaterite.

In the majority of experiments, large crystals are preferred. However, the size of the precipitated crystal is dependent upon the degree of supersaturation at the time precipitation begins. The greater the extent of supersaturation the smaller the crystals. Consequently, the concentrations of the reactants, Oswald ripening and filtration speed and stirring rate can affect the size of the resulting crystals. This problem of the formation of small crystals is evident in the isolation of vaterite. In order to obtain vaterite in pure form, without other calcium carbonate phase impurities, the precipitation must be relatively fast because the longer the vaterite nuclei are in contact with the aqueous medium, then the greater is the probability of obtaining unwanted nuclei such as calcite. Growth of vaterite crystals of sufficient size for single crystal X-ray analysis is experimentally precluded.

As a result of the inconsistent results reported, it is evident that reliable methods of preparation need to be established, together with an assessment of the factors that affect the precipitation of each phase of calcium carbonate in relatively pure form.

### **1.3 Advances in Spectroscopic Techniques as Related to Vaterite**

Raman and infrared spectroscopic studies are very useful in the analysis of alkaline earth metal carbonates because the carbonate ion is able to serve as a very sensitive probe for the nature of the various cationic environments. From previous studies of the different  $\text{CaCO}_3$

phases, it has been observed that the carbonate ion is uniquely perturbed by the different cationic environments and different cation coordination numbers. As a consequence of this perturbation, the vibrational bands of the free carbonate ion were found to be shifted and/or broadened, the degeneracy of the doubly-degenerate  $E'$  modes lifted and bands of other non-degenerate modes often showed multi-peak and/or asymmetric features.

Raman and infrared are complementary methods used to obtain the vibrational frequencies of normal modes of molecules and crystals. The selection rules are different because Raman activity is dependent on the change in the polarizability of the molecule ( $\partial \alpha^z / \partial q_i$ ), while infrared activity is dependent on the change in the dipole moment ( $\partial \vec{\mu} / \partial q_i$ ). These differences are well-described in many texts (Farmer, 1974; Iqbal, 1984; Laserna, 1996; Turrell, 1972). In the majority of instances, the use of Raman spectroscopy is now preferred over the use of infrared for several reasons. Raman-active bands tend to be narrower than those in the infrared. Raman microprobe spectrometers permit the collection of spectra faster than with FT-IR spectrometers, which proved to be essential in the determination and identification of the relatively short-lived metastable forms observed in this work. Raman spectroscopy is also a non-destructive technique that permits collection of spectra from samples that have been sealed in glass vessels such as capillary tubes, thus preventing air sensitive compounds from decomposing.

Advances in optical Raman microscopy now permit its use as a complementary tool, along with other spectroscopic and microscopic techniques, for the identification and determination of materials in their different phases from precipitation reactions. Stable and

metastable forms may be differentiated by simply comparing the characteristic spectra from each phase, and information such as the kinetic and structural properties of each polycrystalline form may also be deduced from the spectra.

In the past, spectroscopic studies on vaterite have been inconclusive and confusion exists as to the assignment of the vibrational bands. For example, in the  $\nu_1$  region of vaterite, it has been suggested that the observed doublet is either due to correlation field splitting effects (Anderson, 1996) or multiple site effects (Behrens *et al.*, 1995), but neither group was able to provide spectroscopic evidence to support their assignments. Recent advances in Raman spectroscopic techniques have made it possible to reinvestigate this system with much higher signal-to-noise to clarify the assignments of the vibrational spectra of vaterite.

#### **1.4 The Possible Incommensurate Phase of Calcium Carbonate**

Raman and infrared spectroscopic studies of natural and synthetic vaterite indicate an extremely complicated crystal structure where it appears the carbonate ions occupy a number of crystallographically distinct sites. The structure reported by Meyer (1969), an extension of Kamhi's research (1963), appears to be consistent with the work presented in this paper, but with our suggestion that the disordered stacking sequence is not random over the 12 carbonate sites, but rather follows that of an incommensurate phase similar to that of  $\gamma$ - $\text{Na}_2\text{CO}_3$ .

An incommensurate phase is one in which there is a superposition of two independent periodicities with the ratio of the periods usually an irrational number, with the result that there is no simple relationship between the incommensurate phase and some normal phase of

the compound (Levanyuk, 1986). The ratio of the periods cannot be expressed as a simple ratio of two integers because the periods are not fixed, but rather are continuously dependent on temperature and other external conditions (Section 4.6).

## Chapter 2

### Experimental

Solutions of  $\text{CaCl}_2$  (Baker-analysed reagent, 95.5 % assay),  $\text{K}_2\text{CO}_3$  (BDH Chemicals analytical reagent, 99.9 % assay),  $\text{Na}_2\text{CO}_3$  (Mallinckrodt analytical reagent) and  $(\text{NH}_4)_2\text{CO}_3$  (Aldrich Chemical Company) were prepared with nanopure water of high quality. These solutions were purified by adding charcoal activated powder (American Chemicals, Ltd.) and were filtered through a fine # 5 Whatman filter paper. Ammonium carbonate was the usual choice as the source of  $\text{CO}_3^{2-}$  ions except for in the  $^{18}\text{O}$  study of vaterite where  $\text{Na}_2\text{CO}_3$  was used.

All of the resulting precipitates were collected using a suction filtration apparatus equipped with a # 2 qualitative medium speed filter paper. The crystals were washed with high quality, nanopure water, anhydrous ethanol (Commercial Alcohols, Inc.) and acetone (Caledon, 99.5 % assay). All of the reagents used in the washing procedure were cooled in an ice-water bath before addition to the precipitates. For vaterite and  $\text{CaCO}_3 \cdot 6\text{H}_2\text{O}$ , rapid filtration was essential because the stability depended on minimal water contact. It was also important to maintain the  $\text{CaCl}_2$  and  $(\text{NH}_4)_2\text{CO}_3$  solutions at the required temperatures before and during the precipitation. Furthermore, the crystals were constantly spread out evenly over the filter paper to allow the maximum area for surface washing.

## **2.1 The Preparation of $\text{CaCO}_3 \cdot 6\text{H}_2\text{O}$**

Calcium carbonate hexahydrate crystals were prepared by adding 2 mL of a 1.0 M solution of  $\text{CaCl}_2$  to 2 mL of a 1.0 M solution of  $(\text{NH}_4)_2\text{CO}_3$ . Using a 1 mL syringe and under vigorous stirring conditions, the addition rate of the  $\text{CaCl}_2$  solution was 1 drop every 2-3 seconds at temperatures below 3 °C. The resulting suspension was milk-like. The suspension was then immediately filtered. The washing consisted of three quick 5 mL washes with water and three 10 mL washes with each of ethanol and acetone. After the washes were completed, the  $\text{CaCO}_3 \cdot 6\text{H}_2\text{O}$  crystals remained under suction for an additional 5 minutes to ensure the removal of all of the water, ethanol and acetone.

## **2.2 The Preparation of $\text{CaCO}_3 \cdot 1\text{H}_2\text{O}$**

Impure calcium carbonate monohydrate crystals were prepared by adding 1 mL of a 1.5 M solution of  $\text{CaCl}_2$  to 2 mL of a 2.0 M solution of  $(\text{NH}_4)_2\text{CO}_3$ . Using a 1 mL syringe and under vigorous stirring conditions, the addition rate of the  $\text{CaCl}_2$  solution was 1 drop every 2-3 seconds at a temperature between 3-10 °C. The resulting thixotropic suspension was immediately filtered. The washes were the same as for  $\text{CaCO}_3 \cdot 6\text{H}_2\text{O}$ , but with the only exception that the suction was broken upon the addition of wash water. The  $\text{CaCO}_3 \cdot 1\text{H}_2\text{O}$  crystals were also kept under suction for an additional 5 minutes to dry.

The above procedure resulted in mainly calcium carbonate monohydrate, but with varying amounts of calcite and vaterite impurities. However, pure  $\text{CaCO}_3 \cdot 1\text{H}_2\text{O}$  crystals were produced by dehydration of  $\text{CaCO}_3 \cdot 6\text{H}_2\text{O}$  at a temperature of 120 °C for 1 hour.

### **2.3 The Preparation of Calcite**

Calcite crystals were prepared by adding 1 mL of a 1.5 M solution of  $\text{CaCl}_2$  to 2 mL of a 2.0 M solution of  $(\text{NH}_4)_2\text{CO}_3$ . Using a 1 mL syringe and under relatively slow stirring conditions, the addition rate of the  $\text{CaCl}_2$  solution was 1 drop every 5-6 seconds at a temperature between 15-25 °C. The resulting milk-like suspension was allowed to stand for 24 hours. The remainder of the procedure was the same as for the first preparation of  $\text{CaCO}_3 \cdot \text{H}_2\text{O}$ .

### **2.4 The Preparation of Vaterite**

Vaterite crystals were prepared by adding 1 mL of a 1.5 M solution of  $\text{CaCl}_2$  to 2 mL of a 2.0 M solution of  $(\text{NH}_4)_2\text{CO}_3$ . Using a 1 mL syringe and under vigorous stirring conditions, the addition rate of the  $\text{CaCl}_2$  solution was 1 drop every 2-3 seconds at a temperature between 25-40 °C. The resulting milk-like suspension was immediately filtered. The remainder of the procedure was the same as for  $\text{CaCO}_3 \cdot 6\text{H}_2\text{O}$ .

In the  $^{18}\text{O}$  study of vaterite, a sample of  $^{18}\text{O}$ -enriched vaterite was prepared. The procedure was the same as above except for the fact that 12 mol % of 70 %  $^{18}\text{O}$ -enriched  $\text{Na}_2\text{CO}_3$  was added to the initial natural  $\text{Na}_2\text{CO}_3$  solution. The vaterite crystals prepared in this manner were approximately 8 %  $^{18}\text{O}$ -enriched.

### **2.5 The Preparation of Aragonite**

Aragonite crystals were prepared by adding 2 mL of a 1.0 M solution of  $\text{CaCl}_2$  to 2 mL of a 1.0 M solution of  $(\text{NH}_4)_2\text{CO}_3$ . Using a 1 mL syringe and under vigorous stirring conditions, the addition rate of the  $\text{CaCl}_2$  solution was 1 drop every 2-3 seconds at a

temperature between 60-90 °C. The resulting milk-like suspension was immediately filtered. The remainder of the procedure was the same as for vaterite.

## **2.6 Raman Spectroscopic Measurements**

The Raman equipment was a Renishaw Raman imaging microscope (System 1000) consisting of a single spectrograph (0.25 m focal length) containing a holographic grating (1800 grooves/mm) and a notch filter, an Olympus BH-2 microscope equipped with 10x, 20x and 50x objective lenses, and a Peltier-cooled CCD detector (600 x 400 pixels). The majority of samples were excited with 514.5 nm radiation from a 35 mW air-cooled argon ion laser (Spectra-Physics, Model #: 163-A42) and the laser beam was focussed on the sample by a 50x objective lens to give a spot size of *ca.* 1  $\mu\text{m}$ . The spectral resolution was about 2  $\text{cm}^{-1}$ . In order to obtain the low wavenumber spectral range, samples were also studied with the 632.8 nm excitation line from a 12 mW air-cooled He-Ne laser (Jodon Laser, Model #: HN-20X) because of the difference in sensitivity between the two notch filters. All the samples were studied on a microscope slide immediately after preparation. The exposure times ranged from 30 to 200 seconds and the accumulations were between 1 and 30 depending on the signal-to-noise ratios (S/N) and on the scattering quality of the sample.

Curve resolving was performed with Galactica Grams/386 and Jandel Scientific Sigma Plot 2.0 software for the purpose of determining the number of components contained in each region, as well as their respective frequencies and full widths at half height (FWHM). A Gaussian-Lorentzian line shape was assumed in all the curve analyses.

The effect of temperature on the Raman spectrum of vaterite was investigated using

a Coderg PHO Raman spectrometer with the standard  $90^\circ$  scattering geometry. The 488.0 nm line of the argon ion laser was used as the source of excitation with a power level of about 300 mW. The slits were  $0.25 \text{ cm}^{-1}$ , the scanning rate was  $10 \text{ cm}^{-1}/\text{minute}$  and eight data points were collected per wavenumber. The scattering light was detected by a photo-multiplier tube (PMT) cooled to  $-20^\circ\text{C}$ . The sample was placed in a capillary tube and cooled to 77 K on the cold finger of a liquid nitrogen vacuum glass cryostat.

Raman spectra were calibrated with the Hg emission line from a mercury lamp ( $1122.7 \text{ cm}^{-1}$ ) and solid silicon ( $520.2 \text{ cm}^{-1}$ ).

## **2.7 Infrared Spectroscopic Measurements**

For infrared analysis, each sample was ground with KBr to a sufficiently fine powder using a mortar and pestle in a MBraun Lab Master 130 nitrogen glove box (Model #: MB-130-BG) to give spectra with relatively symmetrical absorption bands, minimally distorted by the Christiansen filter effect (Brooker, 1992). All measurements were made as pellets with a KBr diluent (*ca.* 290 mg of spectroscopically pure, infrared grade KBr (Fisher Scientific) + 4 mg sample) that was first dried at  $135^\circ\text{C}$  for 1 hour. The mixtures were then pressed at reduced pressure using a KBr Die MK3 (Research and Industrial Instruments Company) and a hydraulic press (Fred S. Carver Inc., Model #: 19205-25) to a maximum pressure of *ca.* 15,000 pounds per square inch.

Absorbance spectra of the anhydrous carbonate samples were collected over the spectral range  $4000\text{-}500 \text{ cm}^{-1}$ , at  $2 \text{ cm}^{-1}$  spectral resolution, using a Mattson Polaris FT-IR spectrometer. The number of accumulations for both sample and background scans was set

at 32.

As was the case with the Raman spectra, curve resolving was performed on the infrared spectra with Galactica Grams/386 and Jandel Scientific Sigma Plot 2.0 software for the purpose of determining the number of components contained in each region, as well as their respective frequencies and full widths at half height. A Gaussian-Lorentzian line shape was assumed in all curve analyses.

Infrared spectra were calibrated with an infrared-active vibration of CO<sub>2</sub> which is observed in the infrared at *ca.* 667.8 cm<sup>-1</sup>.

## **2.8 Morphological Investigations**

For the scanning electron microscopic imaging, each sample was suspended in absolute ethanol and then mounted on an Al metal stub. After drying at room temperature, the samples were coated with gold using an Edwards S150A sputter coater equipped with an argon gas supply for purging purposes.

The majority of the morphological studies of the calcium carbonate phases were carried out with a Hitachi S570 scanning electron microscope operating at an accelerating voltage of 20 keV. Micrographs were produced by secondary electrons. The microscopic working distances ranged between 15 and 23 mm, with magnifications up to 11,000x, depending on the height and quality of the crystals, as well on the efficiency of the gold-coating.

Scanning electron micrographs of the solids in their different phases were recorded on a Polaroid type 665 positive/negative film using a Polaroid camera which was attached to

the scanning electron microscope.

The remainder of the morphological studies were carried out with a Sony CCD-IRIS colour video camera (Model #: 111048), a Sony camera adaptor CMA-D2 and a Play Inc. Snappy 3.0 image capturing device which were coupled to the Renishaw Raman imaging microscope assembly. The ranges for the microscope working distances and magnifications were 1 to 7 mm and 50 to 10x respectively.

## **2.9 Thermoanalytical Measurements**

Phase transformations were followed by differential scanning calorimetry (DSC). The DSC analyses were carried out under non-isothermal conditions in a nitrogen flow with a Seiko Instruments SSC5300 DSC thermal analysis system. The measurements were performed in the temperature interval from 295 to 823 K, with heating rates of 10 and 20 K/min, and a sampling rate of 1 point/second. The rate of nitrogen flow was 100 cm<sup>3</sup>/min and the masses of the samples ranged from 1.69 to 17.29 mg. The temperature was limited to 823 K by the characteristics of the aluminum sample holder pans.

The vaterite samples were also analysed using thermogravimetry with evolved gas analysis (TG-EGA). The instrument used was a TG Plus consisting of a Dupont 900 thermogravimeter (TG) connected to a BOMEM MB100 interferometer (FT-IR) via a 16-pass gas cell. The vaterite samples were heated from 303 to 1173 K with heating rates of 10 and 20 K/minute. Gases released (i.e. CO, CO<sub>2</sub> and H<sub>2</sub>O) from the vaterite samples being heated in the TG were swept into the gas cell by the helium purge gas flowing at 882 mL/minute. During the scans, infrared spectra of these gases were taken every 0.3 minutes

with the weight of the vaterite sample and the temperature being constantly monitored and recorded. Results are expressed as a percentage of the initial sample weight.

### **2.10 Structural Investigations**

Vaterite samples for X-ray diffraction (XRD) studies were mixed with Si-metal standard and lightly crushed in a mortar and pestle with a sample to silicon mixture ratio of 80:20. The mixtures were then immersed in acetone, spread on a glass slide and then allowed to dry for *ca.* 24 hours.

Powder XRD patterns of the solids were collected using a Rigaku RU-200 automated diffractometer using Cu-K $\alpha$  radiation generated with an accelerating voltage of 40 keV and a filament current of 100 mA.

## **Chapter 3**

### **Theory**

The formation and transformation of minerals is a complex and important aspect of geochemistry. The understanding of these changes requires an in-depth appreciation of the structure of the reactants and products. Minerals represent a collection of atoms whose aggregation depends on factors such as the composition, pressure and temperature of the natural environment in which they were formed (Putnis, 1992).

#### **3.1 Phase Transformations**

Many materials can exist with different crystal structures under different conditions. It is often possible to convert between these phases. Phase transitions can be classified or described on a number of different criteria and these have been reviewed by a number of authors (Visintin, 1996; Brooker and Wang, 1993; Bruce and Cowley, 1981; Lévy *et al.*, 1982).

##### **3.1.1 Thermodynamic/Macroscopic Concepts: Transformation Orders**

Thermodynamically, phase transformations are characterized by their order. The order of the transformation is defined by the order of the derivative of the Gibbs free energy ( $G$ ) that displays a discontinuity. There are three major kinds of transformation orders: first-order, second-order and lambda-order.

### 3.1.1.1 First-Order Transformations

At a particular temperature and pressure at which a phase transformation occurs, the free energies of the two polymorphs are equal. Consequently, there will be no discontinuity in the free energy on passing from one form to the other. However, in first-order transformations the first derivatives of  $G$ ,  $(\partial G/\partial T)_P$  and  $(\partial G/\partial P)_T$ , exhibit discontinuities. Since,

$$(\partial G/\partial T)_P = -S \quad (3.1)$$

and

$$(\partial G/\partial P)_T = V \quad (3.2)$$

first-order transformations are characterized by discontinuities in the entropy ( $S$ ) and the molar volume ( $V$ ) at the transformation temperature. Similarly, there is a discontinuity in the enthalpy ( $H$ ), since, at the transformation temperature,  $C_p$  approaches infinity due to the heat used to convert one phase to the other (i.e. latent heat) (Blackburn and Dennen, 1994; Laidler and Meiser, 1995; Putnis, 1992).

### 3.1.1.2 Second-Order Transformations

In second-order transformations,  $G$  and its first derivatives are continuous, but its second derivatives,

$$(\partial^2 G/\partial T^2)_P = -(\partial S/\partial T)_P = -C_p/T \quad (3.3)$$

$$(\partial^2 G/\partial P^2)_T = -V[-(1/V)(\partial V/\partial P)_T] = -V\beta = (\partial V/\partial P)_T \quad (3.4)$$

$$(\partial^2 G / \partial T \partial P) = V[(1/V)(\partial V / \partial T)_P] = V\alpha = (\partial V / \partial T)_P \quad (3.5)$$

all exhibit discontinuities across the transformation. Since the enthalpy change is continuous there is no latent heat associated with second-order phase transformations, a point of difference from first-order phase transformations (Blackburn and Dennen, 1994; Laidler and Meiser, 1995; Putnis, 1992; Yuhnovskii, 1987).

Second-order phase transformations are usually difficult to establish and are often described as  $\lambda$ -transitions (Brooker and Wang, 1993).

### 3.1.1.3 Lambda-Order Transformations

Lambda-order transformations are characterized by the shape of the  $C_p$ -versus- $T$  curve which resembles the Greek letter  $\lambda$ . In these types of transformations,  $C_p$  approaches infinity at the transformation temperature, which is commonly referred to as the lambda-point temperature ( $T_\lambda$ ). The area under the  $C_p$ -versus- $T$  curve (i.e. the enthalpy) is a finite value and hence, is a continuous function. Even though there is no true latent heat, the change in the enthalpy is defined as the  $\Delta H$  of the transformation. The molar volume is also continuous at  $T_\lambda$ , but its slope  $(\partial V / \partial T)_P$  is infinite at this temperature (Blackburn and Dennen, 1994; Laidler and Meiser, 1995; Putnis, 1992).

### 3.1.2 Structural/Microscopic Considerations

Polymorphism can also be discussed in terms of differences in crystal structures. Crystal structures for many different phases of the same chemical compound have been established by X-ray diffraction patterns (Wells, 1975). The rate of change from one polymorph to another may be very slow or extremely rapid, depending on the degree of

reconstruction of the structure.

### **3.1.2.1 Displacive Phase Transformations**

Displacive phase transformations involve slight displacements of the structural units in such a way as to change the symmetry, without disrupting any of the chemical bonds. Thermodynamically, these transitions may be first-order or second-order. Under a unique set of physical conditions, the transformation tends to be rapid due to the relatively low activation energy barrier. This relatively low activation energy barrier reflects only the energy required to rotate the bond angles and is indicative of the relatively small energy difference between the two polymorphs. As a result, displacive transformations are generally faster than reconstructive transformations (Section 3.1.2.2) (Blackburn and Dennen, 1994; Bruce and Cowley, 1981; Putnis, 1992). The  $\alpha$ - $\beta$  phase transformation in cristobalite is an example of a displacive phase transformation where the Si-O-Si bond angle merely undergoes a slight rotational displacement (Schmahl *et al.*, 1992).

### **3.1.2.2 Reconstructive Phase Transformations**

Reconstructive phase transformations involve two major processes. The initial process is one of bond breaking which is followed by bond formation and reconstruction. Thermodynamically, these transitions are always first-order and result in large discontinuities in the enthalpy, entropy and molar volume. In the majority of cases, they require the presence of a catalyst because the two polymorphic forms are separated by a relatively large activation energy barrier. This activation energy barrier is relatively high because it reflects the energy required to break the specific bonds and, as a consequence, these transformations are

kinetically slower than displacive phase transformations (Adams, 1974; Blackburn and Dennen, 1994; Putnis, 1992). The aragonite--calcite phase transformation in the  $\text{CaCO}_3$  system is an example of a reconstructive phase transformations since bonds between the  $\text{Ca}^{2-}$  and  $\text{CO}_3^{2-}$  ions are broken and then reformed (Blackburn and Dennen, 1994).

### **3.1.2.3 Order-Disorder Phase Transformations**

Order-disorder phase transformations involve the transition from an ordered state to a disordered state (Sections 3.2.1.1 and 3.2.1.2 respectively). Order-disorder phase transformations may either be sluggish or rapid depending on whether the disorder is substitutional, as in the Si and Al substitution in sanidine (Blackburn and Dennen, 1994), or orientational, as is the case of  $\text{NaNO}_3$  (Adams, 1974). Thermodynamically, these types of transformations may be first-order or second-order (Bruce and Cowley, 1981; Laidler and Meiser, 1995) .

### **3.1.3 Kinetic Theory of Phase Transformations**

A complex mineral may fail to transform to the thermodynamically most stable state and it may undergo a structurally easier transformation to some intermediate metastable phase. Although not thermodynamically stable under the given set of conditions, the metastable phase may be kinetically more accessible. The persistence of metastable phases and their preservation over geological time is a consequence of the sluggish kinetics of such phases under ambient conditions. Metastable phases are often formed from quenching processes (Schmahl *et al.*, 1992).

### 3.1.3.1 Thermodynamics of Metastable Phases

The intermediate states through which a system passes during its transformation are of particular importance because the kinetics are not solely governed by the changes in the Gibbs free energy (i.e.  $\Delta G$ ).

When a system passes from an initial, metastable state to a final, thermodynamically more stable state which has a lower free energy, it passes through an activated transition complex and/or an intermediate state (Figure 3.1). The driving force for the transformation is the reduction in the free energy, but in order to initially achieve this state the system must first overcome  $\Delta G_a$ , the free energy of activation.

The free energy of activation depends on the pathway of the reaction, with the lowest  $\Delta G_a$  being favoured. In order for a transformation to occur at an appreciable rate, it is necessary that a sufficient number of atoms have enough energy to reach the transition maximum. At any temperature above 0 K, the vibrations of the atoms about their structural sites provide a large contribution to the energy of the system. Thermal motions result in relatively large differences in the instantaneous positions of individual atoms. The end result is that some of these atoms will have sufficient energy to overcome the activation energy barrier and jump to another site.

The concept of an activation energy barrier is very useful in a qualitative explanation of a number of aspects encountered in mineral reactions. It accounts for the persistence of metastable states when insufficient energy is available to initiate the transformation. It shows the effects of addition of catalysts on the value of  $\Delta G_a$  for a particular reaction. That is, a

catalyst provides an alternate reaction mechanism which effectively lowers the activation energy barrier. Finally, it helps to explain the slow rate of many transformations due to the small number of atoms, at any one time, with sufficient free energy to overcome the  $\Delta G_a$  barrier (Laidler and Meiser, 1995; Putnis, 1992).

### 3.1.3.2 Precipitation of Metastable Phases

Metastable solids can form from aqueous solutions. The  $\text{CaCO}_3$  precipitation system represents an excellent example (Kralj *et al.*, 1997). The product of precipitation of calcium carbonate is dependent upon two processes, nucleation and crystal growth (Tarits *et al.*, 1990). The nucleation process is controlled by the supersaturation state of the solution ( $S$ ) which determines the resulting precipitation species. The supersaturation state is expressed as the saturation ratio (Kralj *et al.*, 1997),

$$S = Q/K_{sp} = ([\text{Ca}^{2+}] \cdot [\text{CO}_3^{2-}] \cdot \gamma^2 / K_{sp})^{1/2} \quad (3.6)$$

where  $Q$  is the supersaturation activity product,  $K_{sp}$  is the solubility product of calcite and  $\gamma$  is the mean activity coefficient of the divalent ions. In these particular systems, the precipitation from aqueous solutions can lead to the production and isolation of a number of different solid phases. In the majority of cases, kinetic factors govern, and even dominate, the precipitation processes. As a result, thermodynamically metastable phases are produced which have thermodynamic properties that are associated with slight differences in solubility under a given set of conditions.

Metastable phases can be differentiated by their slight differences in solubility and their occurrence can be explained with Ostwald's Law of Stages (Brooks *et al.*, 1951; Kralj *et al.*,

1997). According to this law, a metastable precipitate will subsequently transform to the more stable form given sufficient time. There are two possible mechanisms by which the transformation from the less stable phase to the more stable phase will take place: solid-state transformation or solution-mediated transformation (Kralj *et al.*, 1997). In a solid-state transformation, the crystal structure undergoes internal rearrangement. However, in a solution-mediated transformation, there is an initial dissolution of the unstable solid phase which eventually leads to the nucleation and crystal growth of a more stable modification for the given conditions.

In the calcium carbonate precipitation system, when the solubility quotient  $a_{\text{Ca}^{2+}} \cdot a_{\text{CO}_3^{2-}}$  has reached  $K_{\text{calcite}}$ , then calcite will begin to precipitate from aqueous solutions, but only if there are nuclei of calcite present or some isomorphous species, such as  $\text{MgCO}_3$ , which exhibits the same crystal structure. However, in the absence of a proper nucleating site, the solubility quotient will continue to increase until a value characteristic of one or more of the other unstable phases is reached. Hence, it would be possible to simultaneously attain any, or all, of the phases which exhibit a solubility quotient equal to, or lower, than the solubility quotient present at the time precipitation occurs (Johnston *et al.*, 1916). Once dry the metastable solids may exist for a long period of time.

### **3.1.4 Experimental Methods Used to Study Phase Transformations**

The differences in bonding, chemistry and structure between the initial and final forms of a structural phase transformation allow for easy detection with a variety of techniques. These techniques may include thermal investigations such as DSC and TG-EGA (Maciejewski

*et al.*, 1994; Perić *et al.*, 1996), spectroscopic studies such as Raman and FT-IR (Farmer, 1974; Laserna, 1996), and diffraction studies such as SEM and powder XRD (Ladd and Palmer, 1993; Stout and Jensen, 1968). A number of electrical and visual methods which rely on changes to mechanical properties (i.e. conductivity, dielectric constant, dilatometry, etc.) have also been used (Hume, 1925; Johnston *et al.*, 1916; Mackenzie, 1923).

#### **3.1.4.1 Thermal Investigations**

The heat capacity of a sample can be measured directly with a calorimeter along with thermodynamic properties such as the enthalpy and entropy changes. In our studies, the choice was DSC.

#### **3.1.4.2 Spectroscopic Studies**

The interatomic forces between bonded atoms determine the exact frequency of the individual vibrations. In principle, every phase of every compound will have a different set of vibrational frequencies.

#### **3.1.4.3 Diffraction Studies**

As is the case with spectroscopic studies, crystals of different phases of a system will have unique diffraction patterns because of differences in atomic positions.

#### **3.1.4.4 Mechanical Methods**

Phase transformations are often accompanied by slight differences in appearances and densities. The variations in appearance can be distinguished by optical microscopy. The density changes can be measured directly by dilatometry and often indirectly by conductivity.

## **3.2 Crystal Structures**

The atoms of a crystal are held in fixed positions by chemical bonds. The grouping of atoms in a regular pattern along with their bonding arrangements in 3-dimensional space, constitutes the crystalline structure, and the geometrical framework which relates the elements within the structure is termed the lattice (Adams, 1974). These positions are generally sites of regular pattern and spacing. However, thermal agitation, as well as rapid nucleation and crystal growth, result in the random occupancies of some sites by certain atoms. This leads to patterns of irregularity. There are three major types of crystal structures: ordered, disordered and incommensurate.

### **3.2.1 Ordered Crystals**

Ordered phases exhibit perfect 3-dimensional translational periodicity and the regular pattern of the atoms provide the lowest free energy for the structure.

### **3.2.2 Disordered Crystals**

Disordered phases partially, or completely, lack translational symmetry because of the irregular arrangement of the ions and vacancies within the structure. A structure exhibiting completely random arrangements is considered to be amorphous or glass-like (Brooker and Papatheodorou, 1983), and all intermediate stages between complete order and complete disorder are possible. There are two different types of disorder: dynamic and static (Adams, 1974). Dynamic disorder is dependent upon the motions of the ions. That is, the atoms move among different lattice sites. Static disorder is solely dependent upon the equilibrium positions of atoms. That is, the atoms can randomly occupy two or more similar lattice sites.

### **3.2.3 Incommensurate Crystals**

In recent years, a new type of disorder has been recognized and crystals with this type of disorder are classified as incommensurate. The literal meaning is "not in proportion to". This name has been chosen because there are two independent periodicities of translational symmetry, the ratio of which is not a rational number. A more detailed description of the incommensurate phase will be presented since the concept is relatively new. Furthermore, it will be shown that this type of phase may explain the unusual features found in the Raman, infrared and X-ray diffraction spectra for vaterite.

In most cases, the atomic position is chosen as the local property which is modulated with a particular periodicity of a crystal. In incommensurate phases, at least one atomic position is not exactly repeated from one unit cell to another and, consequently, the translational symmetry of the crystal is lost in at least one direction, although approximate long-range order persists. However, the translational lattice periodicity is usually restored at lower temperatures at what is known as a "lock-in" phase transition where the lattice modulation changes from incommensurate to commensurate (Tolédano and Tolédano, 1987).

For incommensurate phases, two important phenomena are observed: namely solid-state chaos and the devil's staircase (De Wolff and Tuinstra, 1986). Solid-state chaos simply refers to the loss of the translational symmetry in at least one direction. The devil's staircase refers to the presence of a propagating wave vector of the superstructure which is considered to be rational, consisting of an infinite number of rational numbers (De Wolff and Tuinstra, 1986).

Unlike an "ordinary" crystal, the incommensurate system has no exact translational symmetry, but does exhibit some approximate long-range ordering. The size of the unit cell along the modulation axis can be equal to the crystal size and, consequently, the unit cell will be comprised of a large number of atoms. In various light scattering techniques from ordered crystals, such as Raman and infrared, the number of spectral lines is no more than triple the total number of atoms, ions, or molecules in the unit cell, along with the number of formula units also present in the unit cell. Hence, it could be expected that the total number of normal modes exhibited by an incommensurate phase would be infinite since we are dealing with a continuous range of normal modes (i.e. glass-like). However, in actual fact, even in incommensurate phases a relatively small number of well-defined lines is usually observed. This can be accounted for by the Landau theory of phase transitions which states that the symmetry of the high-symmetry phase is the most important, not that of the low-symmetry phase. Consequently, XRD patterns for incommensurate crystals will often give satellite reflections, or super-lattice reflections (De Wolff and Tuinstra, 1986; Iqbal, 1984; Levanyuk, 1986; Tolédano and Tolédano, 1987).

### **3.2.3.1 Mathematical Definition**

From Landau's theory, incommensurate phase transitions can be thought of as continuous structural transitions to a high-symmetry crystalline phase. This arises from the fact that the wave vector  $k$  fulfills the requirement that at least one  $q_i$  is irrational. This is exemplified by the following wave vector equation (Tolédano and Tolédano, 1987),

$$k = \sum q_i \cdot a_i^* \quad (3.7)$$

where  $q_i$  is a particular temperature-based coordinate and  $a_i^*$  is a reciprocal lattice translation point coherent in the high-symmetry phase.

As seen in Figure 3.2, there is a sequence of three distinct phases which are separated by two phase transitions, the lower one,  $T_{\text{Lock-in}}$ , being the lock-in phase transition and the upper one,  $T_{\text{INC}}$ , being the incommensurate phase transition. In the region just below  $T_{\text{INC}}$ , the situation is essentially that of an ordinary structural transition because the structural and physical properties of the low-symmetry phase can be associated to a single, irreducible representation of the high-symmetry phase whose wave vector has temperature independent components (Tolédano and Tolédano, 1987). However, since the low-symmetry phase exhibits non-crystallinity, it cannot be identified by one of the 3-dimensional space groups because of the irrational  $q_i$  component(s). Hence, even though there is distortion present in the low-symmetry phase, it is still a perfectly ordered phase in that it has a Fourier-transform which displays both the three elementary periods,  $a_i^*$ , as well as a limited number of additional periods which are linked to  $q_i$ . The Fourier components relative to the elementary periods are termed as the principal components and the Fourier components relative to the limited number of additional components are classified as the satellite components (Tolédano and Tolédano, 1987). The satellite components are only a small modulation of the density of the particles in the actual system and they reflect how the principal structure is modified. However, the vast majority of the density has a 3-dimensional periodicity which is essentially defined by the  $a_i^*$  (Tolédano and Tolédano, 1987).

In the simplest situation, the diffraction wave vector  $k$  can be represented by the

following equation (Aalst *et al.*, 1976),

$$\mathbf{k} = h\mathbf{a}^* + k\mathbf{b}^* + l\mathbf{c}^* + m\mathbf{q} \quad (3.8)$$

where  $h$ ,  $k$  and  $l$  are integers in a Miller index,  $m$  is an integer,  $a$ ,  $b$  and  $c$  are unit cell edge lengths and  $a^*$ ,  $b^*$  and  $c^*$  are reciprocal point translations corresponding to  $a$ ,  $b$  and  $c$  respectively. Hence, from the previous equation, the main XRD reflections will have  $m = 0$  and the satellites will have  $m \neq 0$ . The interpretation of this equation is that there is a deviation from some perfect periodic structure, such that it leads to the deviation exhibiting a periodicity. When this occurs in a particular system, there is no 3-dimensional space group symmetry and, hence, no exact translational symmetry (De Wolff and Tuinstra, 1986.)

Figure 3.2 shows three main distinguishing features of an incommensurate system which are portrayed in the low-symmetry phase region: namely the region between  $T_{\text{Lock-in}}$  and  $T_{\text{INC}}$  (Tolédano and Tolédano, 1987). Firstly, the temperature range between  $T_{\text{Lock-in}}$  and  $T_{\text{INC}}$  is considered to be the stability range of the incommensurate system (Tolédano and Tolédano, 1987). Secondly, in the region just below  $T_{\text{Lock-in}}$ , the commensurate phase becomes the stable phase and, like the incommensurate phase, it consists of a structural distortion of the high-symmetry phase. However, unlike the incommensurate phase, the wave vector of the commensurate phase has temperature-independent components. Below  $T_{\text{Lock-in}}$ , the commensurate phase can be identified by a 3-dimensional space group involving primitive translations which are derived from the high-symmetry phase. The lock-in temperature arises from the fact that the lowering of the temperature results in the locking of the all the fundamental periods in the system. Hence, the lowering of the symmetry involved in the

structural transition from the high-symmetry phase to the commensurate phase results in the production of a finite number of energetically equivalent, commensurate states which are related to each other by space symmetry operations. These energetically equivalent, commensurate states are believed to co-exist in a given incommensurate system in the form of domains (Tolédano and Tolédano, 1987). Thirdly, in the region near the lock-in temperature, the incommensurate phase can essentially be regarded as a periodic array of commensurate domains separated by small discommensurations or domain walls (Iqbal, 1984; Tolédano and Tolédano, 1987). The resulting periods of the commensurate domains are determined by the differences in the incommensurate components of the wave vector at the specific temperature and at the lock-in temperature. Consequently, the differences tend to be very minute as the temperature is lowered near  $T_{\text{Lock-in}}$  because the size of the individual commensurate domains tend to become larger as the structure of the incommensurate phase approaches that of the commensurate phase (Tolédano and Tolédano, 1987).

### **3.2.2 Lattice Dynamics**

The spectroscopy of ordered molecular crystals is defined by matter waves of vibrating atoms called phonons. Phonons are quanta of vibrational energy that can be looked upon as elementary particles. Consequently, the vibrational displacements of the atoms and ions in the lattice may be described as simple motions parallel to the x, y or z axis. These vibrational displacements give rise to two distinct types of modes: acoustic and optic. Acoustic modes, of which there are three (i.e. one longitudinal and two transverse), are travelling sound waves of low frequency ( $< 2 \text{ cm}^{-1}$ ). However, optic modes are standing

waves of higher frequency ( $\approx 10\text{-}4000\text{ cm}^{-1}$ ) (Laidler and Meiser, 1995).

### 3.2.2.1 Normal Modes of Vibration

In the  $k=0$  approximation, only vibrations of atoms in phase, vibrating in different unit cells, are active and the selection rules state that these atoms of a unit cell are sufficient for determining the total number of normal modes of vibration (Fateley *et al.*, 1972; Iqbal, 1984).

Because the molecules within a unit cell are loosely coupled together, they vibrate similar to that of a giant molecule. The number of normal modes of vibration ( Eq. 3.9) are governed by the symmetry of the unit cell:

$$\# \text{ of normal modes of vibration} = 3NZ - 3 \quad (3.9)$$

where  $N$  is the number of atoms,  $Z$  is the number of formula units present in the unit cell,  $NZ$  is the total number of atoms in the unit cell and  $-3$  is for the three acoustic modes which are denoted as  $T_x$ ,  $T_y$  and  $T_z$  in the character table for the crystal symmetry. Hence, there will be  $3NZ$  different combinations of motions with each of these combinations having its own unique frequency ( $\nu$ ) for a given wave vector. For any single wave, each atom will move with the same frequency and wave vector, with the interatomic forces determining the direction of the wave motion in any atom. However, the amplitude of the wave motion is determined by the temperature and the frequency of the wave (Fateley *et al.*, 1972; Laidler and Meiser, 1995; Turrell, 1972).

Molecular crystals have a unique feature in that there is a large difference between the two kinds of optic modes: external and internal modes. External modes involve the rotational and translational motions of whole molecules. For these modes, the centre of mass of the

molecules move, but the centre of mass of the unit cell remains constant with respect to neighbouring unit cells. Internal modes, or covalent modes, involve the modes of discrete molecules or molecular ions. They are largely dependent on site splitting and on correlation field splitting, with a relatively weak dependence on the wave vector. Unlike external modes, internal modes do not result in the movement of the centre of mass of the molecule.

In addition to correlation field coupling (i.e. dynamic) effects, there are also static field effects. Dynamic field effects are dependent upon the coupling of the intermolecular motions of ions, whereas static field effects, also known as site or local splitting, are dependent on the symmetry of the field at a site. The latter are represented by static potentials which require a potential of lower symmetry in order to remove a particular degeneracy.

If a crystal has a particular symmetry the lattice vibrations cannot have symmetry higher than that of the unit cell. That is, they must be of equal or lower symmetry. Since each vibrational mode is assigned a unique symmetry which corresponds to a single irreducible representation of the point group of the particular wave vector, then different modes will have different effects on the symmetry of the structure (Fateley *et al.*, 1972).

### **3.2.2.2 Correlation Field Coupling**

Correlation field coupling of the vibrational modes of identical molecules in the unit cell is known by a variety of names such as Davydov, factor group and intermolecular coupling. It occurs when vibrations of two or more ions of the same type present in a unit cell are coupled, either in phase or with opposite phases, resulting in both vibrations appearing in the vibrational spectra. However, this effect arises only when the selection rules for the

given unit cell symmetry permit it. The possibility for additional bands due to correlation field coupling increases with an increase in the number of atoms in the unit cell (Turrell, 1972).

#### **3.2.2.2.1 Origins**

There are two proposed theories as to the origin of correlation field coupling (Decius and Hexter, 1977). Firstly, Dows has proposed that the splitting is due to the repulsive forces between molecules which are by their nature of short-range (i.e.  $r^{-6}$ , where  $r$  is the equilibrium bond length). Secondly, Decius and Hexter have proposed that the splitting is due to the dipole moment of a molecule which fluctuates during the course of a particular vibration. Hence, it is of long-range order (i.e.  $r^{-3}$ ). The latter is a result of dipole-transition dipole-transition coupling and, consequently, the degree of separation of the molecules is directly proportional to  $(\partial \vec{\mu} / \partial q_i)^2$  which is also a measure of the band intensity in infrared spectra (Brooker and Bates, 1971). The preferred theory is that proposed by Decius and Hexter.

#### **3.2.2.2.2 Unit Cell Group Analysis Method**

The unit cell group analysis method involves the use of tables which show the effect on an atom or molecule of either raising or lowering the symmetry within the structure. The correlations are represented by solid lines on the tables which connect the modes of the point group to the modes of the crystallographic site group and, finally, to the modes of the factor, or unit cell group. This is the case for discrete molecules, or molecular ions. However, for simple correlations, such as individual ions, it is only necessary to correlate the crystallographic site symmetry of the ion to the symmetry of the unit cell (Fateley *et al.*, 1972; Turrell, 1972).

The unit cell group analysis method requires that the crystal structure be established and that there be a relatively small number of formula units contained in the unit cell. Consequently, the unit cell group analysis method is not applicable to vaterite because of the lack of crystals of sufficient size for single crystal analysis. In favourable cases, Raman and infrared spectroscopy may be used to predict the crystal structure of a powdered sample if their spectra are similar to that of an isomorphous sample whose crystal structure has already been established. Raman and infrared spectroscopy may also be used to confirm the number of formula units present in a unit cell. The unit cell group analysis method for aragonite and calcite will be presented as an example.

#### 3.2.2.2.3 Application to Aragonite and Calcite

Aragonite exhibits orthorhombic symmetry,  $D_{2h}^{16}$ , with four formula units (i.e.  $Z = 4$ ) contained in the unit cell. Since each  $\text{CaCO}_3$  unit contains five atoms (ie.  $N = 5$ ), the total number of normal modes of vibrations (i.e.  $3NZ$ ) for the orthorhombic unit cell is 60 (Gillet *et al.*, 1993).

The acoustic modes from the  $D_{2h}^{16}$  character table (Table 3.1) are  $B_{1u}$ ,  $B_{2u}$  and  $B_{3u}$ , and the selection rules forbid the activity of the  $A_u$  mode in the Raman and infrared spectra (Fateley *et al.*, 1972).

Since the calcium ion can be looked upon as having a completely spherical structure, it is only necessary to examine the external vibrational modes. From XRD studies, the crystallographic site symmetry of the calcium ions is  $C_s$ , Wyckoff notation 4c.

The table used to correlate the site symmetry of the calcium ions to the symmetry of

the unit cell is given in Table 3.2 (Fateley *et al.*, 1972). This gives the external vibrational modes of the calcium ions (Figure 3.3).

Since the carbonate ion is a discrete molecular ion, it is necessary to examine both the external and internal vibrational modes. The point group symmetry of the free carbonate ion is denoted as  $D_{3h}$ . From XRD studies, the crystallographic site symmetry of the carbonate ions is  $C_s$ , Wyckoff notation 4c.

The tables used to correlate the point group symmetry of the free carbonate ions to their site symmetry and, subsequently, to the symmetry of the unit cell are given in Tables 3.3 and 3.2 respectively (Fateley *et al.*, 1972). This gives the external (rotatory and translatory) and internal vibrational modes of the carbonate ions (Figures 3.4 and 3.5 respectively).

Calcite exhibits hexagonal symmetry and belongs to space group  $D_{3d}^6$ , with two formula units contained in the rhombohedral unit cell. Since each molecule of  $CaCO_3$  contains five atoms, the total number of normal modes of vibrations for the rhombohedral unit cell is 30 (Gillet *et al.*, 1993).

The acoustic modes from the  $D_{3d}^6$  character table (Table 3.4) are  $A_{2u}$  and  $E_u$ , and the selection rules forbid the activity of the  $A_{1u}$  mode in the Raman and infrared spectrum (Fateley *et al.*, 1972).

From XRD studies, the crystallographic site symmetry of the calcium ions is  $S_6$ , Wyckoff notation 2b.

The table used to correlate the site symmetry of the calcium ions to the symmetry of the unit cell is given in Table 3.5 (Fateley *et al.*, 1972). This gives the external vibrational

modes of the calcium ions (Figure 3.6).

From XRD studies, the crystallographic site symmetry of the carbonate ions is  $D_3$ , Wyckoff notation 2a.

The tables used to correlate the point group symmetry of the free carbonate ions to their site symmetry and, subsequently, to the symmetry of the unit cell are given in Tables 3.6 and 3.7 respectively (Fateley *et al.*, 1972). This gives the external (rotatory and translatory) and internal vibrational modes of the carbonate ions (Figures 3.7 and 3.8 respectively).

Table 3.1 Character table for the  $D_{2h}^{16}$  space group of aragonite.

$D_{2h}^{16}$	E	$C_2(z)$	$C_2(y)$	$C_2(x)$	I	$\sigma_{xy}$	$\sigma_{xz}$	$\sigma_{yz}$		
$A_g$	1	1	1	1	1	1	1	1		$\alpha_{xx}, \alpha_{yy}, \alpha_{zz}$
$B_{1g}$	1	1	-1	-1	1	1	-1	-1	$R_z$	$\alpha_{xy}$
$B_{2g}$	1	-1	1	-1	1	-1	1	-1	$R_y$	$\alpha_{xz}$
$B_{3g}$	1	-1	-1	1	1	-1	-1	1	$R_x$	$\alpha_{yz}$
$A_u$	1	1	1	1	-1	-1	-1	-1		
$B_{1u}$	1	1	-1	-1	-1	-1	1	1	$T_z$	
$B_{2u}$	1	-1	1	-1	-1	1	-1	1	$T_y$	
$B_{3u}$	1	-1	-1	1	-1	1	1	-1	$T_x$	

Table 3.2 Table used to correlate the site symmetry of the calcium ions ( $C_s$ ), as well as the carbonate ions ( $C_s$ ), to the symmetry of the unit cell ( $D_{2h}$ ) in aragonite.

$D_{2h}$	$C_s/\sigma_{yz}$
$A_g$	$A'$
$B_{1g}$	$A''$
$B_{2g}$	$A''$
$B_{3g}$	$A'$
$A_u$	$A''$
$B_{1u}$	$A'$
$B_{2u}$	$A'$
$B_{3u}$	$A''$

Table 3.3 Table used to correlate the point group symmetry of the free carbonate ions ( $D_{3h}$ ) to their site symmetry ( $C_s$ ) in aragonite.

$D_{3h}$	$C_s/\sigma_{yz}$
$A_1'$	$A'$
$A_2'$	$A''$
$E'$	$A'+A''$
$A_1''$	$A''$
$A_2''$	$A'$
$E''$	$A'+A''$

Table 3.4 Character table for the  $D_{3d}^6$  space group of calcite.

$D_{3d}^6$	E	$2C_3$	$3C_2$	I	$2S_6$	$3\sigma_d$		
$A_{1g}$	1	1	1	1	1	1		$\alpha_{xx} + \alpha_{yy}, \alpha_{zz}$
$A_{2g}$	1	1	-1	1	1	-1	$R_z$	
$E_g$	2	-1	0	2	-1	0	$(R_x, R_y)$	$(\alpha_{xx} - \alpha_{yy}, \alpha_{xy}), (\alpha_{xz}, \alpha_{yz})$
$A_{1u}$	1	1	1	-1	-1	-1		
$A_{2u}$	1	1	-1	-1	-1	1	$T_z$	
$E_u$	2	-1	0	-2	1	0	$(T_x, T_y)$	

Table 3.5 Table used to correlate the site symmetry of the calcium ions ( $S_6$ ) to the symmetry of the unit cell ( $D_{3d}$ ) in calcite.

$D_{3d}$	$S_6$
$A_{1g}$	$A_g$
$A_{2g}$	$A_g$
$E_g$	$E_g$
$A_{1u}$	$A_u$
$A_{2u}$	$A_u$
$E_u$	$E_u$

Table 3.6 Table used to correlate the point group symmetry of the free carbonate ions ( $D_{3h}$ ) to their site symmetry ( $D_3$ ) in calcite.

$D_{3h}$	$D_3$
$A_1'$	$A_1$
$A_2'$	$A_2$
$E'$	$E$
$A_1''$	$A_1$
$A_2''$	$A_2$
$E''$	$E$

Table 3.7 Table used to correlate the site symmetry of the carbonate ions ( $D_3$ ) to the symmetry of the unit cell ( $D_{3d}$ ) in calcite.

$D_{3d}$	$D_3$
$A_{1g}$	$A_1$
$A_{2g}$	$A_2$
$E_g$	$E$
$A_{1u}$	$A_1$
$A_{2u}$	$A_2$
$E_u$	$E$

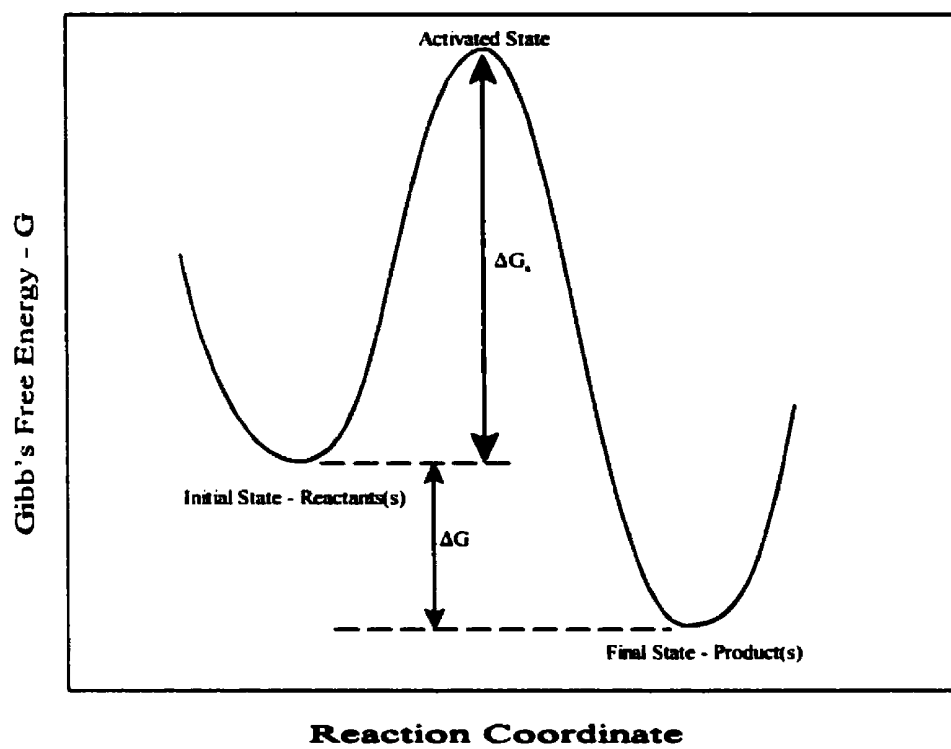


Figure 3.1 Reaction profile diagram showing how the potential energy of the reactant(s) change during the course of a chemical reaction.

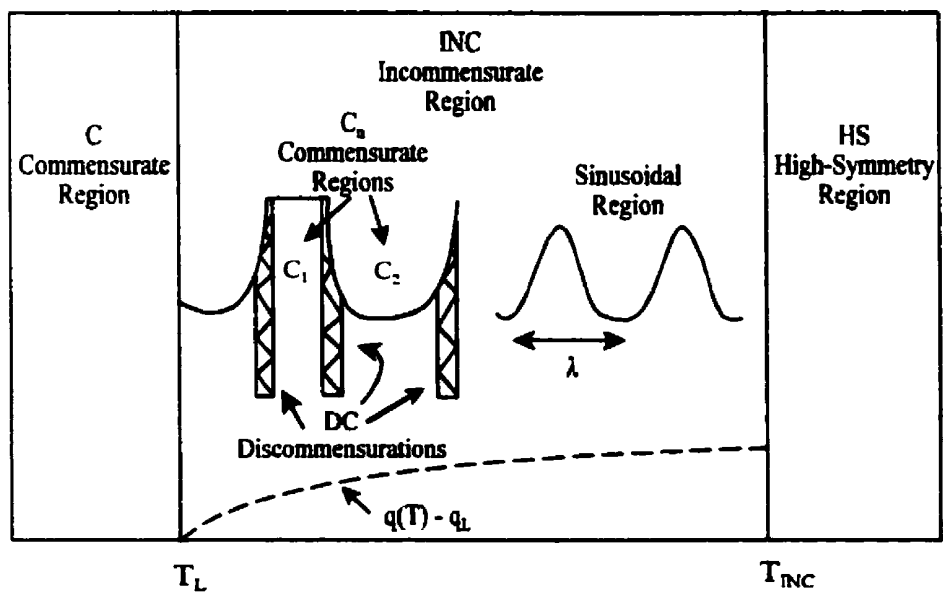


Figure 3.2 Schematic representation (Adapted from Tolédano and Tolédano, 1987) of the distinguishing features of an incommensurate phase.

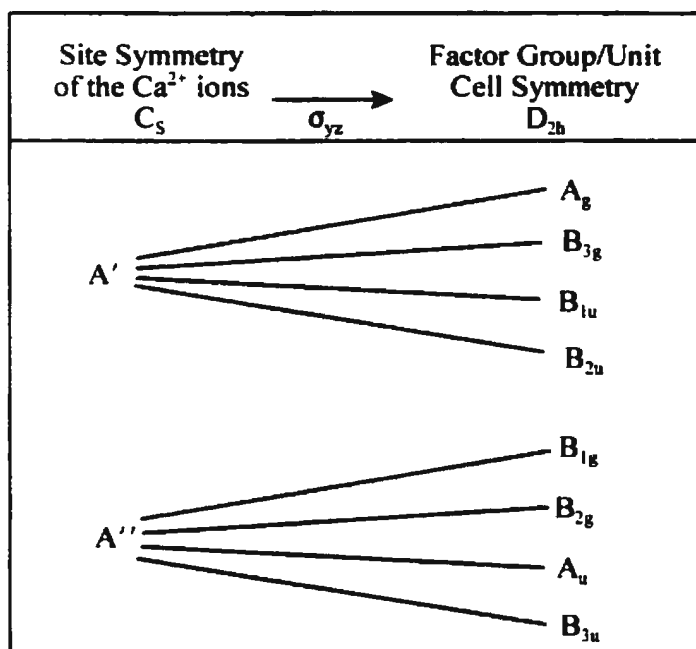


Figure 3.3 Correlation between the site symmetry of the calcium ions ( $C_s$ ) and the symmetry of the unit cell ( $D_{2h}$ ) in aragonite.

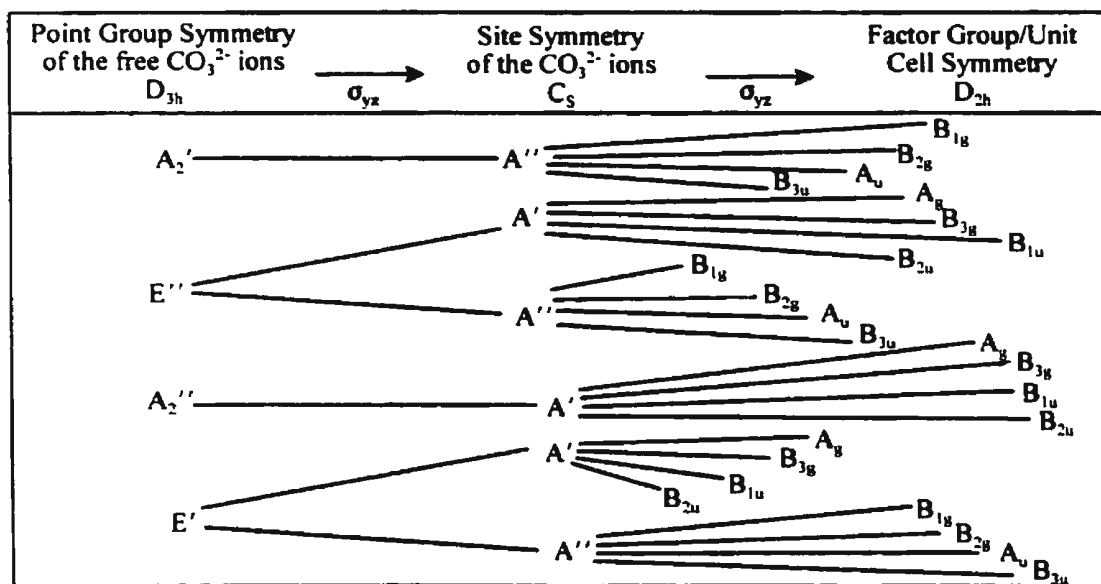


Figure 3.4 Correlation (external vibrational modes only) between the point group symmetry of the free carbonate ions ( $D_{3h}$ ), their site symmetry ( $C_s$ ) and the symmetry of the unit cell ( $D_{2h}$ ) in aragonite.

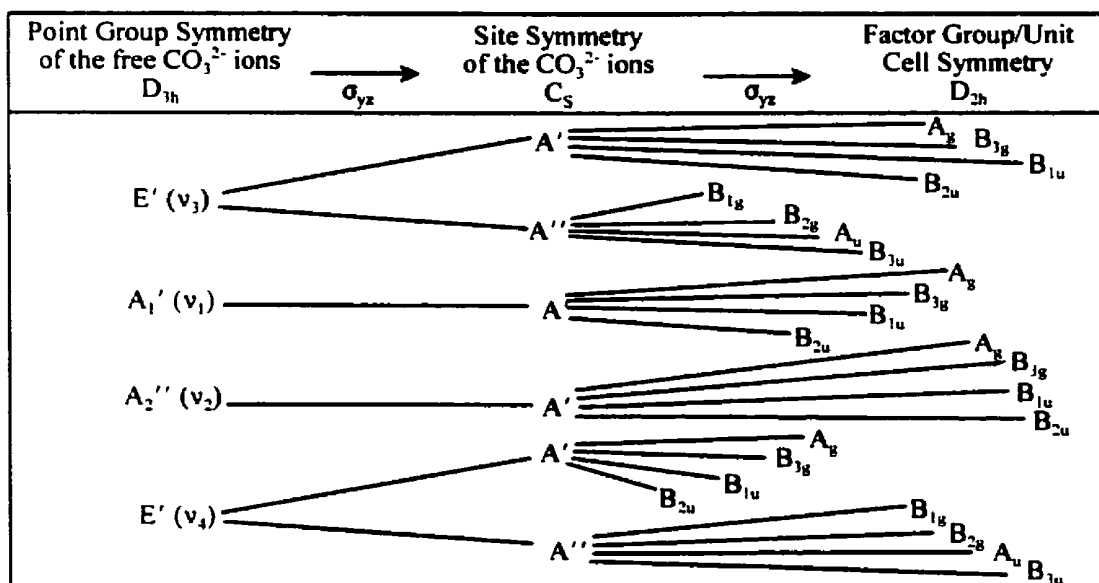


Figure 3.5 Correlation (internal vibrational modes only) between the point group symmetry of the free carbonate ions ( $D_{3h}$ ), their site symmetry ( $C_s$ ) and the symmetry of the unit cell ( $D_{2h}$ ) in aragonite.

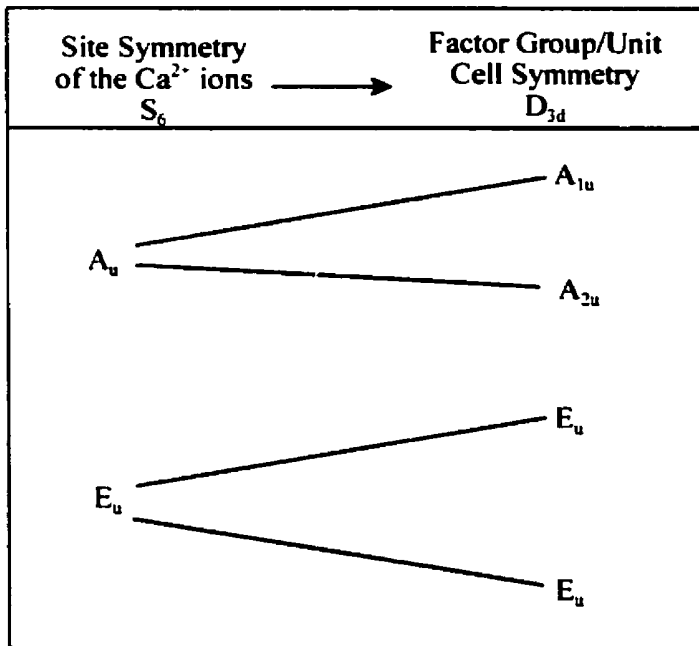


Figure 3.6 Correlation between the site symmetry of the calcium ions ( $S_6$ ) and the symmetry of the unit cell ( $D_{3d}$ ) in calcite.

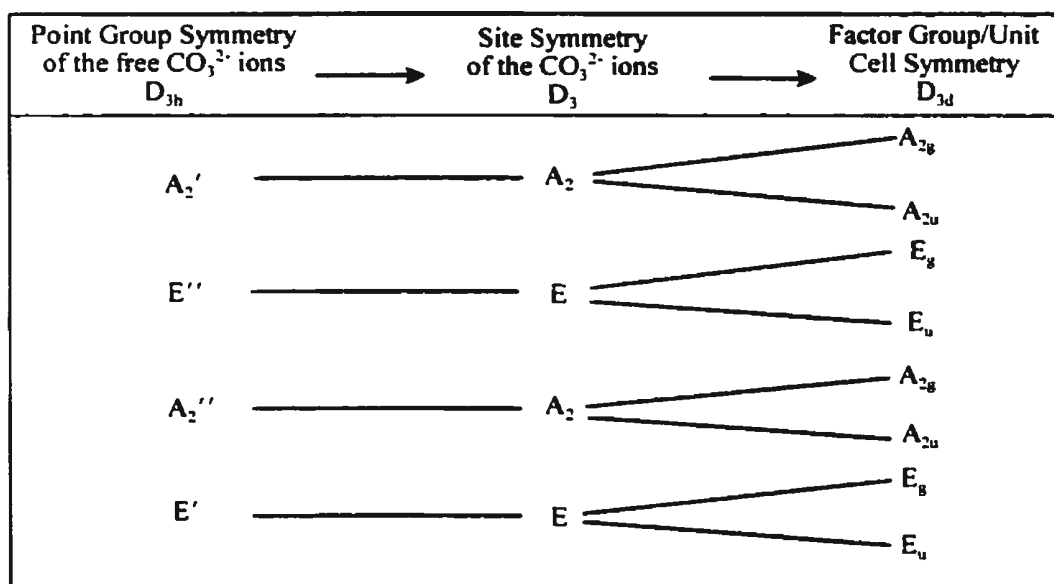


Figure 3.7 Correlation (external vibrational modes only) between the point group symmetry of the free carbonate ions ( $D_{3h}$ ), their site symmetry ( $D_3$ ) and the symmetry of the unit cell ( $D_{3d}$ ) in calcite.

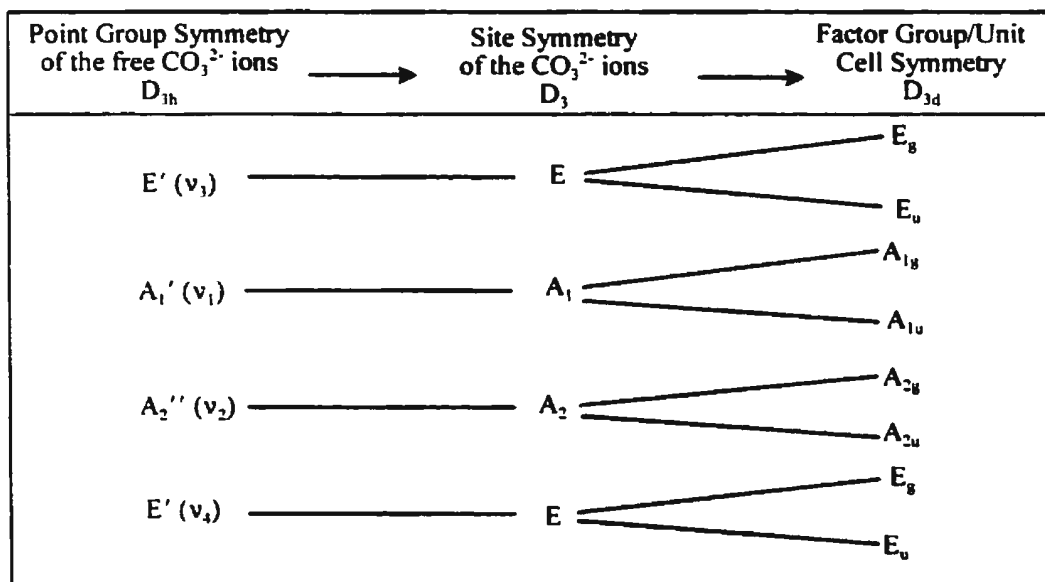


Figure 3.8 Correlation (internal vibrational modes only) between the point group symmetry of the free carbonate ions ( $D_{3h}$ ), their site symmetry ( $D_3$ ) and the symmetry of the unit cell ( $D_{3d}$ ) in calcite.

## **Chapter 4**

### **Results and Discussion**

#### **4.1 Calcium Carbonate Hexahydrate**

##### **4.1.1 Preparation**

Calcium carbonate hexahydrate is unstable with respect to calcite at all temperatures above 0 °C. However, at temperatures below 3 °C, slow precipitation of calcium carbonate leads to the formation of a milk-like suspension. Upon the immediate filtration of this milk-like suspension, crystals of  $\text{CaCO}_3 \cdot 6\text{H}_2\text{O}$  may be isolated. These precipitates were found to be almost pure  $\text{CaCO}_3 \cdot 6\text{H}_2\text{O}$  by optical microscopy and Raman spectroscopy.

##### **4.1.2 Morphological Studies**

The  $\text{CaCO}_3 \cdot 6\text{H}_2\text{O}$  prepared in this manner consists of well-defined tablets of "hexagonally-shaped" crystals. Photomicrographs presented in Figures 4.1 and 4.2 show these "hexagonally-shaped" tablets of  $\text{CaCO}_3 \cdot 6\text{H}_2\text{O}$ , 7-45  $\mu\text{m}$  in length, immediately after the precipitation.

##### **4.1.3 Raman Spectroscopic Data**

The Raman spectrum of  $\text{CaCO}_3 \cdot 6\text{H}_2\text{O}$  has not been previously established in the literature. This is probably due to its relative instability and short life-span. However, the X-ray diffraction pattern is known (Brooks *et al.*, 1950) and its crystal structure is believed to be that of a well-ordered crystal (Adams, 1974).

The Raman spectrum of the external lattice mode region and  $\nu_4$  internal vibrational mode region of  $\text{CaCO}_3 \cdot 6\text{H}_2\text{O}$  is presented in Figure 4.3. The presence of an external vibrational mode at  $269.1 \text{ cm}^{-1}$  is indicative of the order within the crystal structure since disordered structures have only a broad Rayleigh line. The  $\nu_4$  bending mode at  $721.4 \text{ cm}^{-1}$  has a relatively small FWHH of  $9.5 \text{ cm}^{-1}$  which is also indicative of structural order (Figure 4.3a and Table 4.1). Two other peaks are also present at  $587.1$  and  $643.3 \text{ cm}^{-1}$ , but are believed to be due to wagging vibrations of water.

The Raman spectrum is dominated by the  $\nu_1$  symmetric stretching vibration of the  $\text{CO}_3^{2-}$  ion in the  $1000\text{-}1150 \text{ cm}^{-1}$  region (Figure 4.4). The single peak observed for  $\nu_1$  at  $1071.0 \text{ cm}^{-1}$ , with a FWHH of  $5.5 \text{ cm}^{-1}$ , suggests well-defined structural order within the  $\text{CaCO}_3 \cdot 6\text{H}_2\text{O}$  crystal (Figure 4.4a).

The next region of the spectrum contains the  $\nu_3$  antisymmetric stretching region and the  $2\nu_2$  overtone region of the carbonate ion, as well as the  $\nu_2$  region of water (Figure 4.5). The  $\nu_3$  vibrational mode is present as a single, sharp band with a maximum at  $1415.1 \text{ cm}^{-1}$ . The relatively small FWHH observed for the  $\nu_3$  band at  $53.1 \text{ cm}^{-1}$  is also indicative of structural order (Figure 4.5a and Table 4.1). However, the  $2\nu_2$  overtone region is broad and consists of two components,  $1610.9$  and  $1730.8 \text{ cm}^{-1}$  (Figure 4.5a and Table 4.1). The  $\nu_2$  of water is Raman-active at  $\approx 1650 \text{ cm}^{-1}$ , but may be lower (i.e.  $1610.9 \text{ cm}^{-1}$ ) due to hydrogen bonding to the  $\text{CO}_3^{2-}$  ion. The  $\nu_2$  of  $\text{CO}_3^{2-}$  is infrared-active at  $\approx 860 \text{ cm}^{-1}$  and this may give rise to the  $2\nu_2$  of  $\text{CO}_3^{2-}$  observed at  $1730.8 \text{ cm}^{-1}$ .

An overview spectrum is presented in Figure 4.6 which displays the region from  $1000\text{-}$

4000  $\text{cm}^{-1}$ . The O-H stretching region of  $\text{H}_2\text{O}$  at 3400  $\text{cm}^{-1}$  consists of two major components which, upon curve fitting, were fitted to five distinct bands, 3180.0, 3262.6, 3346.0, 3436.9 and 3473.9  $\text{cm}^{-1}$  (Figures 4.6a and 4.6b, and Table 4.1). The presence of these well-defined peaks may be due to intermolecular coupling or Fermi resonance with  $2\nu_2$ , but nothing definite can be said. Regardless of the origin of these two well-defined bands, they are still indicative of the structural order within  $\text{CaCO}_3 \cdot 6\text{H}_2\text{O}$  (Buanam-Om-Danvirutai and Luck, 1987).

#### **4.1.4 Thermoanalytical Measurements**

The following dehydration reaction,  $\text{CaCO}_3 \cdot 6\text{H}_2\text{O} - \text{CaCO}_3 \cdot 1\text{H}_2\text{O}$ , was studied by DSC (Figure 4.7). The hexahydrate was heated from 25-120  $^\circ\text{C}$  at a rate of 10  $^\circ\text{C}/\text{minute}$ . The dehydration reaction was found to be endothermic ( $\Delta H = 1336 \text{ J} \cdot \text{g}^{-1}$ ;  $T = 35.2 \text{ }^\circ\text{C}$ ). Raman spectroscopy performed before and after heating was used to identify the initial and final products of the dehydration reaction. Mass measurements (Table 4.2) were also employed to determine the number of included waters lost during the dehydration reaction.

## **4.2 Calcium Carbonate Monohydrate**

### **4.2.1 Preparation**

At temperatures between 3-10  $^\circ\text{C}$ , precipitation of calcium carbonate leads to the formation of a unique thixotropic suspension. Immediate filtration of this thixotropic suspension yields damp crystals of amorphous calcium carbonate monohydrate. The  $\text{CaCO}_3 \cdot 1\text{H}_2\text{O}$  crystals prepared in this manner were found to be highly contaminated with other phases such as  $\text{CaCO}_3 \cdot 6\text{H}_2\text{O}$ , calcite and vaterite. These impurities were detected by

optical microscopy and Raman spectroscopy.

In order to obtain relatively pure crystals of  $\text{CaCO}_3 \cdot 1\text{H}_2\text{O}$ , it was necessary to allow pure crystals of  $\text{CaCO}_3 \cdot 6\text{H}_2\text{O}$  to stand for a period of 24 hours. The slow dehydration process produced a relatively pure  $\text{CaCO}_3 \cdot 1\text{H}_2\text{O}$  crystals.

#### 4.2.2 Morphological Studies

The  $\text{CaCO}_3 \cdot 1\text{H}_2\text{O}$  prepared from the spontaneous dehydration of  $\text{CaCO}_3 \cdot 6\text{H}_2\text{O}$  consisted of distorted tablets of "hexagonally-shaped" crystals. These crystals had a cloudy appearance which was probably due to the dehydration reaction of the hexahydrate. A photomicrograph is presented in Figure 4.8 to show these distorted, "hexagonally-shaped" tablets of  $\text{CaCO}_3 \cdot 1\text{H}_2\text{O}$ , 3-25  $\mu\text{m}$  in length, immediately after dehydration. The distorted shape of these crystals is believed to be a consequence of the dehydration process.

#### 4.2.3 Raman Spectroscopic Data

As was the case with  $\text{CaCO}_3 \cdot 6\text{H}_2\text{O}$ , the Raman spectrum of  $\text{CaCO}_3 \cdot 1\text{H}_2\text{O}$  has also not been previously reported in the literature. It has been suggested that the crystal structure of the monohydrate is of a disordered nature because of the presence of broad X-ray diffraction peaks of relatively low intensities (Brooks *et al.*, 1950).

By definition, disordered crystals lack translational symmetry, either partially or completely. Consequently, the lack of external vibrational modes in the Raman spectrum of the monohydrate (Figure 4.9) suggests structural disorder within the crystal lattice. Figure 4.9 also shows the presence of a broad band, consisting of at least two components, 696.8 and 727.3  $\text{cm}^{-1}$  (Figure 4.9a and Table 4.3), in the  $\nu_4$  region. This region is analogous to the

Raman spectrum of the  $\nu_4$  region of molten and solid  $\text{Li}_2\text{CO}_3$ , which are known to exhibit partial disorder of the  $\text{CO}_3^{2-}$  ion sublattice (Bates *et al.*, 1972).

The symmetric stretching vibrational mode region presented in Figure 4.10 shows a single broad band at  $1081.7 \text{ cm}^{-1}$  with a relatively large FWHH of  $29.9 \text{ cm}^{-1}$  (Figure 4.10a and Table 4.3). The large half width suggests structural disorder because the  $\nu_1$  mode is extremely sensitive to changes in the structural environment.

The next region of the spectrum contains the  $\nu_3$  antisymmetric stretching region and the  $2\nu_2$  overtone region of the carbonate ion, as well as the  $\nu_2$  region of water (Figure 4.11). The  $\nu_3$  bending mode is very broad and consists of at least three components,  $1412.0$ ,  $1482.3$  and  $1544.1 \text{ cm}^{-1}$  (Figure 4.11a and Table 4.3). As was the case with the  $\nu_4$  region of  $\text{CaCO}_3 \cdot \text{H}_2\text{O}$ , the  $\nu_3$  region also shows features similar to those found in the Raman spectrum of the  $\nu_3$  region of molten and solid  $\text{Li}_2\text{CO}_3$  (Bates *et al.*, 1972). The lack of a single, well-defined band in the  $\nu_3$  region suggests some structural disorder. The  $2\nu_2$  overtone region is also broad and consists of two components,  $1649.6$  and  $1737.4 \text{ cm}^{-1}$  (Figure 4.11a and Table 4.3). The  $\nu_2$  of water is Raman-active at  $\approx 1650 \text{ cm}^{-1}$  which may correspond to the  $1649.6 \text{ cm}^{-1}$  band. The  $\nu_2$  of  $\text{CO}_3^{2-}$  is infrared-active at  $\approx 860 \text{ cm}^{-1}$  and this may give rise to the  $2\nu_2$  of  $\text{CO}_3^{2-}$  at approximately  $1737.4 \text{ cm}^{-1}$ . Unlike the  $2\nu_2$  region in  $\text{CaCO}_3 \cdot 6\text{H}_2\text{O}$ , the  $2\nu_2$  region in  $\text{CaCO}_3 \cdot \text{H}_2\text{O}$  is not as complicated because there are five fewer water molecules in the formula of the monohydrate.

An overview spectrum is presented in Figure 4.12 which displays the region from  $1000\text{--}4000 \text{ cm}^{-1}$ . The O-H stretching region of  $\text{H}_2\text{O}$  does not consist of well-defined distinct

bands as in  $\text{CaCO}_3 \cdot 6\text{H}_2\text{O}$ , but rather consists of three relatively broad bands, 3008.1, 3217.4 and  $3447.6 \text{ cm}^{-1}$  (Figures 4.12a and 4.12b, and Table 4.3). These observations also suggest that the crystal structure of the monohydrate is not as well-ordered as the hexahydrate.

#### **4.2.4 Thermoanalytical Measurements**

The transformation reaction of  $\text{CaCO}_3 \cdot \text{H}_2\text{O}$  was found to be very complex and depended on the presence of impurity seed crystals of calcite and vaterite. All of the different preparations reacted in the same manner. The majority of the time, vaterite seed crystals co-precipitated with the monohydrate, thus, favouring the transformation to vaterite. However, in some instances, calcite co-precipitated with the monohydrate and, as a result, the transformation led to mainly calcite crystals. Raman spectroscopy performed before and after heating was used to identify the initial and final products of the transformation reaction. Mass measurements (Table 4.4) were also employed to determine the number of included waters lost during the transformation reaction.

### **4.3 Calcite**

#### **4.3.1 Preparation**

Calcite is the thermodynamically stable form of  $\text{CaCO}_3$  under ambient conditions to which all other phases transform given sufficient time. At temperatures between 15-25 °C, precipitation of calcium carbonate leads to the formation of a milk-like suspension. After a time period of 24 hours, filtration of this milk-like suspension yields crystals of calcite. These precipitates were found to be relatively pure by optical microscopy and Raman spectroscopy.

### 4.3.2 Morphological Studies

The calcite prepared using the above procedure consists of well-defined rhombohedral-shaped crystals. A scanning electron micrograph is presented in Figure 4.13 showing these rhombohedral crystals of calcite, 6-8  $\mu\text{m}$  in length, immediately after the precipitation.

Calcite was also prepared by the transformation reactions,  $\text{CaCO}_3 \cdot 6\text{H}_2\text{O} \rightarrow \text{CaCO}_3 \cdot \text{H}_2\text{O} \rightarrow \text{calcite}$  at 25  $^\circ\text{C}$ . In this case, well-defined tablets of "hexagonally-shaped" crystals of calcite were obtained. However, the transformation rates may be slow (i.e. 1-3 months) and seem to depend upon the humidity and temperature. A scanning electron micrograph is presented in Figure 4.14 showing these distorted, "hexagonally-shaped" tablets of calcite, 7-45  $\mu\text{m}$  in length, immediately after the transformation reactions had occurred. The hexagonal shape of these crystals, compared to the normal rhombs, appears to be a suitable way to establish the origin of the calcite.

### 4.3.3 Raman Spectroscopic Data

The Raman spectrum of calcite is well-known at ambient conditions. Calcite belongs to the space group  $D_{3d}^6$  and symmetry analysis reveals that there are 30 normal modes of vibration for the rhombohedral unit cell. Detailed spectroscopic analyses of calcite have been reported (Anderson, 1996; Gillet *et al.*, 1993; Gillet *et al.*, 1996; White, 1974). The Raman spectra of natural calcite are presented for comparative purposes with the other phases. Overview spectra are presented in Figures 4.15 and 4.16 which display the regions from 100-1150  $\text{cm}^{-1}$  and 1300-2000  $\text{cm}^{-1}$  respectively. The presence of well-defined external (100-300

cm<sup>-1</sup>) and internal vibrational bands ( $\nu_4 = 713.9 \text{ cm}^{-1}$ ,  $\nu_1 = 1086.6 \text{ cm}^{-1}$ ,  $\nu_3 = 1435.8 \text{ cm}^{-1}$  and  $2\nu_2 = 1748.7 \text{ cm}^{-1}$ ) with relatively small FWHH's suggest a well-ordered crystal structure. The observed Raman band frequencies for calcite are compared with literature values in Table 4.5.

#### **4.4 Vaterite**

##### **4.4.1 Preparation**

Vaterite is the least stable and most soluble of the anhydrous calcium carbonate polymorphs. At temperatures between 25-40 °C, precipitation of calcium carbonate leads to the formation of a milk-like suspension. The immediate filtration of this milk-like suspension yields a relatively pure powder of vaterite. Since no calcite could be detected by optical microscopy, Raman spectroscopy or XRD, it can be concluded that the purity of the vaterite was better than 99 %. Although other methods of preparation have been reported (Section 1.2), this is the only known method for preparing pure precipitates of vaterite without impurity phases.

The transformation reaction,  $\text{CaCO}_3 \cdot 1\text{H}_2\text{O} \rightarrow \text{CaCO}_3$  also gives crystals of vaterite in some cases. The endothermic reaction rate for the dehydration of  $\text{CaCO}_3 \cdot 1\text{H}_2\text{O}$  was found to be extremely sensitive to temperature, and to the inclusion of small quantities of water and other  $\text{CaCO}_3$  phases which co-precipitated with the original  $\text{CaCO}_3 \cdot 6\text{H}_2\text{O}$ . However, depending on the humidity and temperature, the transformation rates may be slow (i.e. 1-3 months). Usually, the vaterite crystals prepared in the latter manner were found to be relatively pure. However, in some instances, 1-2 % calcite was found. This was confirmed

using optical microscopy, Raman spectroscopy and XRD.

#### 4.4.2 Morphological Studies

These preparations both result in the formation of spherical aggregates of crystals known as spherulites (Brooks *et al.*, 1950; Maciejewski *et al.*, 1994). Figures 4.17-4.18 and 4.19-4.20 are photomicrographs and scanning electron micrographs of the vaterite spherulites respectively. The aggregated vaterite crystals are of length 2-12  $\mu\text{m}$ .

#### 4.4.3 Raman Spectroscopic Data

A definitive crystal structure determination of vaterite has not been established. This is probably due to the lack of crystals of sufficient size and purity required for single crystal studies. However, a number of possible hexagonal crystal structures have been proposed which differ in the number of formula units and in the coordination of the  $\text{CO}_3^{2-}$  sublattice in the vaterite unit cell: [1]  $D_6^6$  with  $Z = 6$  (Bradley *et al.*, 1966), [2]  $D_{6h}^4$  with  $Z = 6$  (Kamhi, 1963; McConnell, 1960; White, 1974) and [3]  $D_{6h}^4$  with  $Z = 12$  (Kamhi, 1963; Meyer, 1969).

Overview spectra are presented in Figures 4.21 and 4.22 which display the regions from 100-1150  $\text{cm}^{-1}$  and 1300-2000  $\text{cm}^{-1}$  respectively. In the external vibrational mode region (100-400  $\text{cm}^{-1}$ ), at least nine Raman bands were observed for vaterite compared to only two bands for calcite. The presence of a relatively large number of lattice bands in vaterite appears to be consistent with the structure proposed by Meyer, in which  $Z = 12$ . This differs greatly from the relatively small number of formula units in the unit cell of calcite ( $Z = 2$ ). Because vaterite gives rise to distinct bands in both the external and internal vibrational mode regions,

it can easily be distinguished from the other forms of CaCO<sub>3</sub> using Raman spectroscopy. A detailed spectroscopic analysis of vaterite will be given in Section 4.6.

#### **4.4.4 Thermoanalytical Measurements**

The polymorphic transformation of vaterite into calcite has been reported in several papers (Chakraborty *et al.*, 1994; Kralj *et al.*, 1997; Maciejewski *et al.*, 1994; Northwood and Lewis, 1968; Perić *et al.*, 1996; Tarits *et al.*, 1990). From our DSC studies (Figure 4.23), determined from experiments performed under non-isothermal conditions, the enthalpy of the polymorphic transformation ( $\Delta H_t$ ) of vaterite at  $T = 442.7$  °C was found to be  $-20.147$  J·g<sup>-1</sup>. This is in good agreement to the value determined by Perić *et al.* (1996) for the exothermic reaction,  $\Delta H_t = -21.2$  J·g<sup>-1</sup>.

One unexpected result of this study was the identification of water in the vaterite. DSC and mass loss analyses have shown a total loss of 0.129 moles of water corresponding to the loss of absorbed and trapped water (0.026 and 0.103 moles respectively). TG-EGA analyses have also shown a loss of mass corresponding to about 2 %. Mass measurements (Table 4.6) and Raman spectroscopy (Figure 4.24) performed before and after heating were also used to confirm the loss of included water.

### **4.5 Aragonite**

#### **4.5.1 Preparation**

Aragonite is thermodynamically favoured at low temperatures and high pressures. Under ambient conditions, it only differs slightly from calcite in terms of thermodynamic stability (Blackburn and Dennen, 1994). At temperatures between 60-90 °C, precipitation of

calcium carbonate leads to the formation of a milk-like suspension. The immediate filtration of this milk-like suspension yields crystals of aragonite. These precipitates were also found to be relatively pure as confirmed by optical microscopy and Raman spectroscopy.

#### **4.5.2 Morphological Studies**

The above preparation results in the formation of "needle-like" crystals of aragonite. Photomicrographs presented in Figures 4.25 and 4.26 show these "needle-like" crystals of aragonite, 10-60  $\mu\text{m}$  in length, immediately after the precipitation.

#### **4.5.3 Raman Spectroscopic Data**

As is the case with calcite, the Raman spectrum of aragonite is also well-known at ambient conditions. Aragonite belongs to the space group  $D_{2h}^{16}$  and symmetry analysis reveals that there are 60 normal modes of vibration for the orthorhombic unit cell. Detailed spectroscopic analyses of aragonite have been reported (Anderson, 1996; Gillet *et al.*, 1993; Gaudie *et al.*, 1997; White, 1974). The Raman spectra of natural aragonite are presented for comparative purposes with the other phases. Overview spectra are presented in Figures 4.27 and 4.28 which display the regions from 100-1150  $\text{cm}^{-1}$  and 1300-2000  $\text{cm}^{-1}$  respectively. In aragonite, the site symmetry of the  $\text{CO}_3^{2-}$  ion is reduced to  $C_s$ . This alters the selection rules permitting the activity of the  $\nu_1$  vibrational mode and results in the splitting of the two doubly-degenerate modes,  $\nu_3$  and  $\nu_4$ , into pairs of non-degenerate modes. The observed Raman band frequencies for aragonite are compared with literature values in Table 4.7.

#### **4.6 A Detailed Spectroscopic Analysis of Vaterite**

Vaterite has received much attention in the literature because it is a rare form of

calcium carbonate and because of its unusual crystal structure. Due to the presence of a small number of weak superstructure reflections in the XRD pattern of vaterite indicating some degree of long-range ordering, Kamhi (1963) has proposed a hexagonal cell with twelve formula units of  $\text{CaCO}_3$ . Meyer's (1969) proposed structure for vaterite agrees in general with Kamhi's proposal, but suggests a disordered stacking sequence of the  $\text{CO}_3^{2-}$  ion sublattice. Based on the limited crystal structure information, and on the nature of the Raman and infrared spectra, we suggest the possibility that vaterite is an incommensurate phase.

Raman and infrared vibrational frequencies, half widths and assignments for vaterite are collected in Tables 4.8 and 4.9 respectively, along with literature values for comparative purposes. In general, the present results are in good agreement with previous Raman spectra, but the improved signal-to-noise suggests a very complicated structure. Raman spectra have been measured at 77 K and 298 K. The Raman and infrared spectra of vaterite were found to be similar to those obtained for  $\gamma\text{-Na}_2\text{CO}_3$  (Brooker and Bates, 1971). These new spectra of vaterite have allowed the detection of bands, not previously obtained, that provide further evidence to support our proposed crystal structure.

#### **4.6.1 External Lattice Modes**

The external lattice mode regions of the anhydrous calcium carbonates are remarkably different. Unlike calcite and aragonite, vaterite exhibits a relatively large number of broad bands in the  $100\text{-}400\text{ cm}^{-1}$  region of the Raman spectrum (Figures 4.29 and 4.29a). The density of states observed for this region of vaterite is rather large at about  $250\text{ cm}^{-1}$ . The unique lattice bands of vaterite, 116.6, 130.3, 151.5, 172.9, 190.0, 208.4, 266.4, 301.7 and

332.5  $\text{cm}^{-1}$ , are less intense and much broader than those of calcite and aragonite. Both of these findings suggest a more disrupted crystal lattice for vaterite. If, as proposed by Meyer, the structure is fully disordered, it would lead to overlapping features in the external vibrational mode region and possibly a single broad peak. The effects of a fully-disordered crystal structure would be similar to that observed for  $\text{CaCO}_3 \cdot \text{H}_2\text{O}$  which has no discrete external lattice bands. However, our results suggest that vaterite is not fully disordered, but has partial disordering of the  $\text{CO}_3^{2-}$  ions. This is indicative of an incommensurate crystal structure.

#### **4.6.2 Internal Vibrational Modes**

The unperturbed  $\text{CO}_3^{2-}$  ion has  $D_{3h}$  symmetry and would result in the following assignments and relative frequencies respectively:  $\nu_4$  ( $E'$ ) infrared- and Raman-active, antisymmetric bend at 700  $\text{cm}^{-1}$ ;  $\nu_2$  ( $A_2''$ ) infrared-active, out-of-plane deformation at 860  $\text{cm}^{-1}$ ;  $\nu_1$  ( $A_1'$ ) Raman-active, symmetric stretch at 1090  $\text{cm}^{-1}$ ;  $\nu_3$  ( $E'$ ) infrared- and Raman-active, antisymmetric stretch at 1400  $\text{cm}^{-1}$  (Brooker and Bates, 1971). In the vibrational spectra of vaterite, significant deviations from the free  $\text{CO}_3^{2-}$  ion approximation method are observed.

##### **4.6.2.1 $\nu_4$ - Antisymmetric Bend**

In the region of the  $\nu_4$  vibrational mode, the Raman spectrum presented in Figure 4.30 shows a removal of the degeneracy. This results in two regions, about 675 and 750  $\text{cm}^{-1}$ , with differing intensities, over a very large density of states of about 100  $\text{cm}^{-1}$ . Each of these regions also contains three components (667.2, 674.0 and 684.8  $\text{cm}^{-1}$ , and 738.4, 743.5 and

751.3  $\text{cm}^{-1}$  respectively) as presented in Figure 4.30a. It is believed these three components correspond to at least three different groups of carbonate ions in the unit cell of vaterite.

The infrared spectra of the  $\nu_4$  region presented in Figures 4.31 and 4.32 show features similar to those found in the  $\nu_4$  region of the Raman spectrum of vaterite. There is a removal of the degeneracy giving two distinct regions (670 and 745  $\text{cm}^{-1}$  respectively) with an observed density of states of about 100  $\text{cm}^{-1}$ . The lower wavenumber region consists of four components, 660.2, 666.5, 673.8 and 680.8  $\text{cm}^{-1}$ , and the higher wavenumber region consists of three components, 739.0, 744.1 and 749.5  $\text{cm}^{-1}$  (Figures 4.31a and 4.32a respectively).

The coincidence of frequencies of all of the components of the  $\nu_4$  band in the Raman and infrared spectra of vaterite suggest that the centrosymmetric crystal structures proposed cannot be correct (Kamhi, 1963; Meyer, 1969). It seems more likely the crystal structure of vaterite is non-centrosymmetric as proposed by Lippmann (1973).

#### 4.6.2.2 $\nu_2$ - Out-of-Plane Deformation

The Raman spectrum of the  $\nu_2$  vibrational mode region, presented in Figure 4.33, shows the presence of a previously unreported band at about 875  $\text{cm}^{-1}$ . Figure 4.33a shows the presence of at least three components in this relatively low intensity band, 881.0, 877.6 and 873.7  $\text{cm}^{-1}$ . The observed density of states for this band is about 20  $\text{cm}^{-1}$ .

The infrared spectrum of the  $\nu_2$  region, presented in Figure 4.34, also shows three components, 871.2, 876.9 and 883.7  $\text{cm}^{-1}$ . However, the  $\nu_2$  region is much more pronounced in the infrared and has a density of states of about 30  $\text{cm}^{-1}$  (Figure 4.34a). Furthermore, the coincidence of Raman and infrared frequencies for the  $\nu_2$  bands also suggests a non-

centrosymmetric crystal structure.

Additional bands in the regions of non-degenerate modes, such as  $\nu_2$  and  $\nu_1$ , can only result from the coupling of identical normal modes of vibration of different molecules in the unit cell (i.e. correlation field coupling), or the ordered distribution of molecules over sets of non-equivalent sites. The latter gives rise to a number of bands equal to the number of different occupied sites (Brooker and Bates, 1971).

When the peak of the dilute isotopomer is shifted outside the density of states of the host crystal, the vibration of the isotopomer will be decoupled from the analogous vibration of the crystal and correlation field effects will be absent (Brooker and Chen, 1991; Gillet *et al.*, 1996). Static field effects such as multiple site occupancy will remain (Brooker and Wang, 1992).

A number of bands were observed in the  $^{13}\text{C}$  region of the infrared spectrum of the  $\nu_2$  vibrational mode. The  $^{13}\text{C}$  isotopic substitution effects for the  $\nu_2$  region are presented in Figure 4.35. Five distinct bands were observed for the uncoupled  $^{13}\text{CO}_3^{2-}$  species, 844.2, 849.3, 851.0, 855.0 and 859.8  $\text{cm}^{-1}$ . The presence of more than one band in this region reveals that there is little or no correlation field splitting. Hence, the five  $^{13}\text{CO}_3^{2-}$  bands must be the result of at least five distinct sets of non-equivalent carbonate ion sites. This suggests vaterite to have a relatively large unit cell comprised of at least five  $\text{CaCO}_3$ .

#### 4.6.2.3 $\nu_1$ - Symmetric Stretch

The Raman spectrum of the  $\nu_1$  vibrational mode region is presented in Figure 4.36. Figure 4.36a shows the presence of three peaks at 1075.0, 1081.4 and 1090.9  $\text{cm}^{-1}$ , with

relative intensities 0.40:0.19:1.00 and a density of states of about  $30 \text{ cm}^{-1}$ . Behrens *et al.* (1995) have assigned the middle band at  $1081.4 \text{ cm}^{-1}$  to a calcite impurity. Behrens *et al.* also suggested that the peaks at  $1075.0$  and  $1090.9 \text{ cm}^{-1}$  were due to two different sites. Anderson (1996) argued on the basis of a unit cell group analysis and that the results could also be explained by correlation field coupling. Our results indicate that all three components are due to vaterite and indicate at least three distinct sites.

Our experimental results indicate that the band at  $1081.4 \text{ cm}^{-1}$  is due to vaterite. If it were a calcite impurity, there should be some evidence of a calcite peak in the  $\nu_2$  region at  $713.9 \text{ cm}^{-1}$ , well-separated from the  $\nu_2$  bands of vaterite. Also, the  $\nu_1$  mode of our calcite occurs at  $1086.6 \text{ cm}^{-1}$  which is appreciably higher than the observed band at  $1081.4 \text{ cm}^{-1}$ . Furthermore, vaterite with a calcite impurity is observed to have an additional sharp band at  $1086.6 \text{ cm}^{-1}$ . In addition, the  $\nu_1$  of vaterite in the infrared exhibits the same three component pattern as found in the Raman (Figures 4.37 and 4.37a) with the same relative intensities and frequencies as those found in the Raman spectrum. The  $\nu_1$  of calcite is forbidden and not observed in the infrared.

Another possible explanation is that the  $1081.4 \text{ cm}^{-1}$  component may be due to a  $\text{CaCO}_3 \cdot 1\text{H}_2\text{O}$  impurity. This is a plausible explanation given the frequency of the  $\nu_1$  Raman band of  $\text{CaCO}_3 \cdot 1\text{H}_2\text{O}$  and the observation of water within the vaterite crystals. However, upon heating the vaterite crystals to  $220 \text{ }^\circ\text{C}$ , the water was removed from the Raman spectrum (Figures 4.24 and 4.24a), but the  $1081.4 \text{ cm}^{-1}$  component still remained. Hence, the three components of  $\nu_1$  must be genuine and, therefore, cannot be due to the presence of

other carbonate impurities.

To prove that the three components of  $\nu_1$  were due to static field effects, a sample of  $^{18}\text{O}$ -enriched vaterite was prepared as described in the experimental (Section 2.4). The splitting of the  $\nu_1$  of the isotopomers confirmed that the three bands are from three different static sites. Figure 4.38 shows the Raman spectrum of  $^{18}\text{O}$ -enriched vaterite in the  $\nu_1$  vibrational mode region. The observed pattern is consistent with the calculated pattern (i.e. substituting an  $^{18}\text{O}$  atom for an  $^{16}\text{O}$  atom on a  $\text{CO}_3^{2-}$  ion approximately results in a  $20\text{ cm}^{-1}$  decrease in the frequency for the dilute isotopomer) (Gillet *et al.*, 1996). There are three peaks at  $1036.9$ ,  $1041.2$ , and  $1050.2\text{ cm}^{-1}$  which correspond to the  $\nu_1$  modes of carbonate ions substituted with two  $^{18}\text{O}$  atoms (i.e.  $\text{CaC}^{16}\text{O}^{18}\text{O}_2$ ). There are also three peaks at  $1015.5$ ,  $1021.5$  and  $1029.2\text{ cm}^{-1}$  which correspond to the fully substituted  $^{18}\text{O}$  carbonate ions,  $\text{CaC}^{18}\text{O}_3$ . However, no peaks were observed for the monosubstituted carbonate ions,  $\text{CaC}^{16}\text{O}_2^{18}\text{O}$ . This is due to the large density of states of  $\text{CaC}^{16}\text{O}_3$  which overlaps with the monosubstituted  $\nu_1$  region.

Correlation field coupling would have resulted in only one peak for each of the  $^{18}\text{O}$ -substituted  $\text{CO}_3^{2-}$  ions, all of which would have frequency shifts from the mean value (i.e.  $1083.0\text{ cm}^{-1}$ ) for the three components. Hence, the three peaks observed for isolated  $\text{CaC}^{16}\text{O}^{18}\text{O}_2$  and  $\text{CaC}^{18}\text{O}_3$  in the vaterite matrix suggest a multi-site effect.

From the infrared spectrum of the  $\nu_2$  region of  $\text{Ca}^{13}\text{CO}_3$  presented in Figure 4.35, there appear to be at least five formula units of  $\text{CaCO}_3$  per unit cell of vaterite ( $844.2$ ,  $849.3$ ,  $851.0$ ,  $855.0$  and  $859.8\text{ cm}^{-1}$ ). This also suggests a multi-site effect, complementing the results

obtained in the Raman spectrum for the  $\nu_1$  vibrational mode region of the  $^{18}\text{O}$ -substituted  $\text{CO}_3^{2-}$  ions.

In order to determine the nature of the splitting, the  $\nu_1$  region was studied at 77 K. At 77 K, there was no significant reduction in the half-width of the  $\nu_1$  band. This suggests the splitting is not dependent on the motions of the  $\text{CO}_3^{2-}$  ions (i.e. dynamic splitting), but rather on the positional average (i.e. static splitting).

#### **4.6.2.4 $\nu_3$ - Antisymmetric Stretch**

In the  $\nu_3$  vibrational mode region, the Raman spectrum presented in Figure 4.39 shows a removal of the degeneracy. Six distinct bands were identified, 1421.1, 1440.9, 1459.9, 1480.4, 1555.0 and 1542.3  $\text{cm}^{-1}$ , over a density of states of about 160  $\text{cm}^{-1}$  (Figure 4.39a).

The infrared spectrum of the  $\nu_3$  region presented in Figure 4.40 also shows removal of the degeneracy. This also results in six distinct bands, 1402.1, 1415.0, 1442.1, 1466.8, 1492.0 and 1558.1  $\text{cm}^{-1}$  (Figure 4.40a). However, because of the strong infrared absorption of the  $\nu_3$  mode of the  $\text{CO}_3^{2-}$  ion, the density of states appears to be larger at about 200  $\text{cm}^{-1}$ .

The coincidence of Raman and infrared frequencies for the  $\nu_3$  bands, combined with the number of components observed in each of these regions, both suggest long-range ordering over a number of non-equivalent  $\text{CO}_3^{2-}$  ion sites within the non-centrosymmetric unit cell of vaterite.

#### **4.6.2.5 $2\nu_2$ - Overtone of The Out-of-Plane Deformation Mode ( $\nu_2$ )**

The Raman spectrum of the  $2\nu_2$  overtone region is presented in Figure 4.41. The free ion selection rules in spectroscopy limit the  $2\nu_2$  vibrational mode to being Raman-active only.

As was the case with the  $\nu_2$  and  $\nu_1$  vibrational modes, the  $2\nu_2$  mode also shows a number of components. The  $2\nu_2$  region consists of three components, 1745.6, 1754.4 and 1757.5  $\text{cm}^{-1}$ , with a density of states of about 30  $\text{cm}^{-1}$  (Figure 4.41a). Since these bands correspond to the overtones of the three  $\nu_2$  bands found in the Raman spectrum, it suggests the three bands in the fundamental are genuine and correspond to at least three distinct groups of  $\text{CO}_3^{2-}$  ions within the unit cell of vaterite.

#### **4.6.2.6 [ $\nu_4 + \nu_1$ ] - Combination Band**

The infrared spectrum of the [ $\nu_4 + \nu_1$ ] combination band region is presented in Figure 4.42. The selection rules for the free ion limit the activity of the [ $\nu_4 + \nu_1$ ] vibrational mode to being infrared-active only. As was the case with the  $\nu_4$  and  $\nu_3$  vibrational modes, the [ $\nu_4 + \nu_1$ ] mode is also degenerate. However, this band is also split into two regions, 1755 and 1825  $\text{cm}^{-1}$ , with a density of states of about 120  $\text{cm}^{-1}$ . Each of these regions also consists of three components (1738.7, 1747.3 and 1765.5  $\text{cm}^{-1}$ , and 1814.2, 1821.8 and 1836.1  $\text{cm}^{-1}$  respectively) which show the same intensity patterns as those found in the  $\nu_4$  region of the Raman (Figures 4.42a-4.42d). These findings all suggest a partially disrupted crystal lattice for vaterite characteristic of the static disorder found in incommensurate phase crystals.

#### **4.6.2.7 Water and Manganese(II) Impurities**

Previous studies on vaterite grown from solution have confirmed the presence of 1.28 % water (Perić *et al.*, 1996). The absorbed and trapped water are believed to be a result of the fast precipitation required and is also believed to be a consequence of the relatively open crystal structure of vaterite. Our spectroscopic results have confirmed the presence of

water (Figures 4.23, 4.24, and 4.43, and Table 4.6), as did our DSC and TG-EGA results.

Other studies on  $\text{CaCO}_3$  have indicated the presence of manganese(II) impurities (Mason, 1998). In some of these studies, Raman spectroscopy has been used to suggest these manganese(II) impurities occur as hydrated species,  $\text{Mn}(\text{H}_2\text{O})_6^{2+}$  (Nassrallah-Aboukaïs *et al.*, 1998). However, even though our Raman spectroscopic results have confirmed the presence of manganese(II) impurities (i.e. comparison of fluorescence level intensities in our calcite and vaterite Raman spectra with Raman spectra of calcite containing known concentrations of manganese(II) impurities suggests our manganese(II) content to be approximately 0.08 ppm) within the vaterite crystal structure, it cannot account for all of the water present.

Furthermore, the presence of these water and manganese(II) impurities are not believed to be necessary for the kinetic stability of vaterite. This was confirmed when upon heating the vaterite crystals to 220 °C (Figures 4.24 and 4.24a), the Raman vibrational spectrum of vaterite was unchanged except that the band of water was removed. However, the fluorescence level did increase confirming the initial presence of manganese(II) impurities. Since the manganese(II) fluorescence increased for the dried sample, it suggests the water is not essential for the stability of vaterite and anhydrous manganese(II) impurities in defects will also give rise to the fluorescence. Hence, the presence of these impurities may simply be due to the relatively open structure of vaterite which is able to accommodate and incorporate them (Mason, 1998).

It can be inferred from the above that the calcite formed from vaterite also contained about 2 % water and approximately 0.08 ppm of manganese(II) impurities. This was

confirmed by Raman spectroscopy (Figure 4.44).

Table 4.1 Observed Raman vibrational frequencies ( $\text{cm}^{-1}$ ) for  $\text{CaCO}_3 \cdot 6\text{H}_2\text{O}$  at 25 °C.

Vibrational Mode Region	Frequency in Wavenumbers [ $\text{cm}^{-1}$ ]	Full Width at Half Height [ $\text{cm}^{-1}$ ]
External	269.1	32.1
$\nu_4$	587.1	22.1
	643.3	23.7
	721.4	9.5
$\nu_2$	not observed	not observed
$\nu_1$	1071.0	5.5
$\nu_3$	1415.1	53.1
$2\nu_2$	1610.9	245.5
	1730.8	108.9
O-H Stretch of Water	3180.0	159.8
	3262.6	93.3
	3346.0	137.4
	3436.9	63.3
	3473.9	201.1

Table 4.2 DSC analysis results for the dehydration reaction:  
 $\text{CaCO}_3 \cdot 6\text{H}_2\text{O} \rightarrow \text{CaCO}_3 \cdot \text{H}_2\text{O}$ .

Temperature Interval	Mass Before Heating [mg]	Mass After Heating [mg]	Initial Moles of Included Water [moles]	Final Moles of Included Water [moles]	Moles of Included Water Lost [moles]
25-130 °C	3.43	1.96	5.92	1.00	4.92

Table 4.3 Observed Raman vibrational frequencies ( $\text{cm}^{-1}$ ) for  $\text{CaCO}_3 \cdot \text{H}_2\text{O}$  at 25 °C.

Vibrational Mode Region	Frequency in Wavenumbers [ $\text{cm}^{-1}$ ]	Full Width at Half Height [ $\text{cm}^{-1}$ ]
External	absent	absent
$\nu_4$	696.8 727.3	26.5 33.6
$\nu_2$	not observed	not observed
$\nu_1$	1081.7	29.9
$\nu_3$	1412.0 1482.3 1544.1	92.4 60.1 79.9
$2\nu_2$	1649.6 1737.4	75.2 52.7
O-H Stretch of Water	3008.1 3217.4 3447.6	394.8 260.6 301.9

Table 4.4 DSC analysis results for the transformation reaction:  
 $\text{CaCO}_3 \cdot \text{H}_2\text{O} \rightarrow \text{vaterite}$ .

Temperature Interval	Mass Before Heating [mg]	Mass After Heating [mg]	Initial Moles of Included Water [moles]	Final Moles of Included Water [moles]	Moles of Included Water Lost [moles]
25-200 °C	1.96	1.69	1.00	0.0969	0.90

Table 4.5 Observed Raman vibrational frequencies ( $\text{cm}^{-1}$ ) for calcite at 25 °C and comparison with literature.

Vibrational Mode Region	Frequency in Wavenumbers [ $\text{cm}^{-1}$ ]	Full Width at Half Height [ $\text{cm}^{-1}$ ]	Literature (Behrens <i>et al.</i> , 1995) [ $\text{cm}^{-1}$ ]	Literature (Gillet <i>et al.</i> , 1993) [ $\text{cm}^{-1}$ ]	Literature (White, 1974) [ $\text{cm}^{-1}$ ]
External	156.6 184.1 (He-Ne plasma line) 283.0	7.5 2.1 10.3	155 282	156 281	156 283
$\nu_4$	713.9	5.6	711	711	714
$\nu_2$	inactive	inactive	inactive	inactive	inactive
$\nu_1$	1086.6	3.0	1085	1085	1088
$\nu_3$	1435.8	5.9	N/A	1434	1432
$2\nu_2$	1748.7	8.3	N/A	1748	N/A

Table 4.6 DSC analysis results for the polymorphic transformation reaction:  
vaterite → calcite.

Temperature Interval	Mass Before Heating [mg]	Mass After Heating [mg]	Initial Moles of Included Water [moles]	Final Moles of Included Water [moles]	Moles of Included Water Lost [moles]
25-120 °C	17.29	17.21	0.129	0.103	0.026 (physically absorbed)
120-300 °C	17.21	16.98	0.103	0.027	0.076 (chemically trapped)
300-550 °C	16.98	16.90	0.027	0.000	0.027 (chemically trapped)

Table 4.7 Observed Raman vibrational frequencies ( $\text{cm}^{-1}$ ) for aragonite at 25 °C and comparison with literature.

Vibrational Mode Region	Frequency in Wavenumbers [ $\text{cm}^{-1}$ ]	Full Width at Half Height [ $\text{cm}^{-1}$ ]	Literature (Gauldie <i>et al.</i> , 1997) [ $\text{cm}^{-1}$ ]	Literature (Behrens <i>et al.</i> , 1995) [ $\text{cm}^{-1}$ ]	Literature (White, 1974) [ $\text{cm}^{-1}$ ]
External	115.7	9.3	113	142	113
	131.9	10.4	142	152	146
	144.3	5.0	153	179	155
	154.3	8.1	180	189	183
	166.8	18.7	190	205	193
	182.1	7.4	206	213	208
	192.4	9.9	242	273	217
	207.8	6.5	261	282	222
	216.2	11.8	284		250
262.5	65.6			263	
					276
					287
$\nu_4$	702.0	1.9	701	701	703
	706.5	2.9	705	705	
	717.8	2.4			
$\nu_2$	N/A	N/A	N/A	N/A	N/A
$\nu_1$	1085.7	2.6	1085	1085	1087
$\nu_3$	1462.5	6.2	1462	N/A	1464
	1574.7	9.0	1574		1466
$2\nu_2$	1709.2	9.2	N/A	N/A	N/A
	1736.8	56.4			
	1793.5	40.4			
	1814.4	9.5			

Table 4.8 Observed Raman vibrational frequencies ( $\text{cm}^{-1}$ ) for vaterite at 25 °C and comparison with literature.

Vibrational Mode Region	Frequency in Wavenumbers [ $\text{cm}^{-1}$ ]	Full Width at Half Height [ $\text{cm}^{-1}$ ]	Literature (Gauldie <i>et al.</i> , 1997) [ $\text{cm}^{-1}$ ]	Literature (Behrens <i>et al.</i> , 1995) [ $\text{cm}^{-1}$ ]	Literature (White, 1974) [ $\text{cm}^{-1}$ ]
External	116.6	10.0	106	105	N/A
	130.3	19.1	116	114	
	151.5	16.2	150	177	
	172.9	21.1	178	209	
	190.0	10.5	210	267	
	208.4	48.0	266	300	
	266.4	35.4	302		
	301.7	22.2	330		
332.5	31.3				
$\nu_4$	667.2	8.4	685	740	752
	674.0	9.7	740	750	
	684.8	6.4	743		
	738.4	7.9	751		
	743.5	7.3			
751.3	8.7				
$\nu_2$	881.0	8.5	N/A	N/A	845
	877.6	2.5			
	873.7	5.5			
$\nu_1$	1075.0	7.0	1075	1074	1066 1090
	1081.4	9.7	1081	1090	
	1090.9	6.6	1090		
$\nu_3$	1421.1	21.1	N/A	N/A	1416 1466
	1440.9	16.7			
	1459.9	26.8			
	1480.4	31.4			
	1542.3	35.1			
1555.0	5.6				
$2\nu_2$	1745.6	7.3	N/A	N/A	N/A
	1754.4	12.7			
	1757.5	11.3			

Table 4.9 Observed infrared vibrational frequencies ( $\text{cm}^{-1}$ ) for vaterite at 25 °C and comparison with literature.

Vibrational Mode Region	Frequency in Wavenumbers [ $\text{cm}^{-1}$ ]	Full Width at Half Height [ $\text{cm}^{-1}$ ]	Literature (Jones and Jackson, 1993) [ $\text{cm}^{-1}$ ]	Literature (White, 1974) [ $\text{cm}^{-1}$ ]
$\nu_4$	660.2	7.7	668 745	750
	666.5	2.5		
	673.8	7.7		
	680.8	3.6		
	739.0	5.7		
	744.1	5.2		
$\nu_2$	749.5	7.0	877	870
	871.2	11.8		
	876.9	12.9		
$\nu_1$	883.7	3.1	1089	1070 1085
	1075.3	10.2		
	1081.1	5.7		
$\nu_3$	1088.4	7.1	1408 1432 1489	1420 1490
	1402.1	55.1		
	1415.0	22.0		
	1442.1	35.2		
	1466.8	13.8		
	1492.0	61.8		
$[\nu_4 + \nu_1]$	1558.1	12.5	1743 1765 1836	N/A
	1738.7	6.6		
	1747.3	10.7		
	1765.5	14.6		
	1814.2	8.0		
	1821.8	6.8		
	1836.1	17.1		



**Figure 4.1** Photomicrograph (10x magnification) of  $\text{CaCO}_3 \cdot 6\text{H}_2\text{O}$  collected immediately after the precipitation showing the hexagonal shape of the crystals.

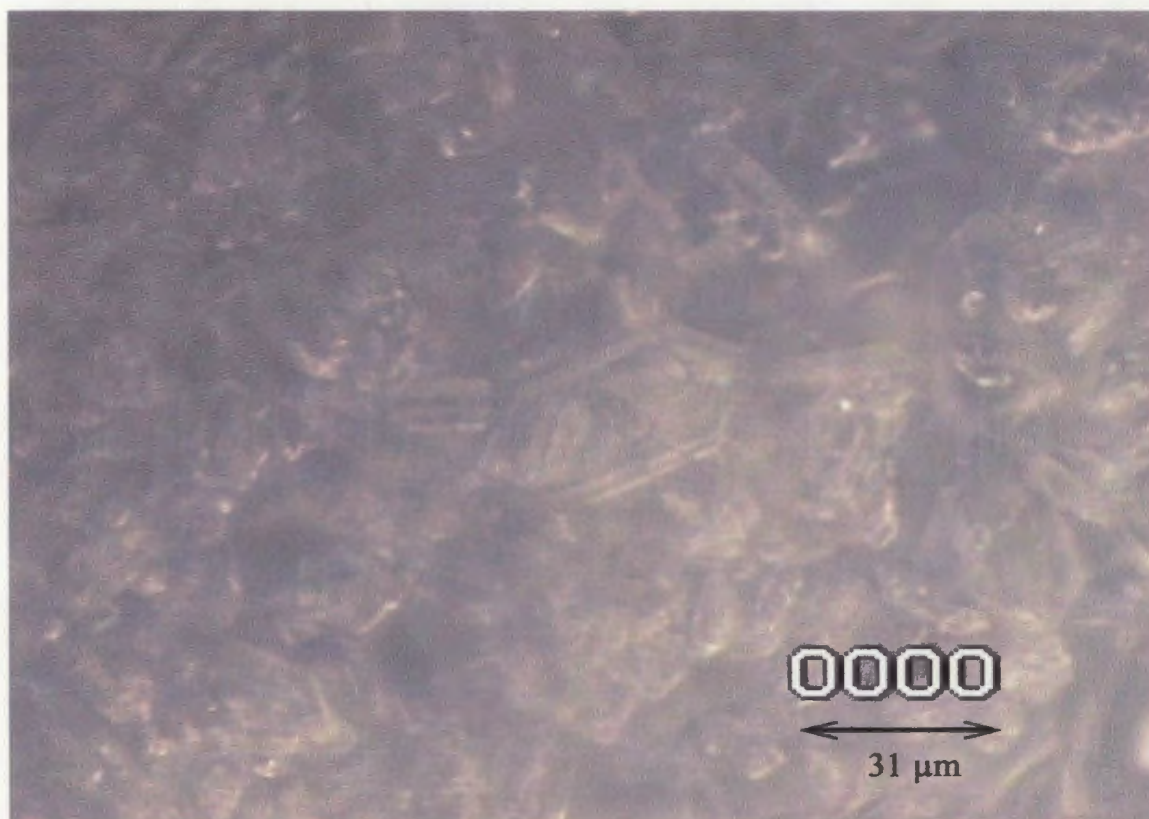


Figure 4.2 Photomicrograph (50x magnification) of  $\text{CaCO}_3 \cdot 6\text{H}_2\text{O}$  collected immediately after the precipitation showing the hexagonal shape of the crystals.

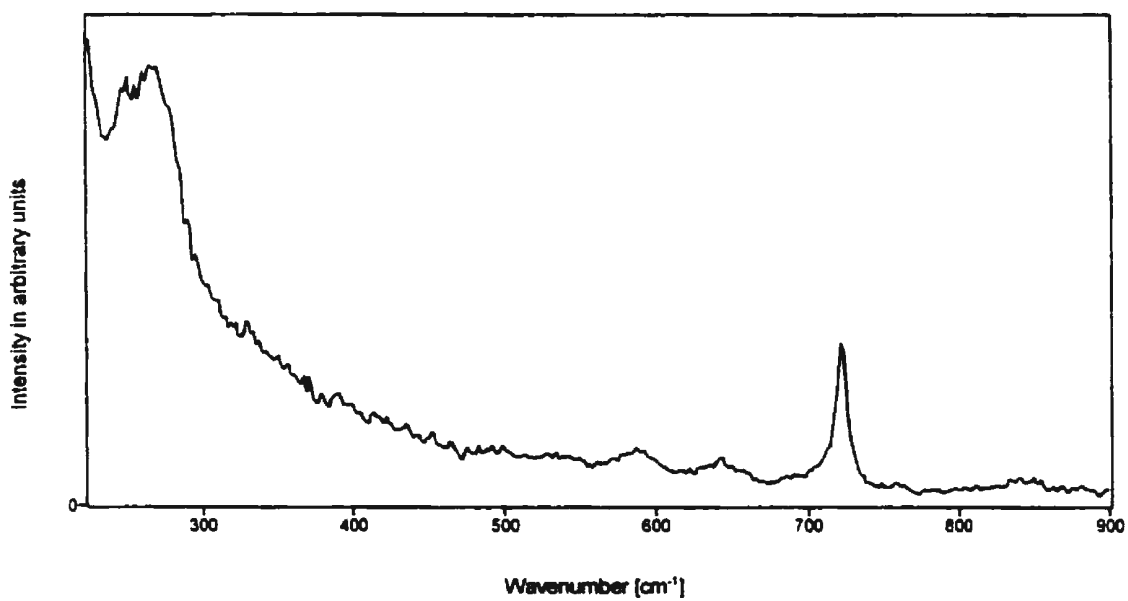


Figure 4.3 Raman spectrum of the external lattice mode region and  $\nu_1$  internal vibrational mode region of  $\text{CaCO}_3 \cdot 6\text{H}_2\text{O}$  at 25 °C.

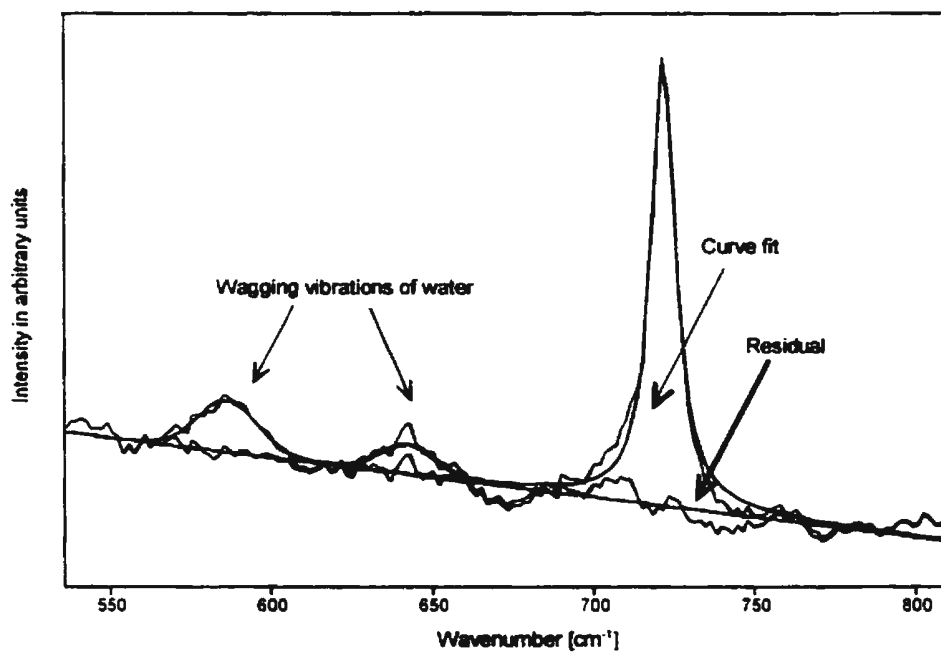


Figure 4.3a Curve fit of the Raman spectrum of the wagging vibrations of water and the  $\nu_4$  internal vibrational mode region of  $\text{CaCO}_3 \cdot 6\text{H}_2\text{O}$  at 25 °C.

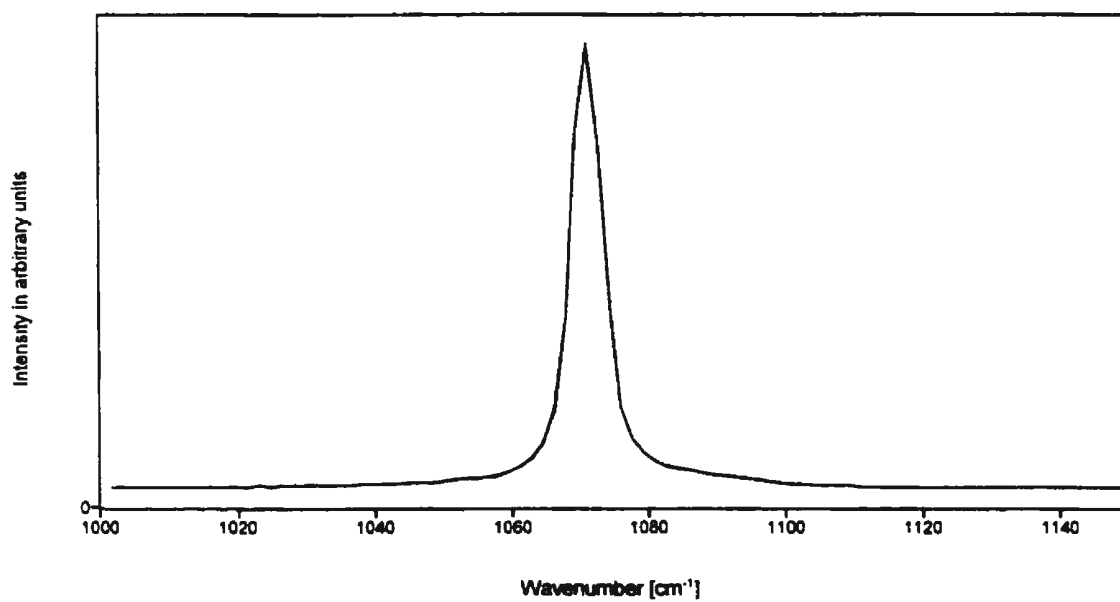


Figure 4.4 Raman spectrum of the  $\nu_1$  internal vibrational mode region of  $\text{CaCO}_3 \cdot 6\text{H}_2\text{O}$  at 25 °C.

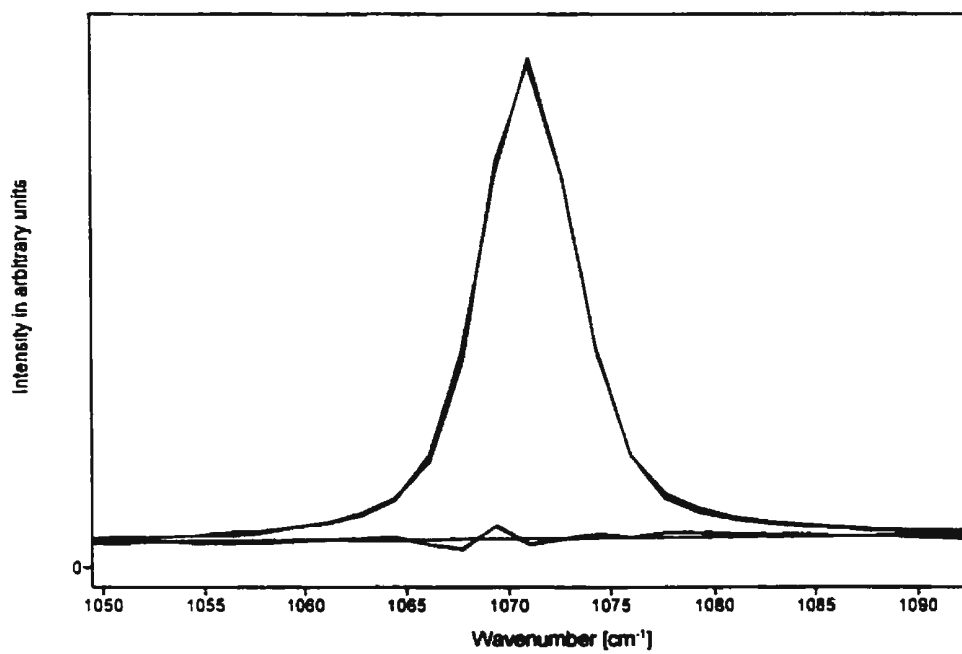


Figure 4.4a Curve fit of the Raman spectrum of the  $\nu_1$  internal vibrational mode region of  $\text{CaCO}_3 \cdot 6\text{H}_2\text{O}$  at  $25^\circ\text{C}$ .

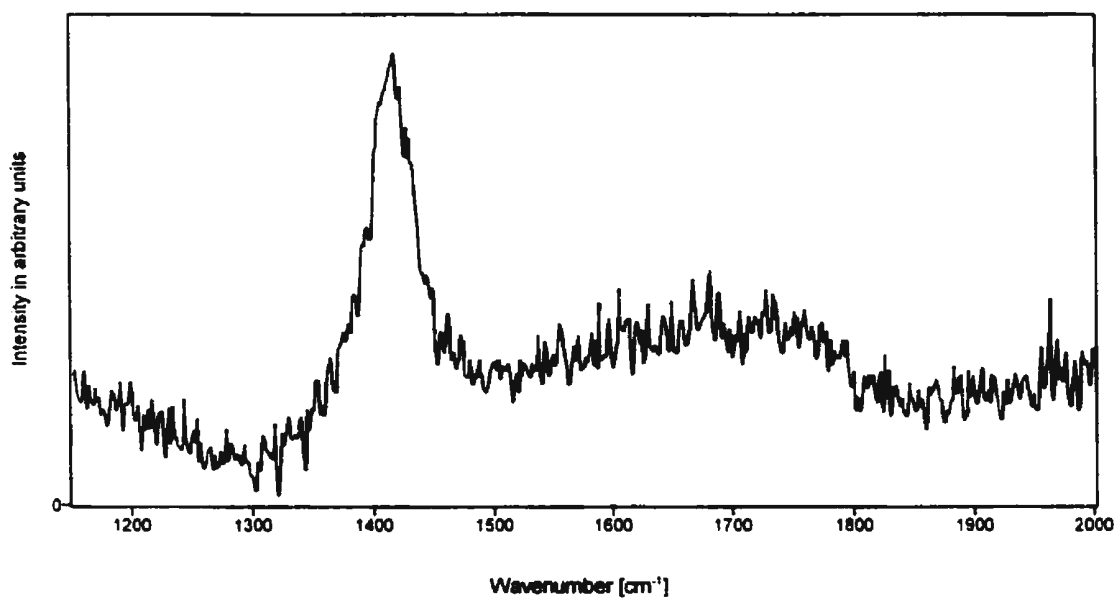


Figure 4.5 Raman spectrum of the  $\nu_3$  internal vibrational mode region and  $2\nu_2$  overtone region of  $\text{CaCO}_3 \cdot 6\text{H}_2\text{O}$ , as well as the  $\nu_2$  region of water, at 25 °C.

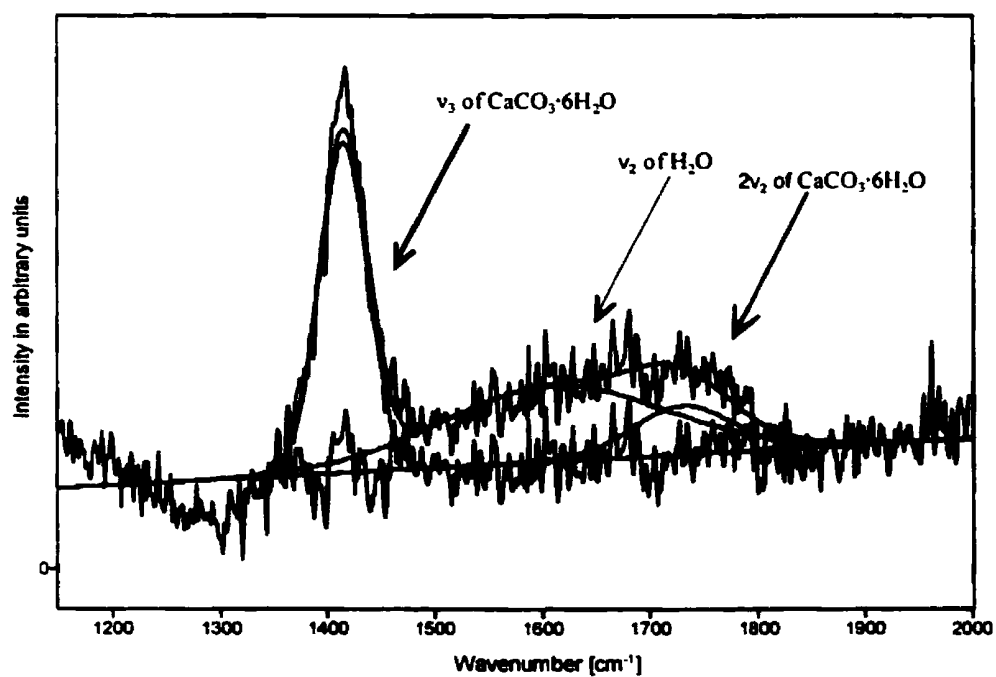


Figure 4.5a Curve fit of the Raman spectrum of the  $\nu_3$  internal vibrational mode region and  $2\nu_2$  overtone region of  $\text{CaCO}_3 \cdot 6\text{H}_2\text{O}$ , as well as the  $\nu_2$  region of water, at 25 °C.

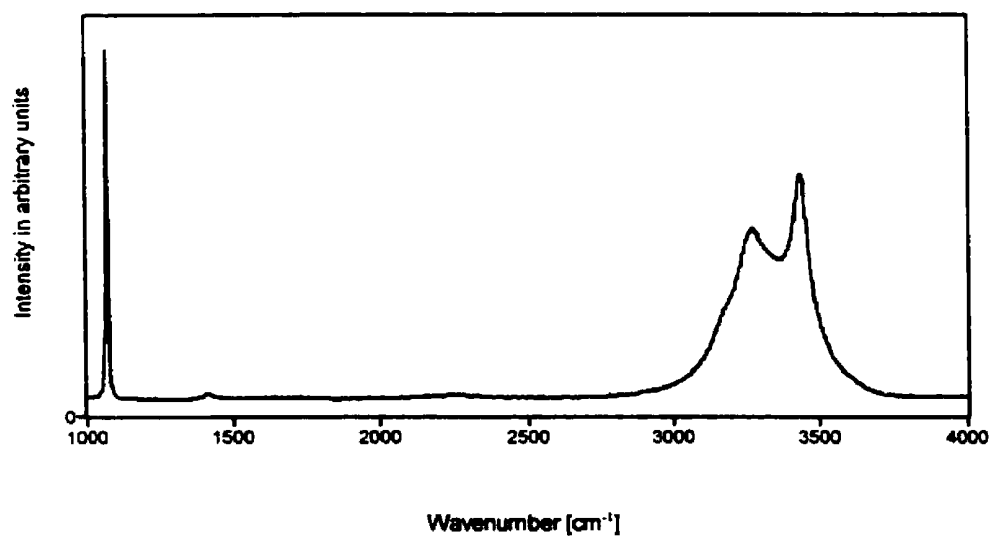


Figure 4.6 Overview Raman spectrum of  $\text{CaCO}_3 \cdot 6\text{H}_2\text{O}$  at  $25^\circ\text{C}$  displaying the region from  $1000\text{-}4000\text{ cm}^{-1}$ .

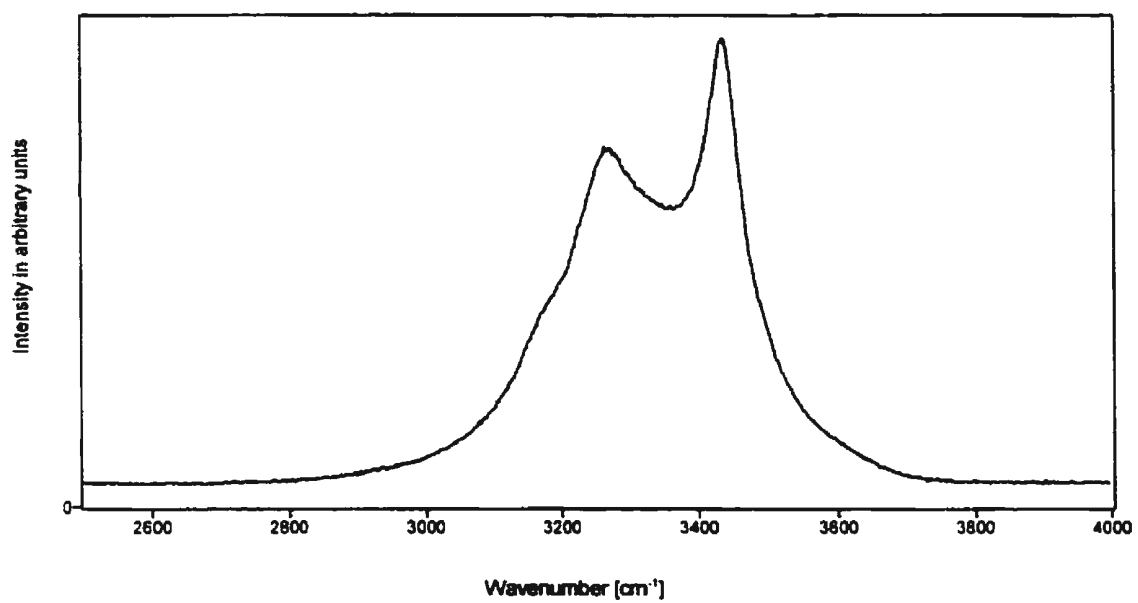


Figure 4.6a Raman spectrum of the O-H stretching region of  $\text{CaCO}_3 \cdot 6\text{H}_2\text{O}$  at 25 °C.

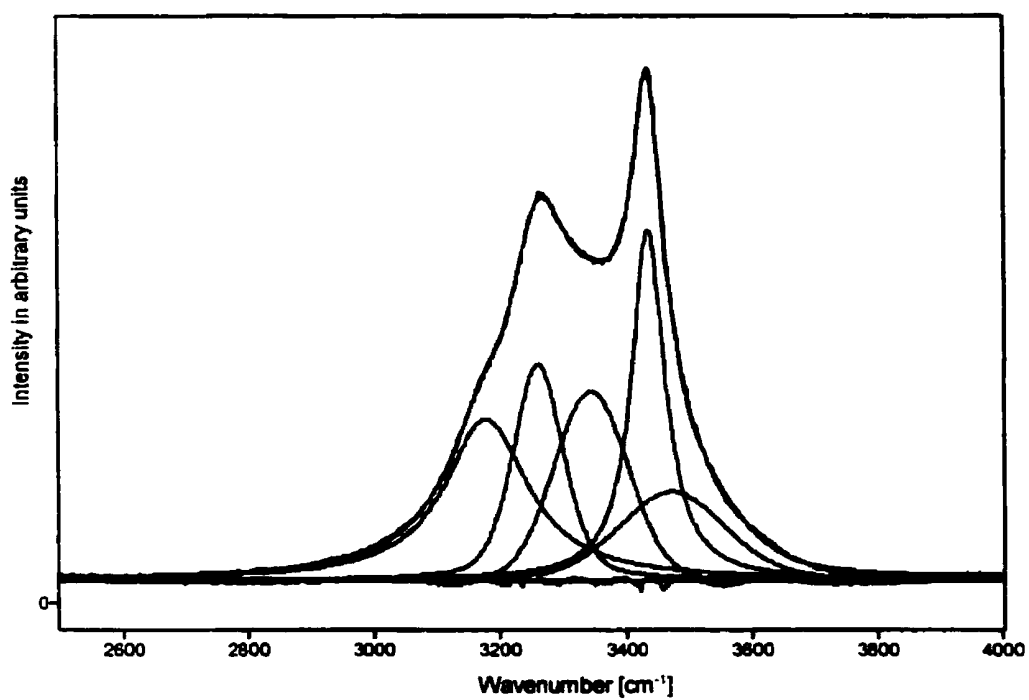


Figure 4.6b Curve fit of the Raman spectrum of the O-H stretching region of  $\text{CaCO}_3 \cdot 6\text{H}_2\text{O}$  at 25 °C.

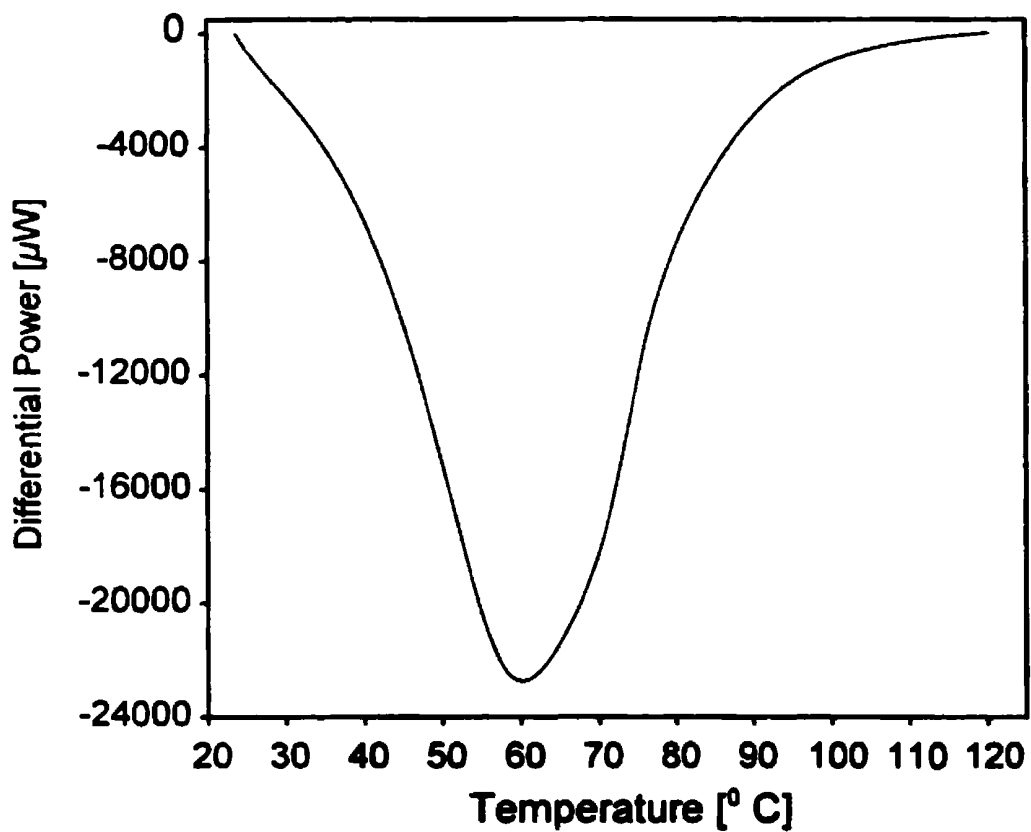


Figure 4.7 DSC spectrum for the dehydration reaction,  $\text{CaCO}_3 \cdot 6\text{H}_2\text{O} \rightarrow \text{CaCO}_3 \cdot 1\text{H}_2\text{O}$ , from 25-120 °C at a rate of 10 °C/minute.

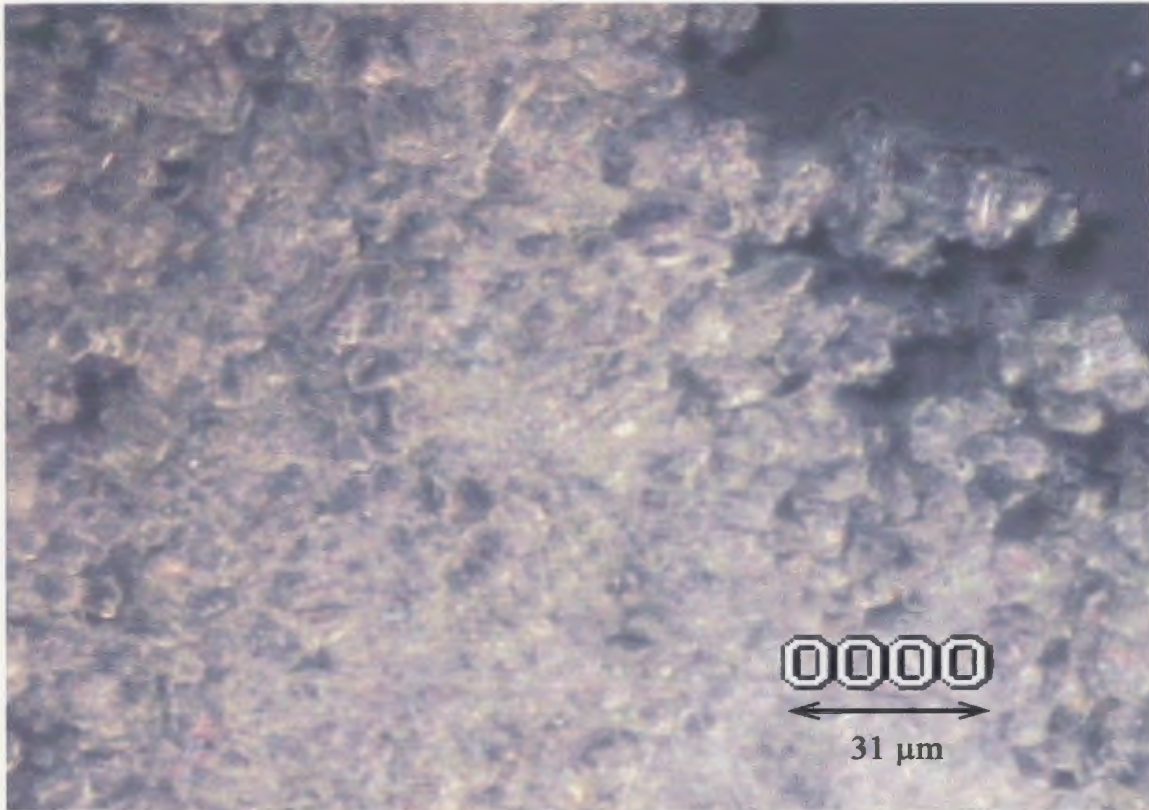


Figure 4.8 Photomicrograph (20x magnification) of  $\text{CaCO}_3 \cdot 1\text{H}_2\text{O}$  produced by dehydration of  $\text{CaCO}_3 \cdot 6\text{H}_2\text{O}$  showing the cloudy appearance and distorted, hexagonal shape of the crystals.

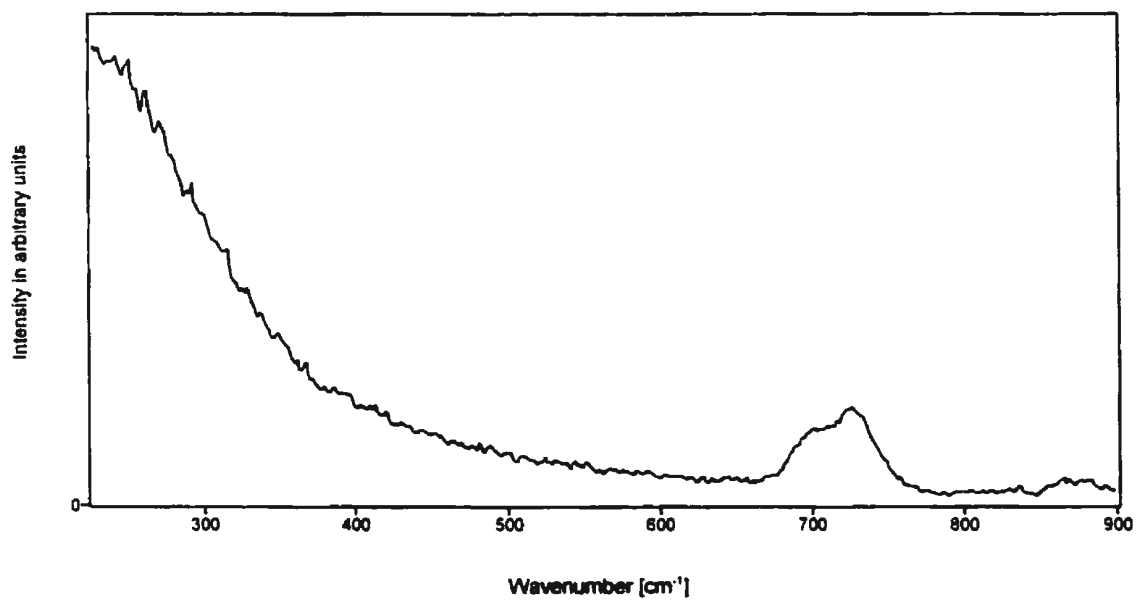


Figure 4.9 Raman spectrum of the external lattice mode region and  $\nu_4$  internal vibrational mode region of  $\text{CaCO}_3 \cdot 1\text{H}_2\text{O}$  at 25 °C.

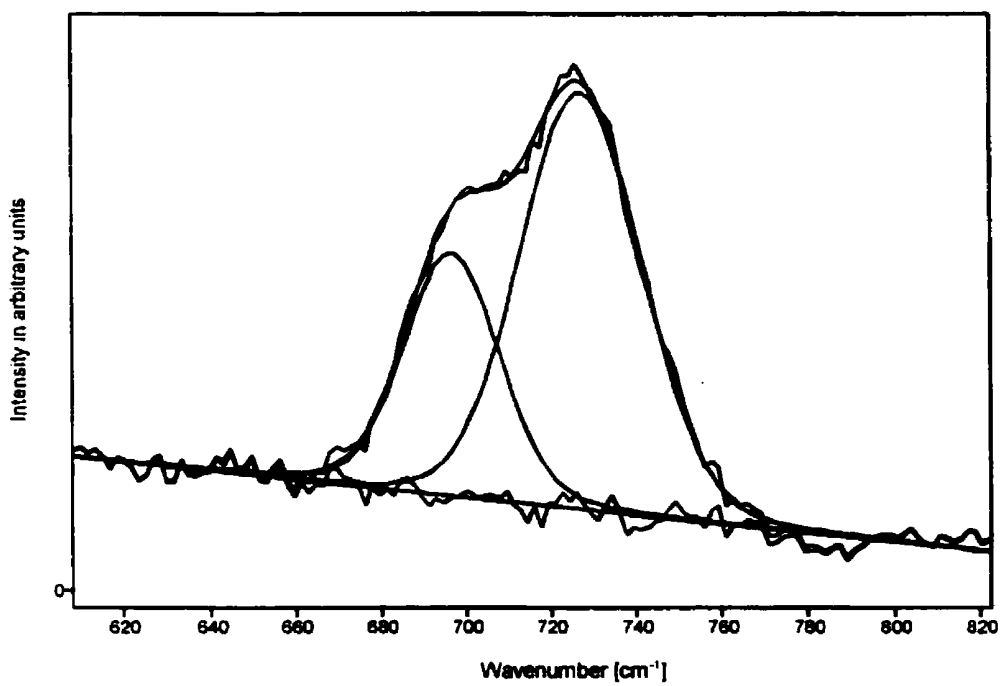


Figure 4.9a Curve fit of the Raman spectrum of the  $\nu_4$  internal vibrational mode region of  $\text{CaCO}_3 \cdot 1\text{H}_2\text{O}$  at  $25^\circ\text{C}$ .

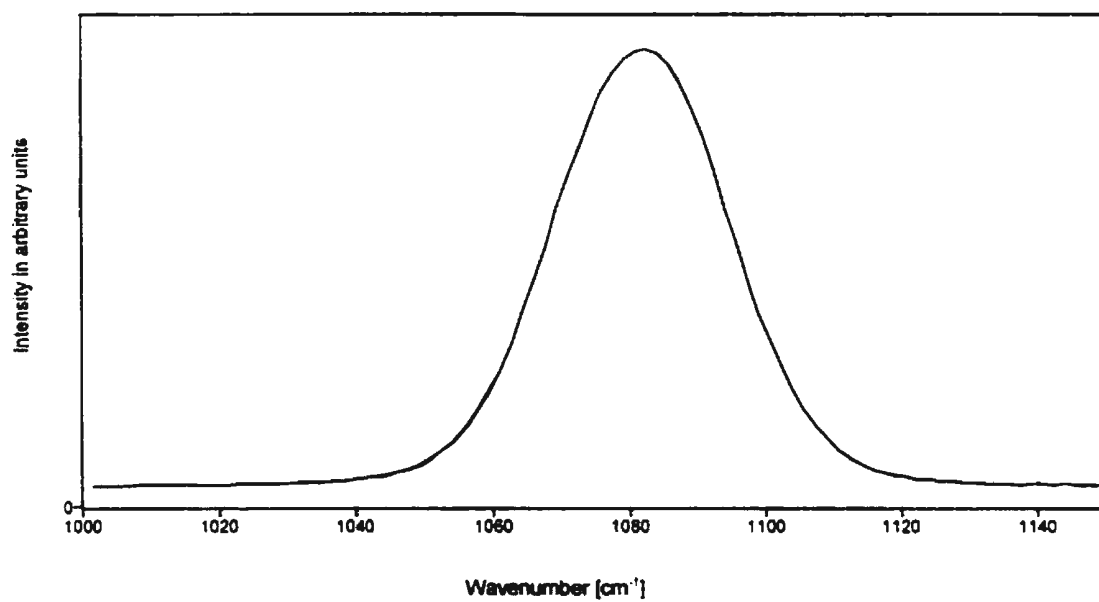


Figure 4.10 Raman spectrum of the  $\nu_1$  internal vibrational mode region of  $\text{CaCO}_3 \cdot \text{H}_2\text{O}$  at 25 °C.

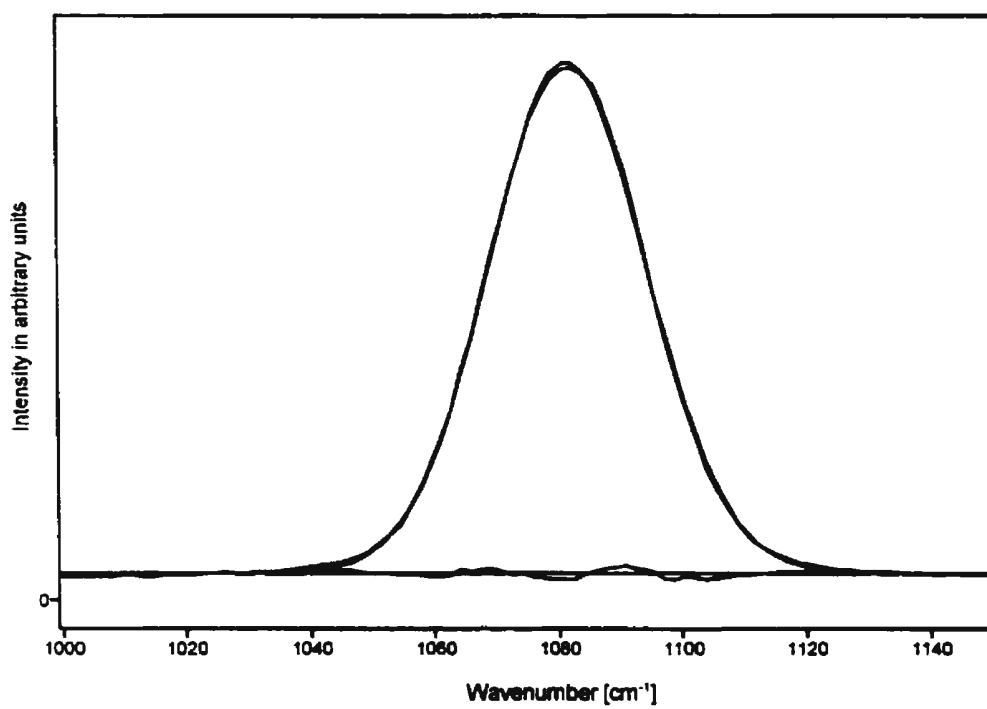


Figure 4.10a Curve fit of the Raman spectrum of the  $\nu_1$  internal vibrational mode region of  $\text{CaCO}_3 \cdot \text{H}_2\text{O}$  at 25 °C.

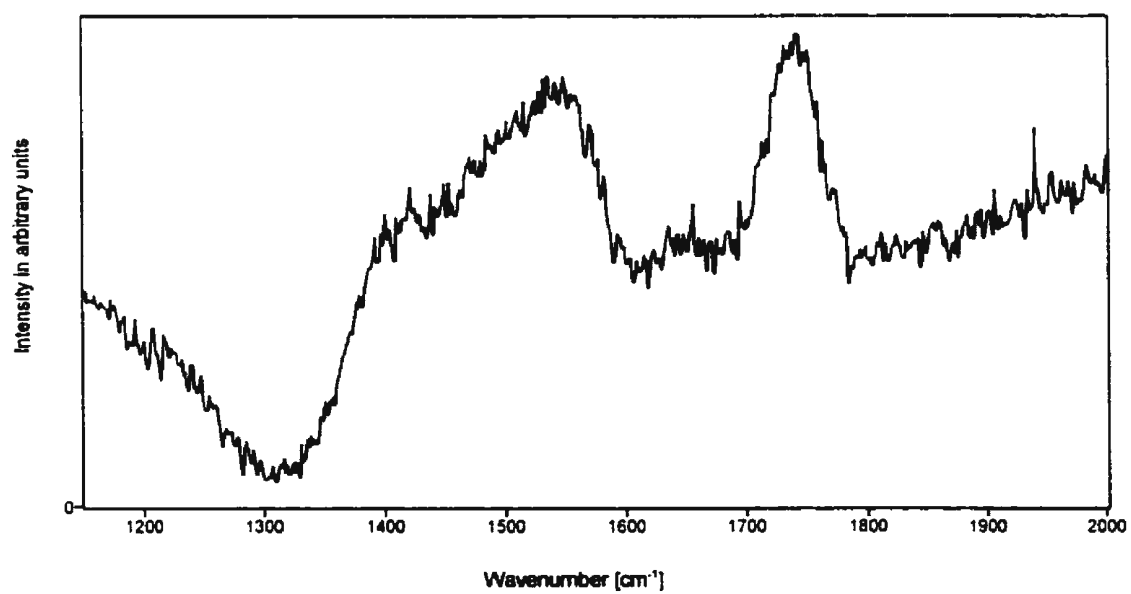


Figure 4.11 Raman spectrum of the  $\nu_3$  internal vibrational mode region and  $2\nu_2$  overtone region of  $\text{CaCO}_3 \cdot \text{H}_2\text{O}$ , as well as the  $\nu_2$  region of water, at 25 °C.

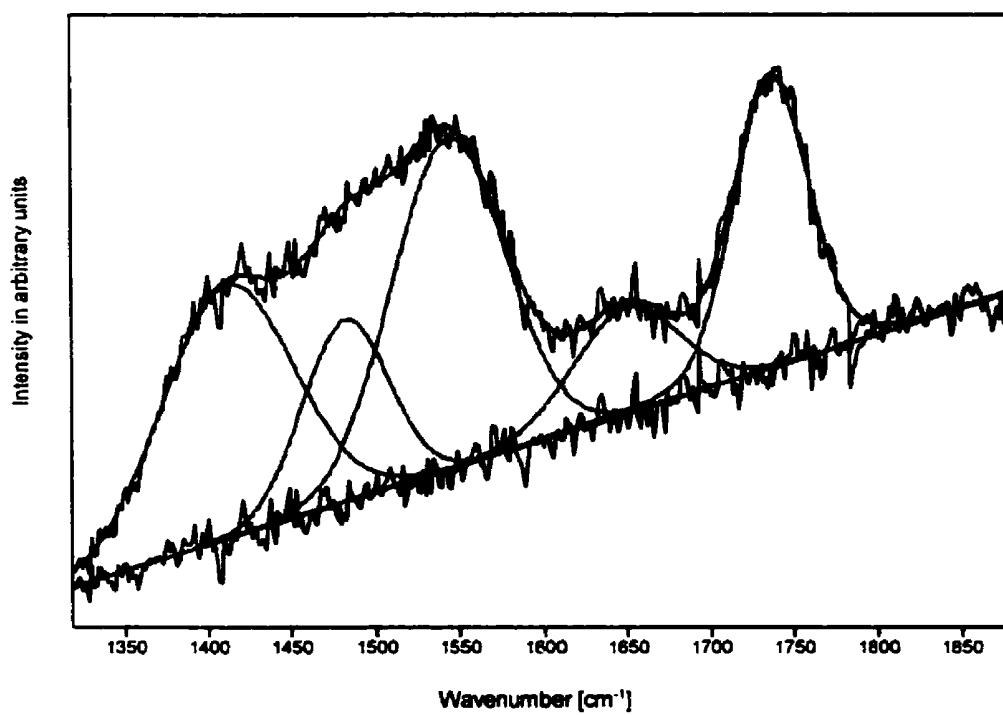


Figure 4.11a Curve fit of the Raman spectrum of the  $\nu_3$  internal vibrational mode region and  $2\nu_2$  overtone region of  $\text{CaCO}_3 \cdot \text{H}_2\text{O}$ , as well as the  $\nu_2$  region of water, at 25 °C.

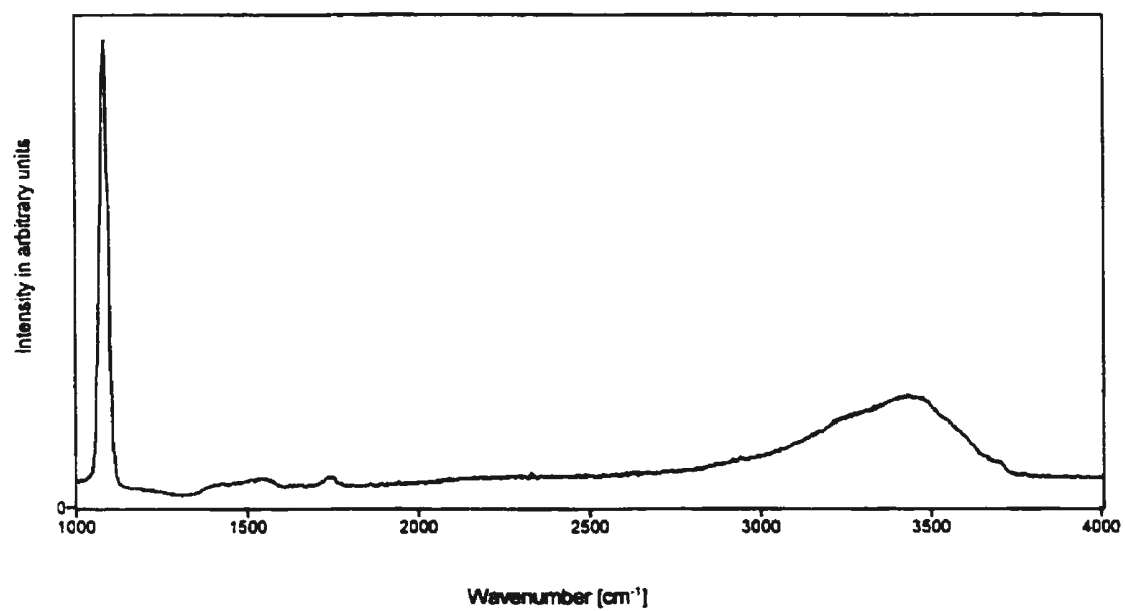


Figure 4.12 Overview Raman spectrum of CaCO<sub>3</sub>·1H<sub>2</sub>O at 25 °C displaying the region from 1000-4000 cm<sup>-1</sup>.

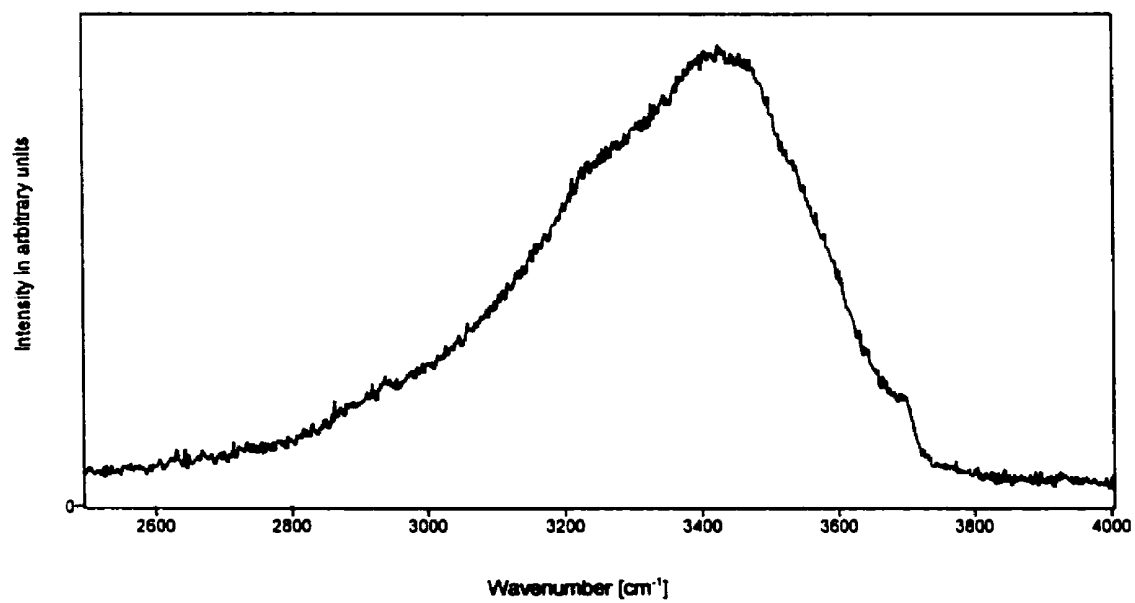


Figure 4.12a Raman spectrum of the O-H stretching region of  $\text{CaCO}_3 \cdot \text{H}_2\text{O}$  at 25 °C.

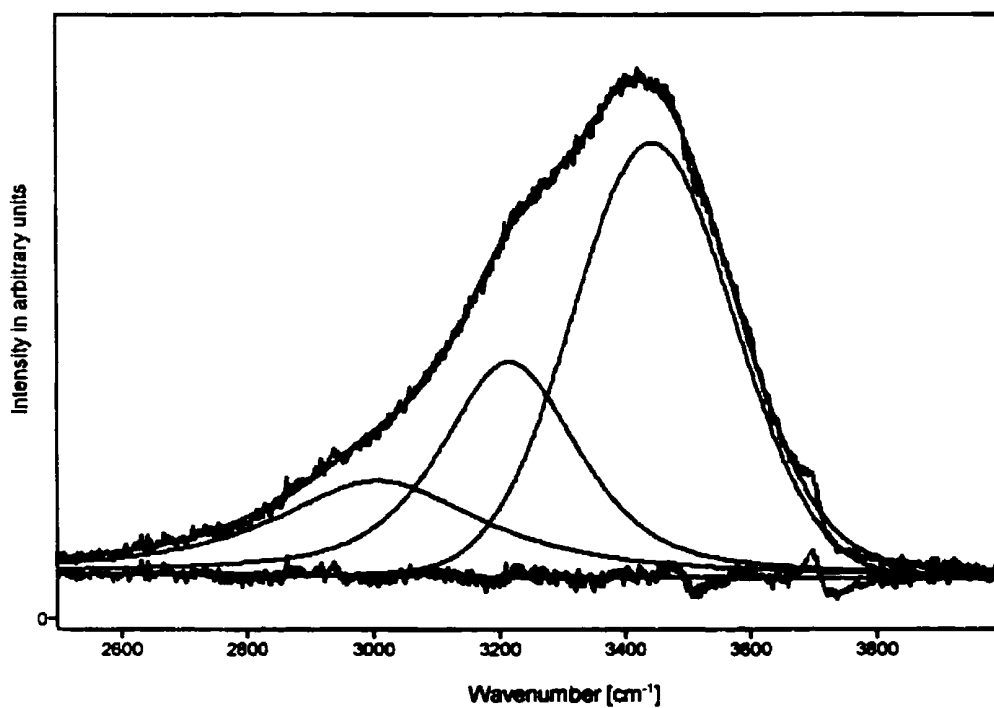
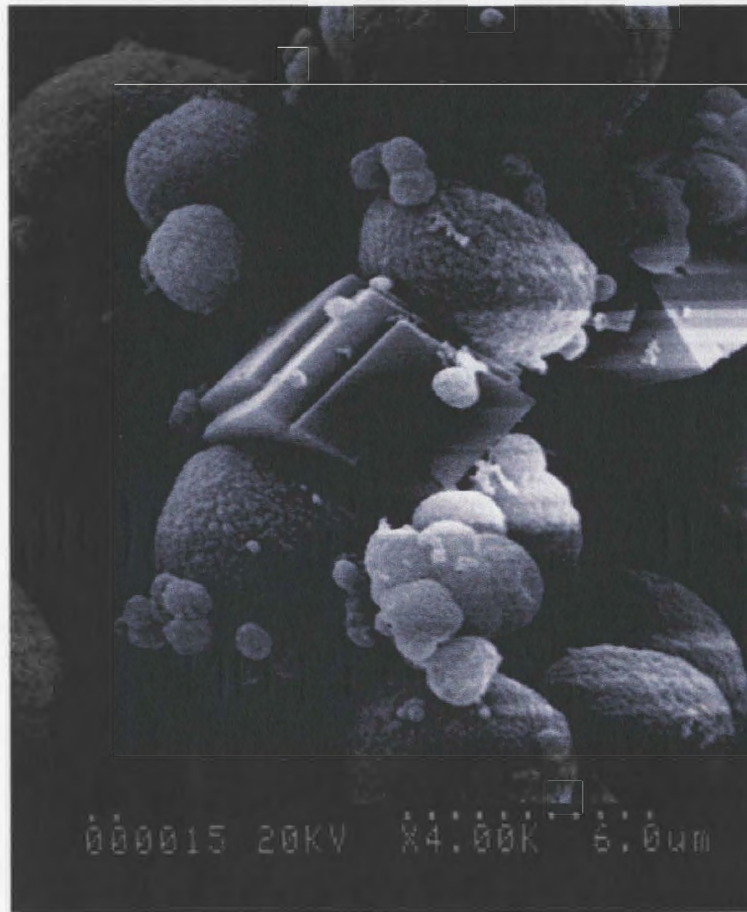


Figure 4.12b Curve fit of the Raman spectrum of the O-H stretching region of  $\text{CaCO}_3 \cdot 1\text{H}_2\text{O}$  at 25 °C.



**Figure 4.13** SEM micrograph of CaCO<sub>3</sub> collected 24 hours after the precipitation, showing calcite rhombs associated with spherulites of vaterite.



Figure 4.14 SEM micrograph of calcite prepared by the transformation reactions,  $\text{CaCO}_3 \cdot 6\text{H}_2\text{O} \rightarrow \text{CaCO}_3 \cdot \text{H}_2\text{O} \rightarrow \text{calcite}$ , showing the well-defined, hexagonal shape of the crystals.

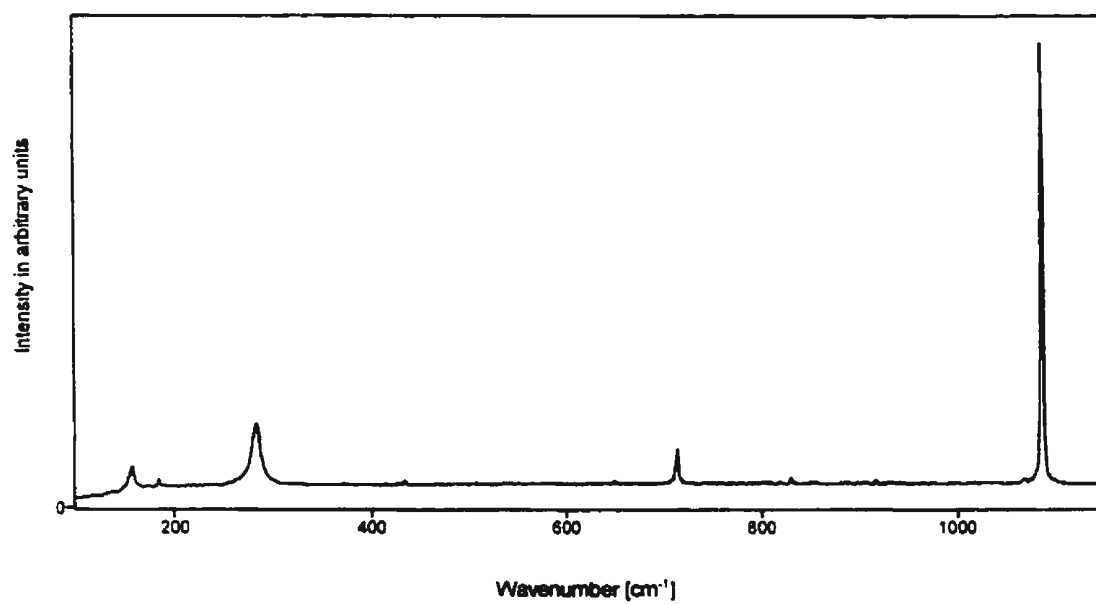


Figure 4.15 Overview Raman spectrum of natural calcite at 25 °C displaying the region from 100-1150  $\text{cm}^{-1}$ .

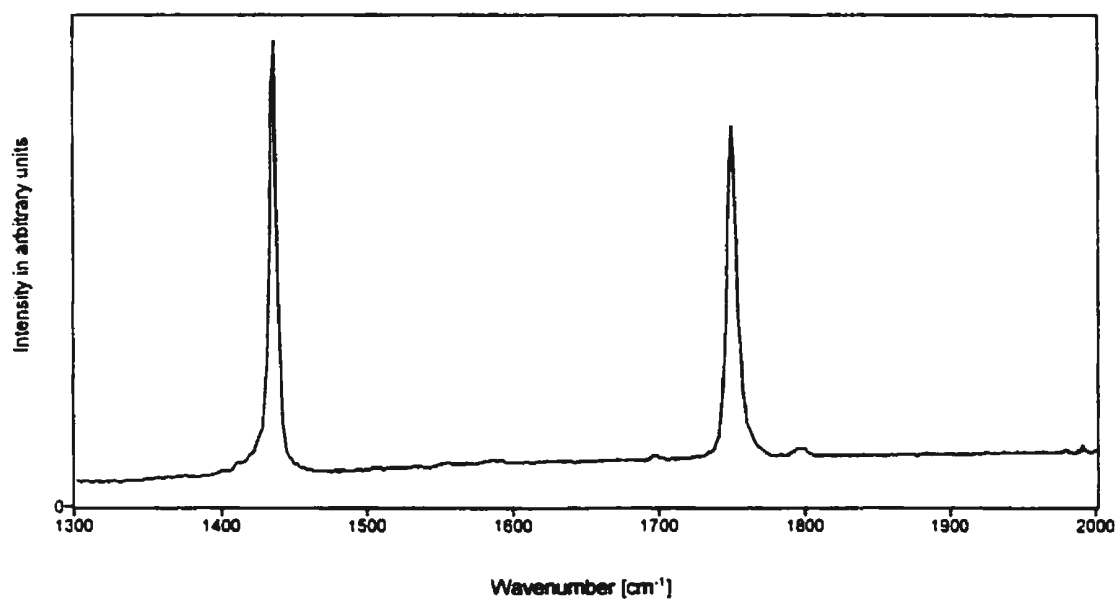


Figure 4.16 Raman spectrum of the  $\nu_3$  internal vibrational mode region and  $2\nu_2$  overtone region of natural calcite at 25 °C.

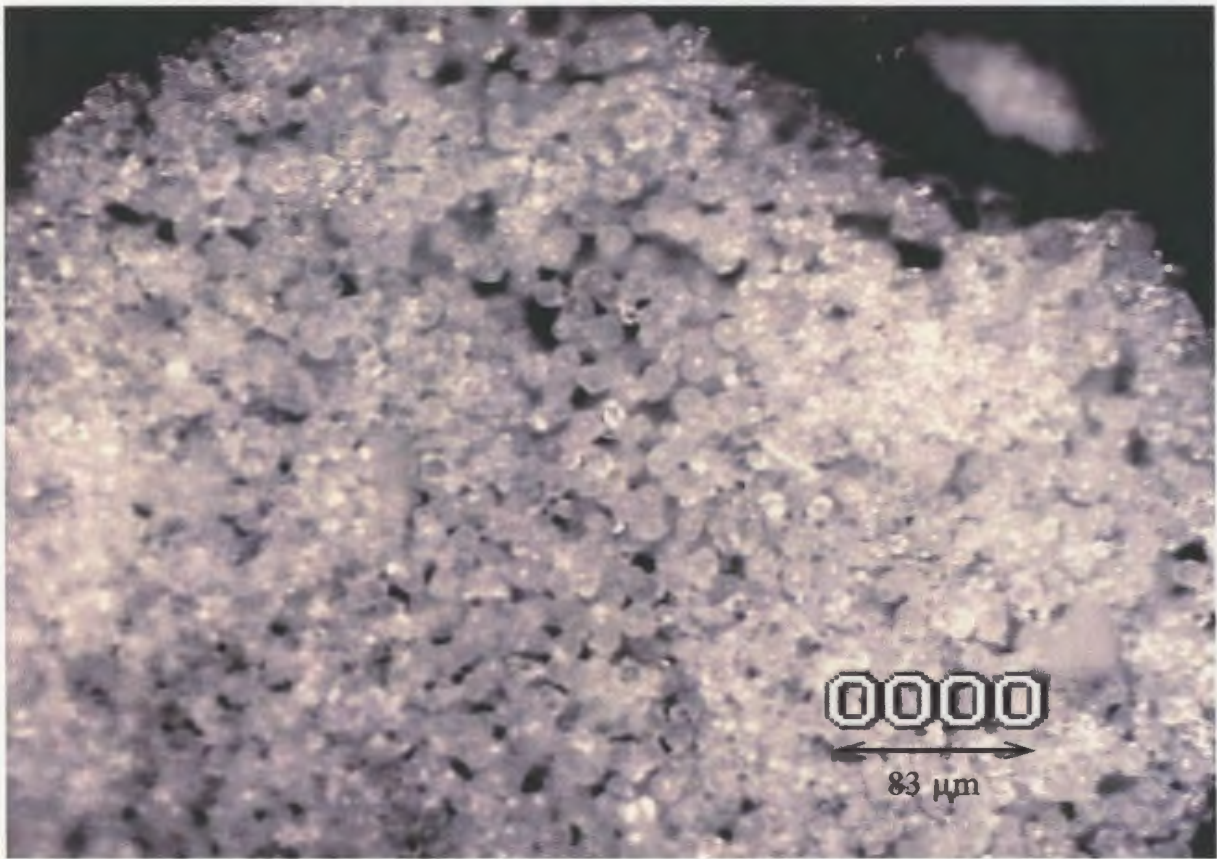


Figure 4.17 Photomicrograph (20x magnification) of vaterite removed immediately after the precipitation showing the spherical shape of the aggregated crystals.

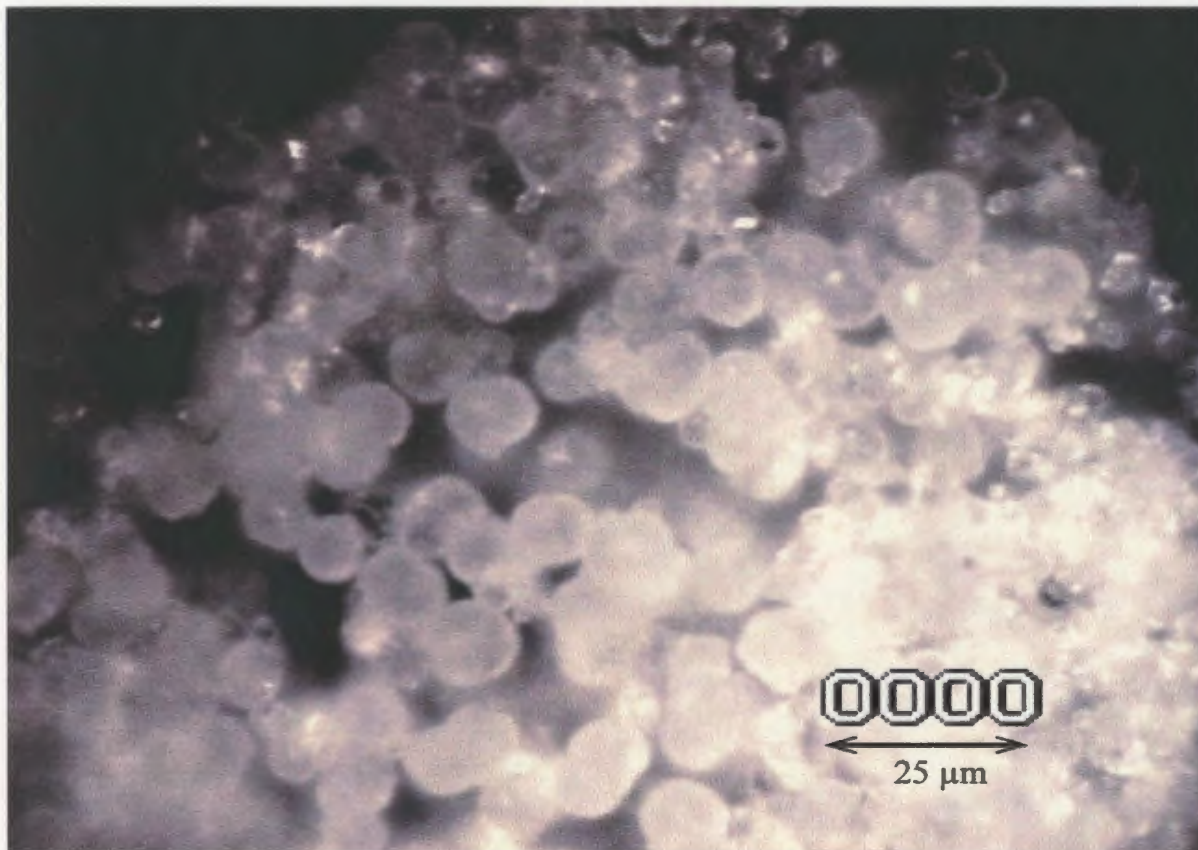
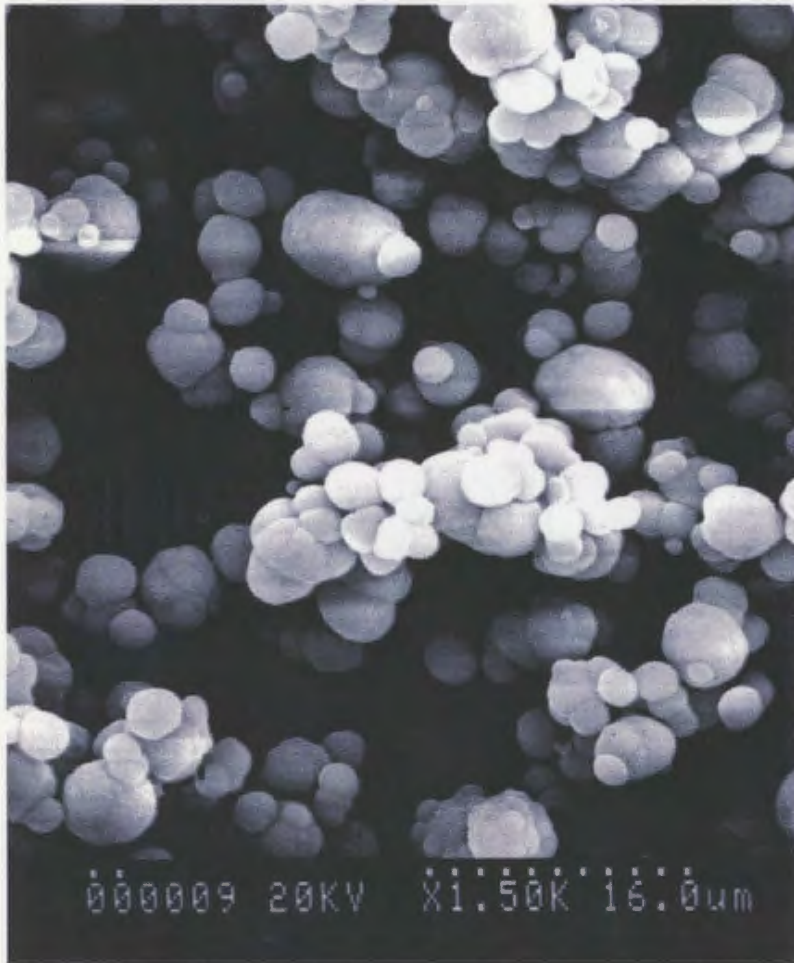
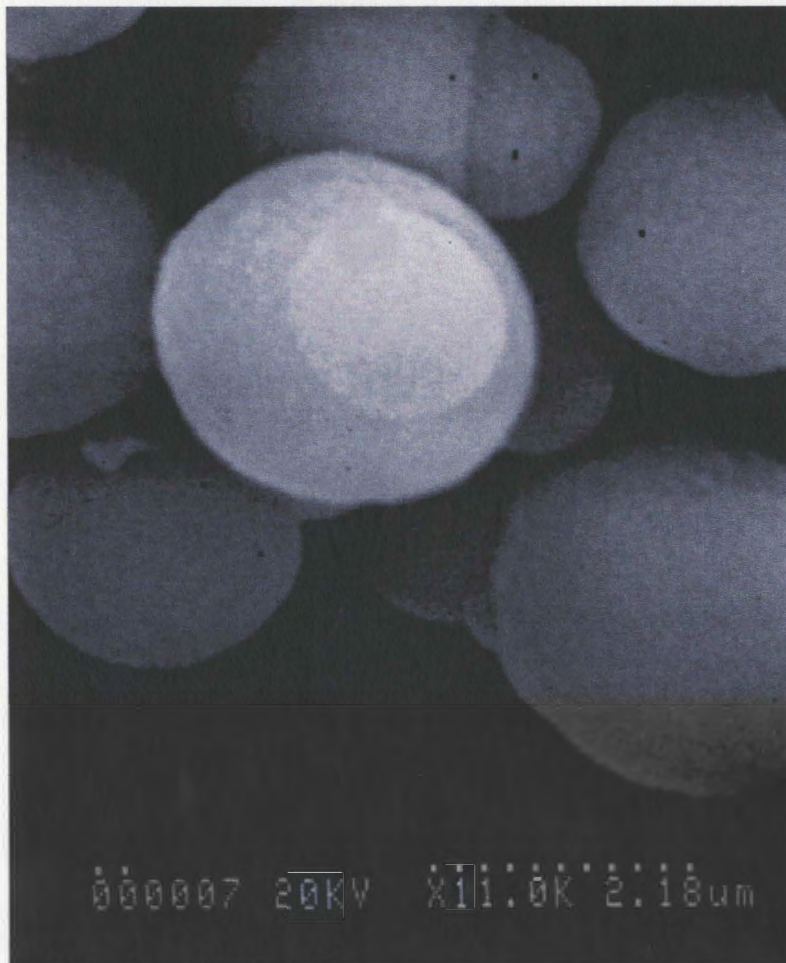


Figure 4.18 Photomicrograph (50x magnification) of vaterite removed immediately after the precipitation showing the spherical shape of the aggregated crystals.



**Figure 4.19** SEM micrograph (low magnification) of vaterite removed immediately after the precipitation showing the spherical shape of the aggregated crystals.



**Figure 4.20** SEM micrograph (high magnification) of vaterite removed immediately after the precipitation showing the spherical shape of the aggregated crystals.

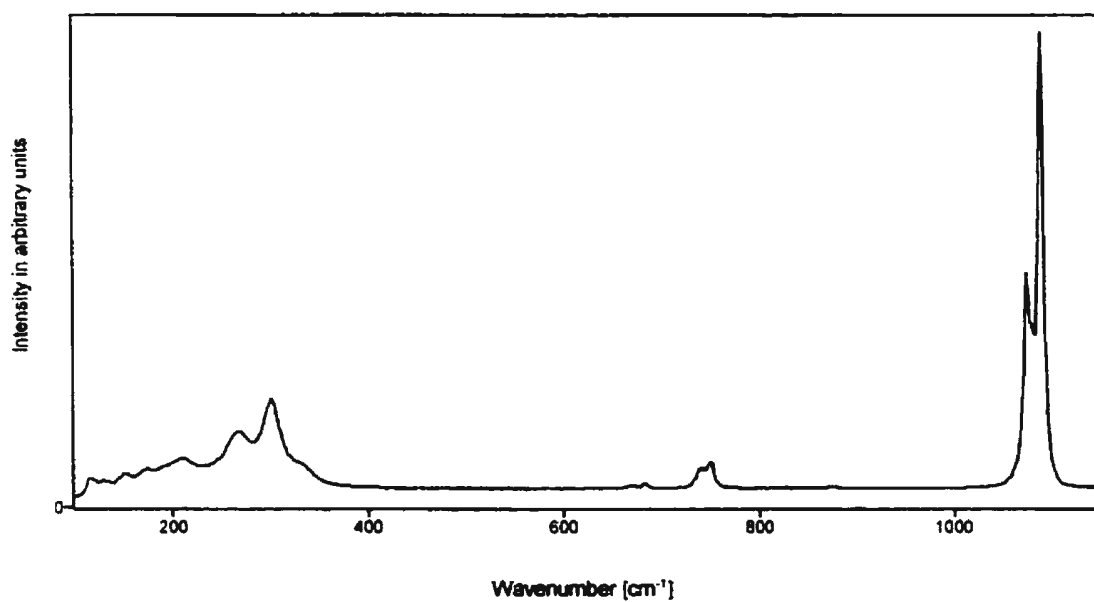


Figure 4.21 Overview Raman spectrum of vaterite at 25 °C displaying the region from 100-1150 cm<sup>-1</sup>.

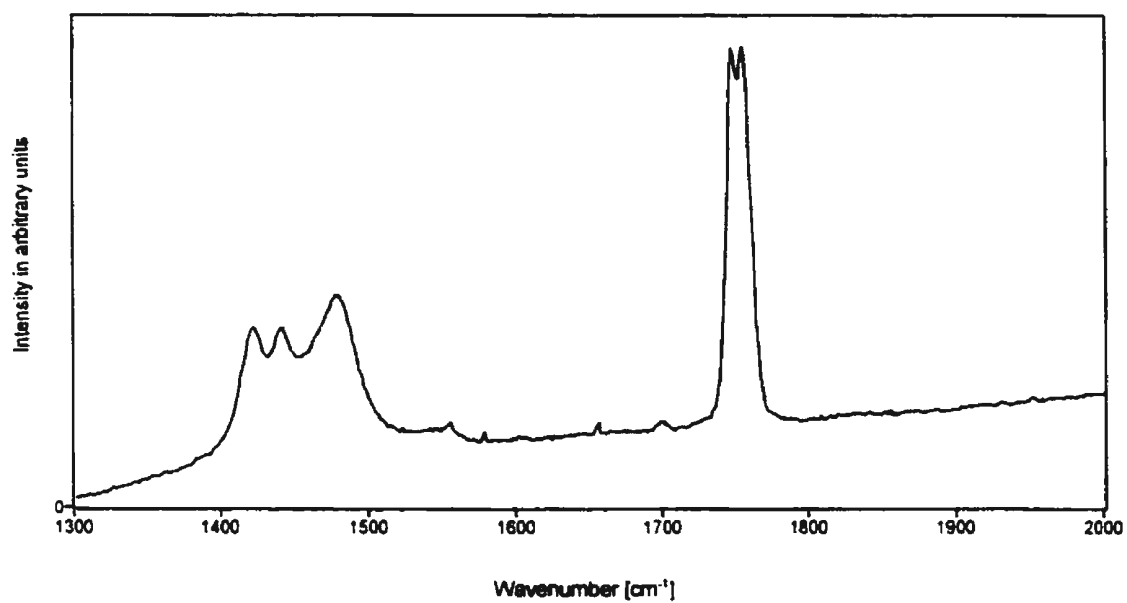


Figure 4.22 Raman spectrum of the  $\nu_3$  internal vibrational mode region and  $2\nu_2$  overtone region of vaterite at 25 °C.

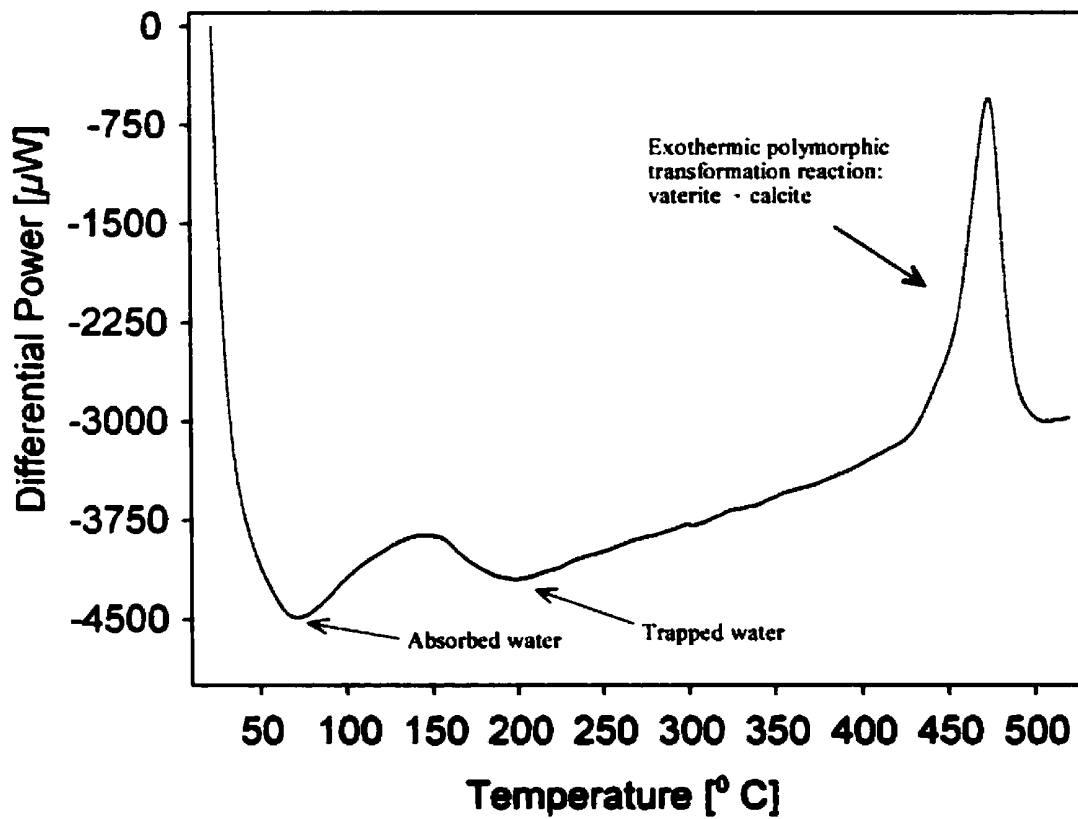


Figure 4.23 DSC analysis spectrum for the polymorphic transformation reaction, vaterite  $\rightarrow$  calcite, from 25-550  $^{\circ}\text{C}$  at a rate of 10  $^{\circ}\text{C}/\text{minute}$ .

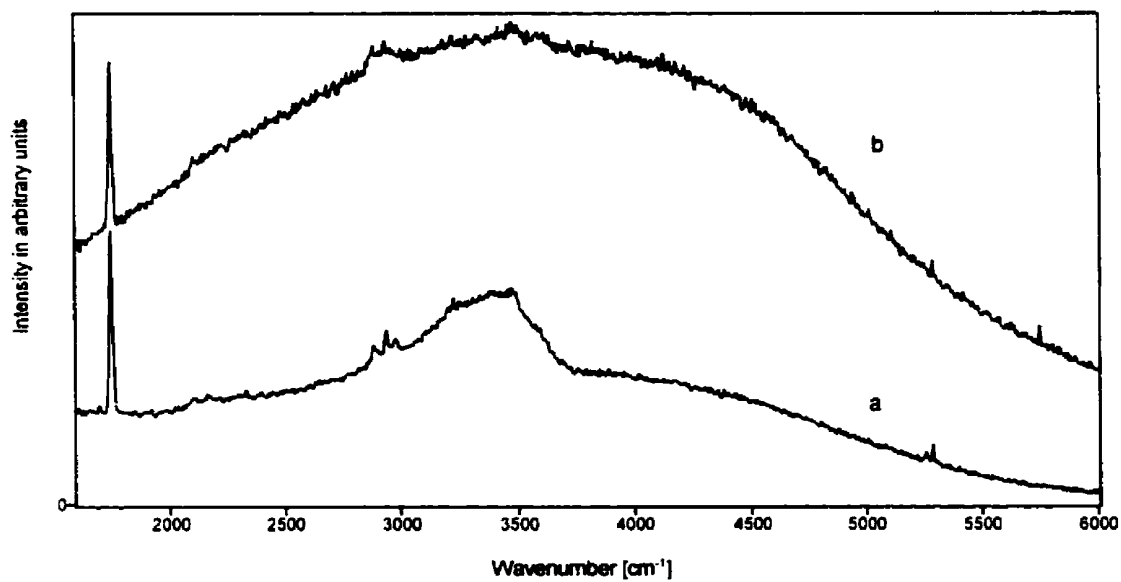


Figure 4.24 Overview Raman spectra of vaterite performed before [a] (note the presence of the water band at  $\approx 3400\text{ cm}^{-1}$ ) and after [b] heating to  $220\text{ }^{\circ}\text{C}$ , showing the removal of water and the increase in fluorescence due to manganese(II) impurities.

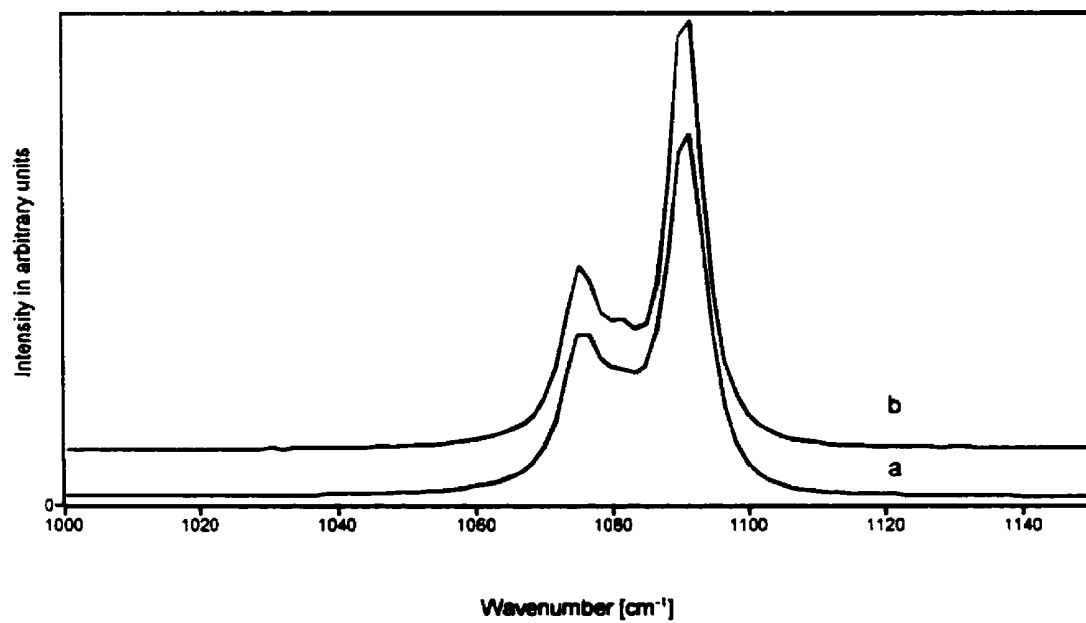


Figure 4.24a Raman spectra of the  $\nu_1$  internal vibrational mode region of vaterite performed before [a] and after [b] heating to 220 °C.

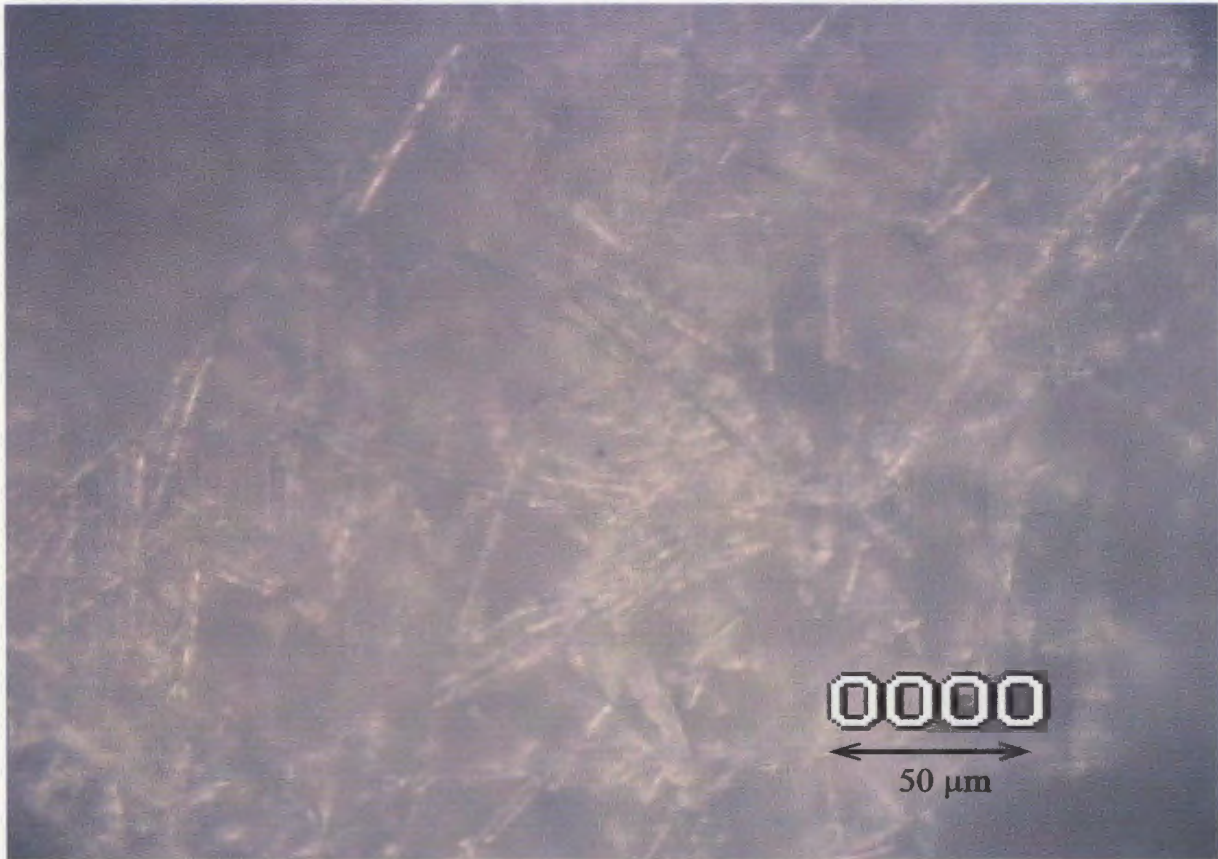
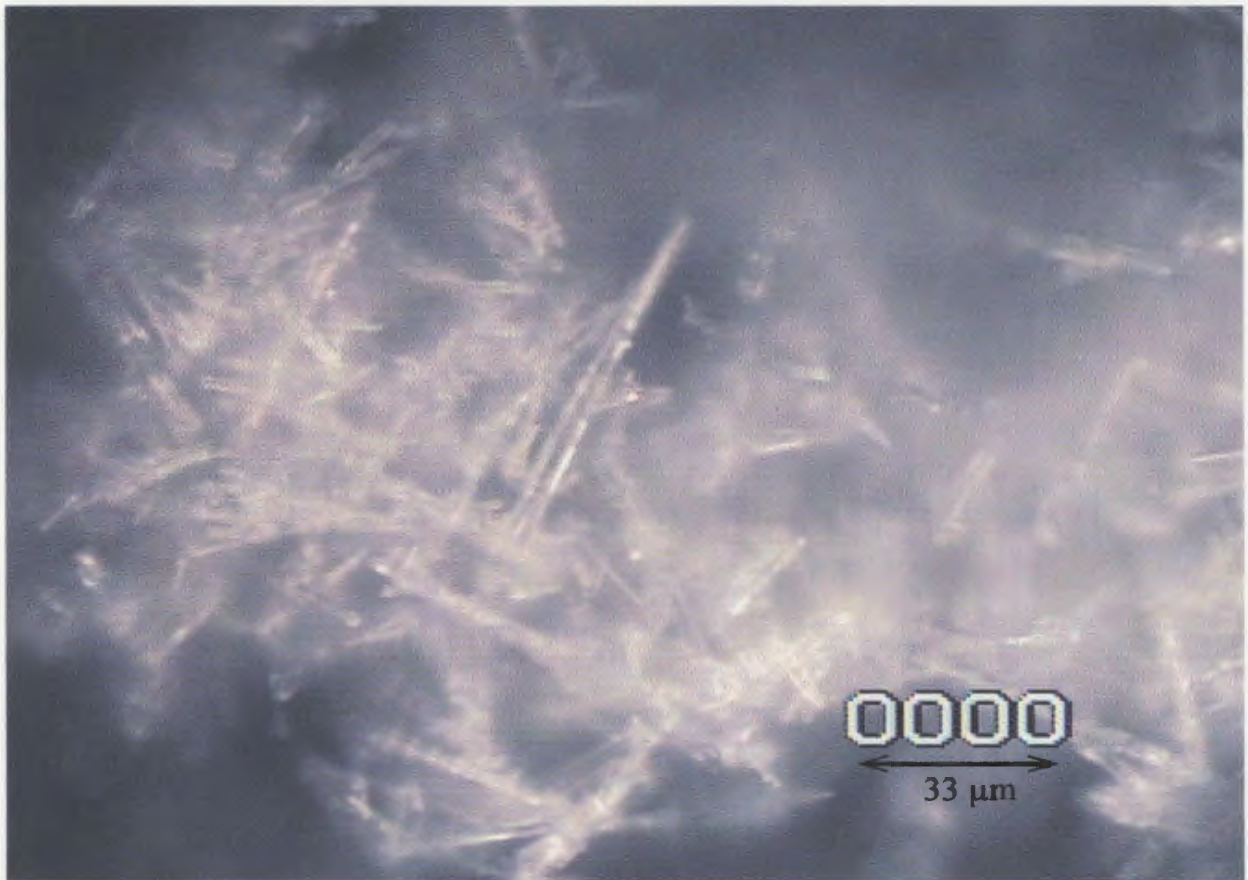


Figure 4.25 Photomicrograph (20x magnification) of aragonite removed immediately after the precipitation showing the "needle-like" shape of the crystals.



**Figure 4.26** Photomicrograph (50x magnification) of aragonite removed immediately after the precipitation showing the "needle-like" shape of the crystals.

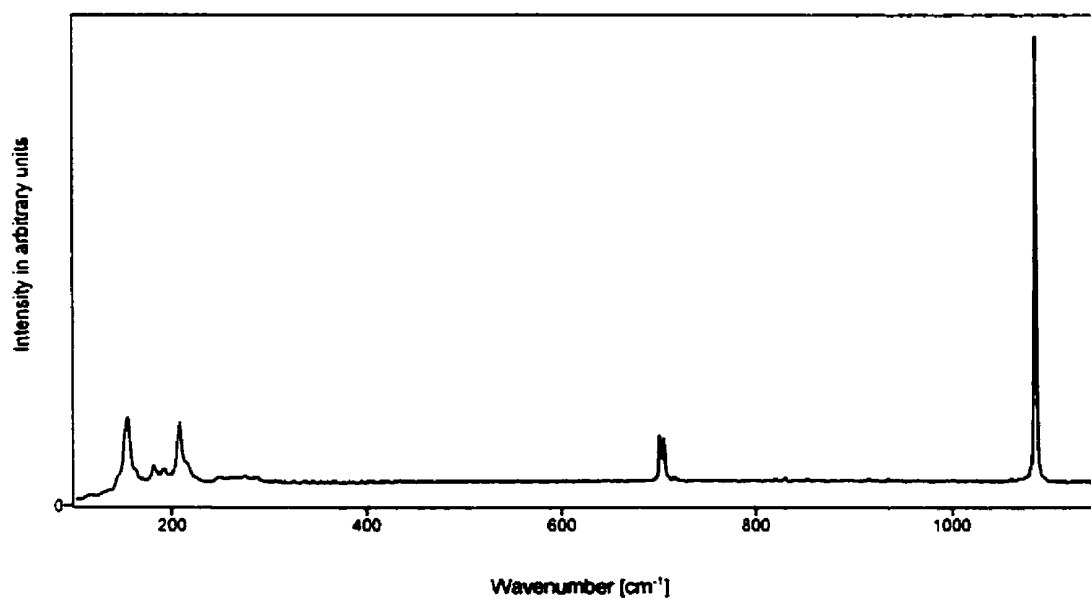


Figure 4.27 Overview Raman spectrum of natural aragonite at 25 °C displaying the region from 100-1150  $\text{cm}^{-1}$ .

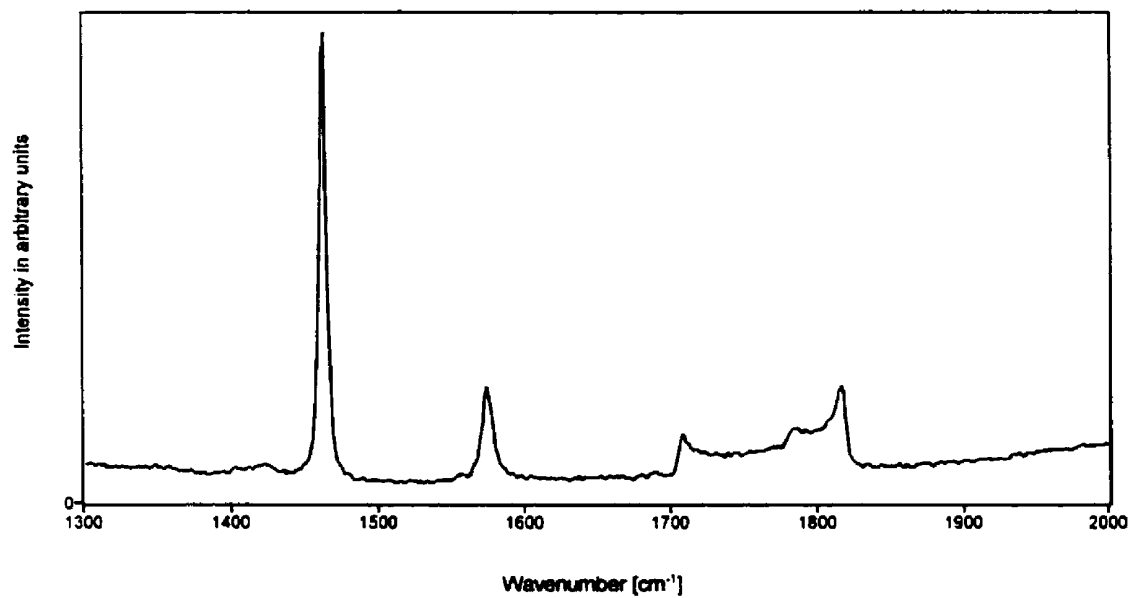


Figure 4.28 Raman spectrum of the  $\nu_3$  internal vibrational mode region and  $2\nu_2$  overtone region of natural aragonite at 25 °C.

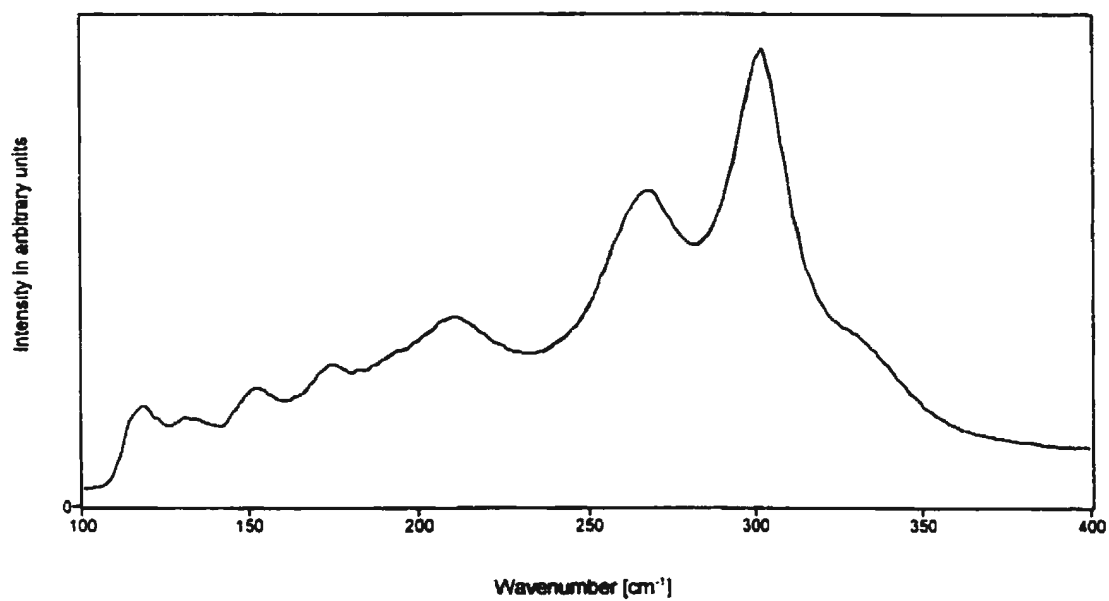


Figure 4.29 Raman spectrum of the external lattice mode region of vaterite at 25 °C.

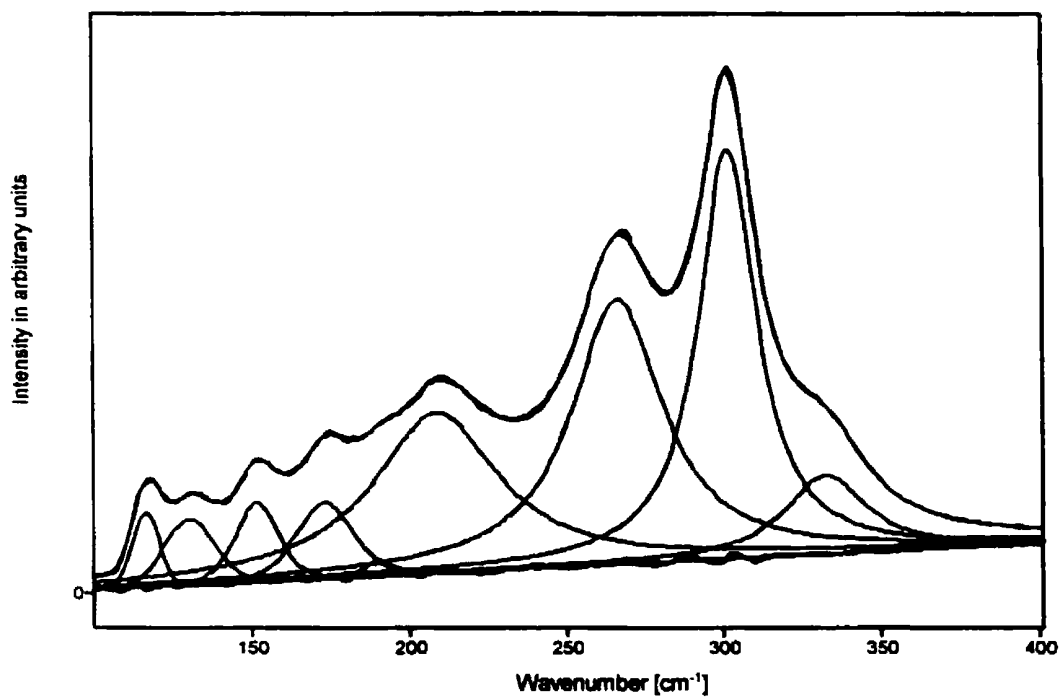


Figure 4.29a Curve fit of the Raman spectrum of the external lattice mode region of vaterite at 25 °C.

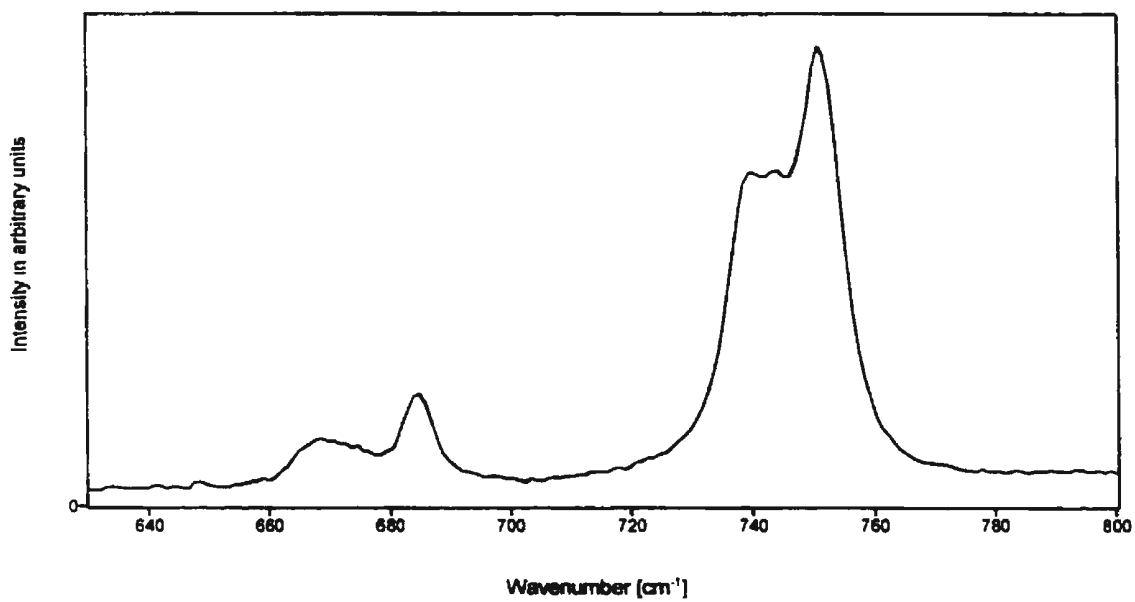


Figure 4.30 Raman spectrum of the  $\nu_4$  internal vibrational mode region of vaterite at 25 °C.

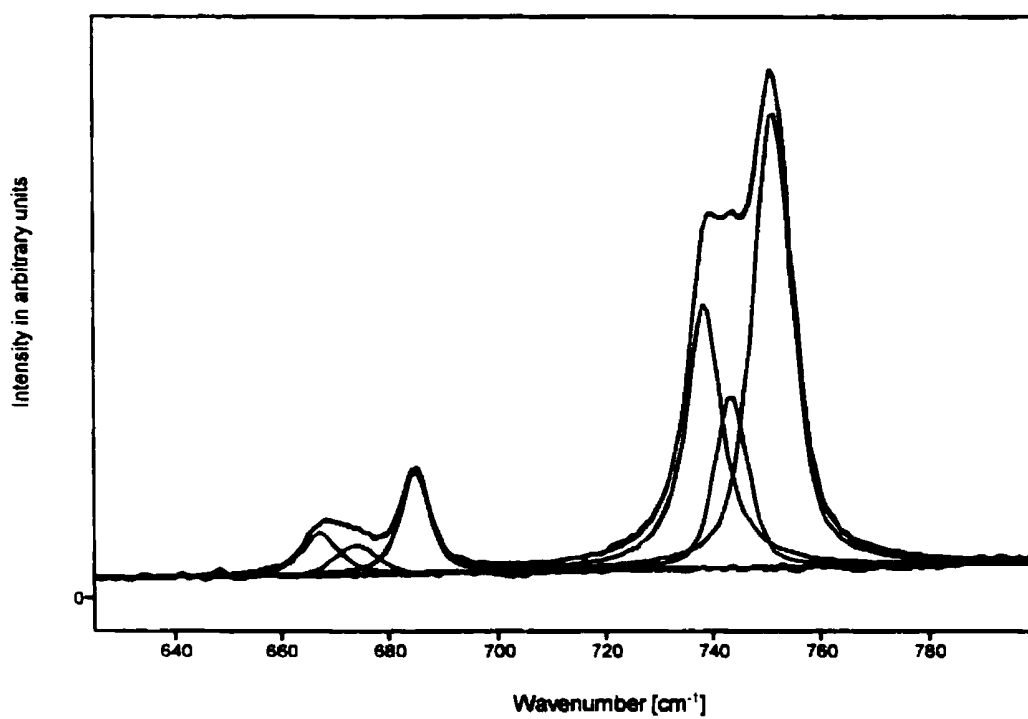


Figure 4.30a Curve fit of the Raman spectrum of the  $\nu_4$  internal vibrational mode region of vaterite at 25 °C.

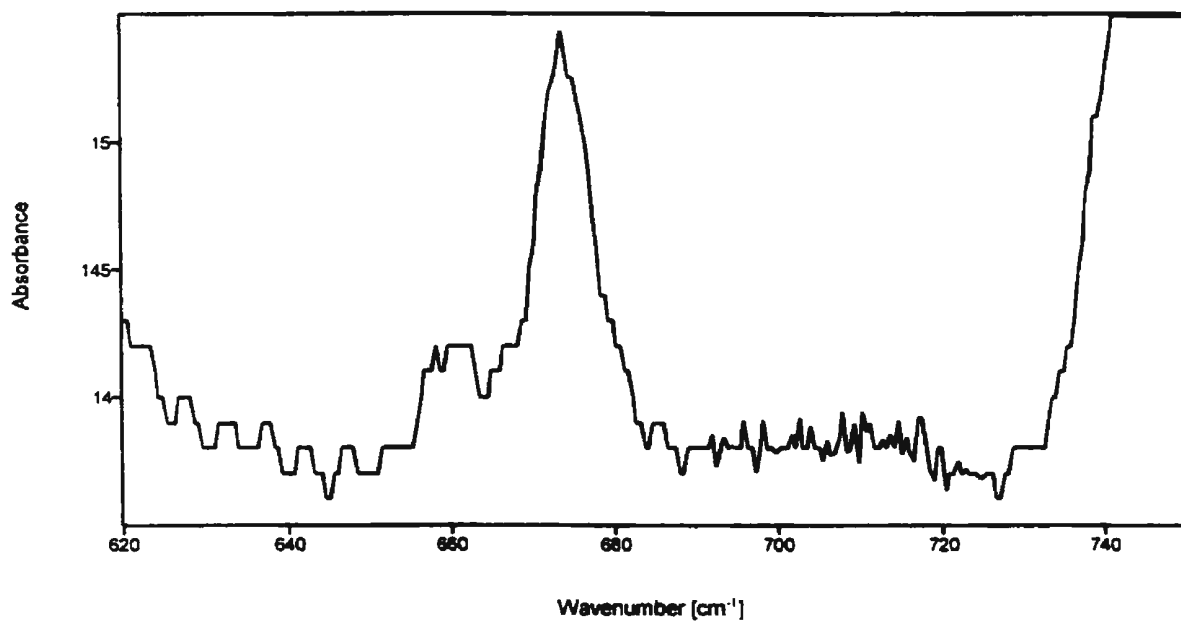


Figure 4.31 Infrared spectrum of the  $\nu_1$  internal vibrational mode region (lower  $\text{cm}^{-1}$  region) of vaterite at 25 °C.

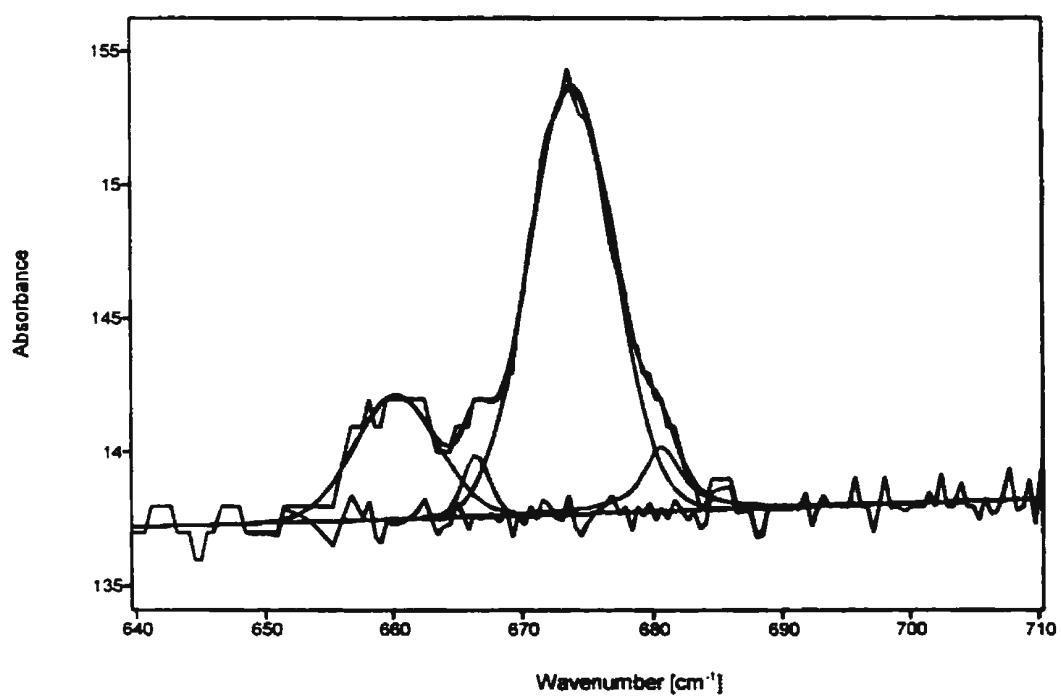


Figure 4.31a Curve fit of the infrared spectrum of the  $\nu_1$  internal vibrational mode region (lower  $\text{cm}^{-1}$  region) of vaterite at 25 °C.

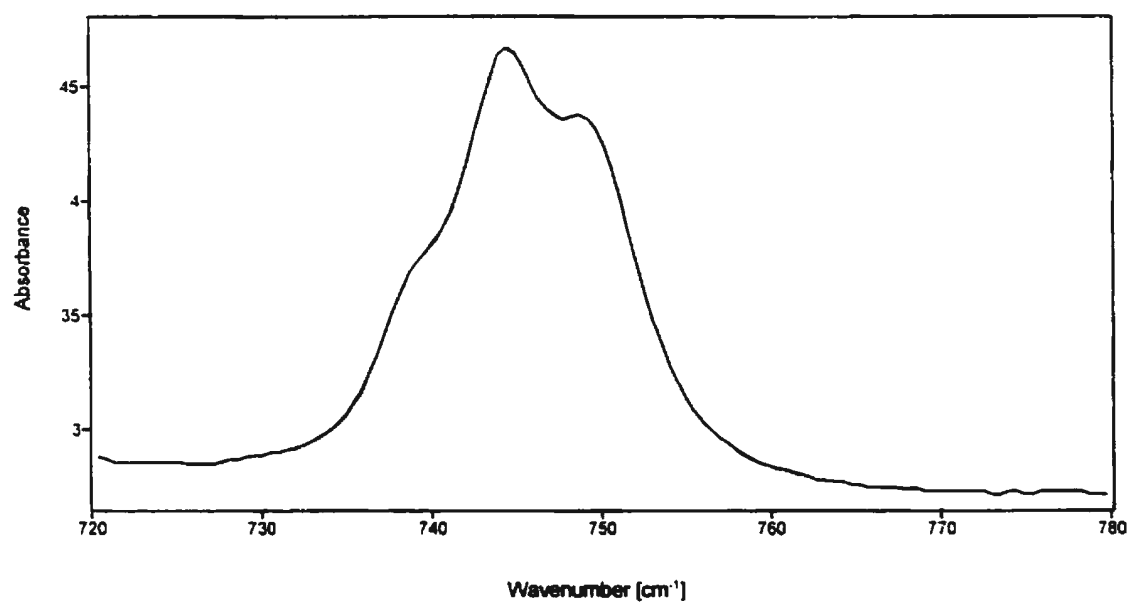


Figure 4.32 Infrared spectrum of the  $\nu_3$  internal vibrational mode region (higher  $\text{cm}^{-1}$  region) of vaterite at 25 °C.

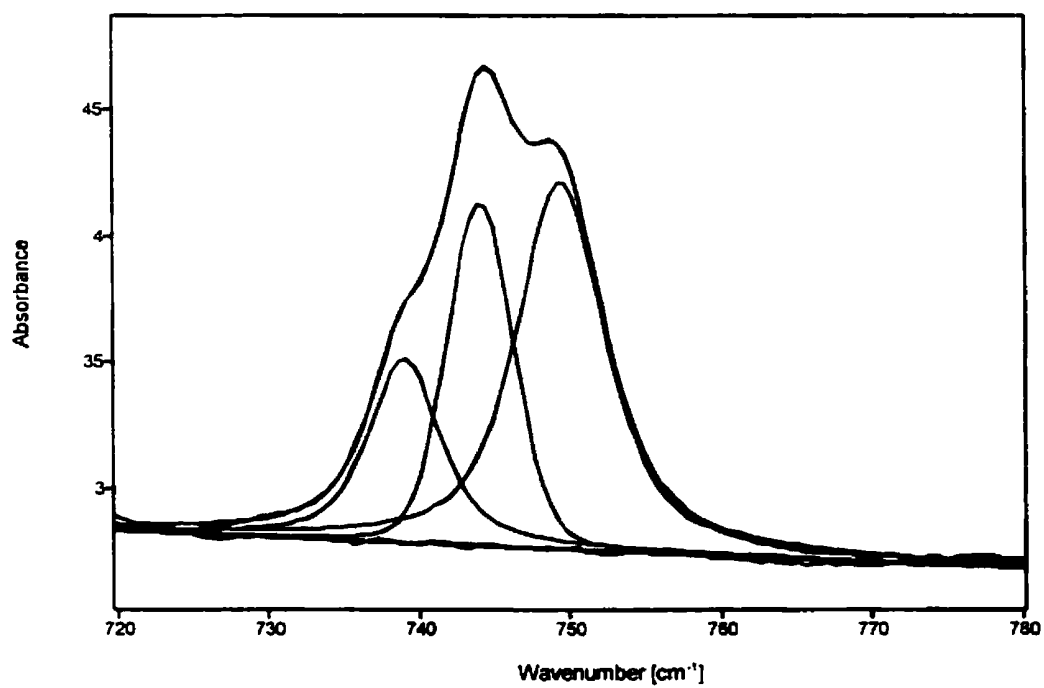


Figure 4.32a Curve fit of the infrared spectrum of the  $\nu_1$  internal vibrational mode region (higher  $\text{cm}^{-1}$  region) of vaterite at 25 °C.

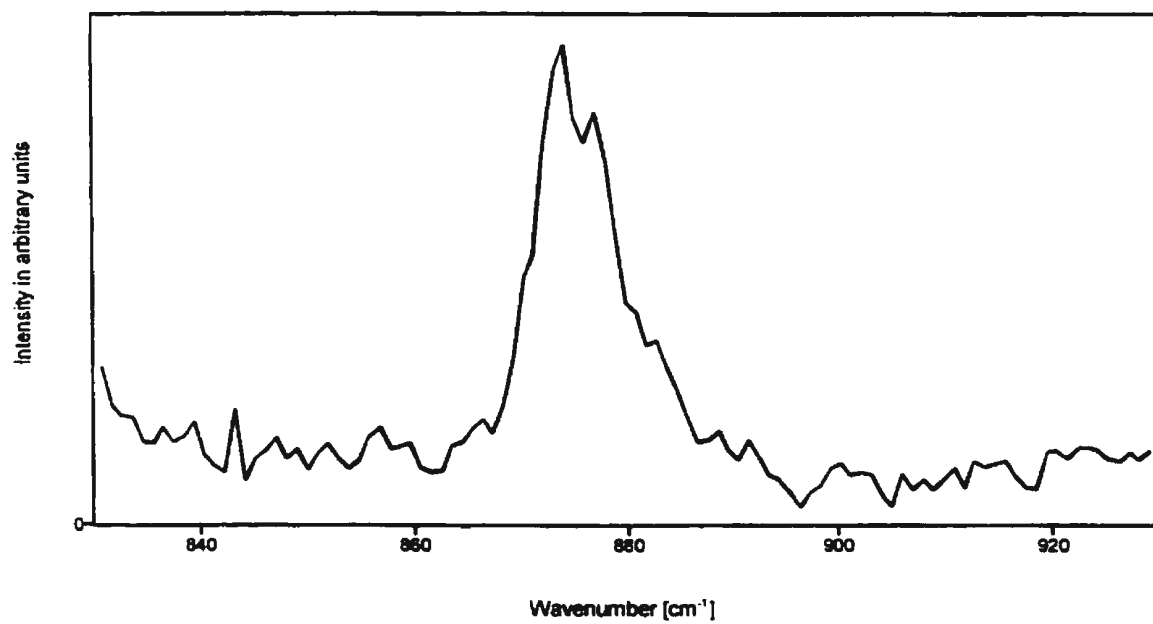


Figure 4.33 Raman spectrum of the  $\nu_2$  internal vibrational mode region of vaterite at 25 °C.

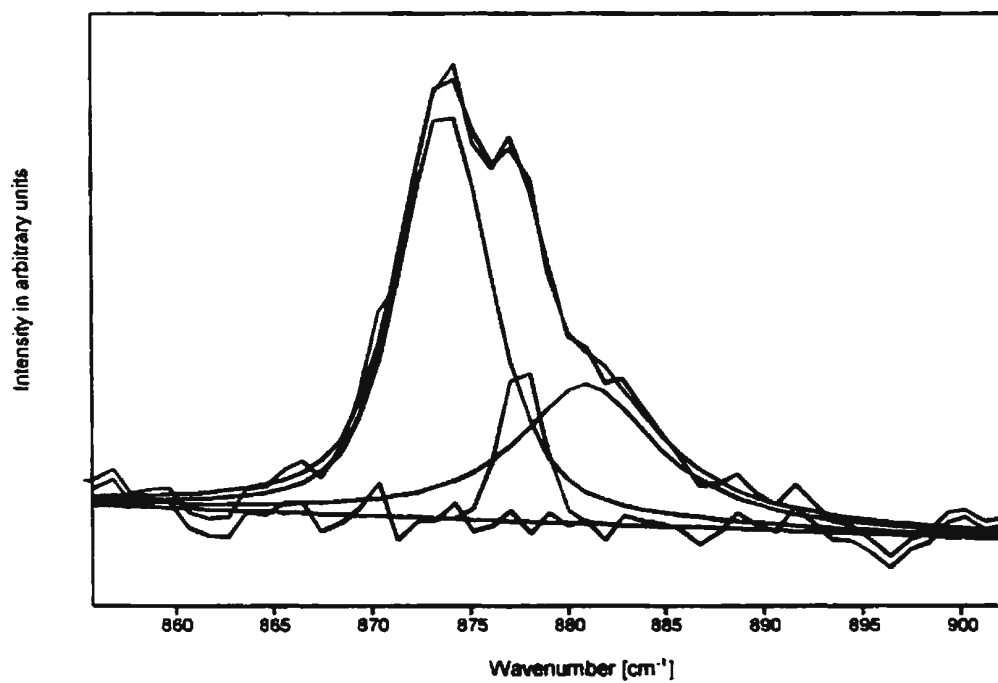


Figure 4.33a Curve fit of the Raman spectrum of the  $\nu_2$  internal vibrational mode region of vaterite at 25 °C.

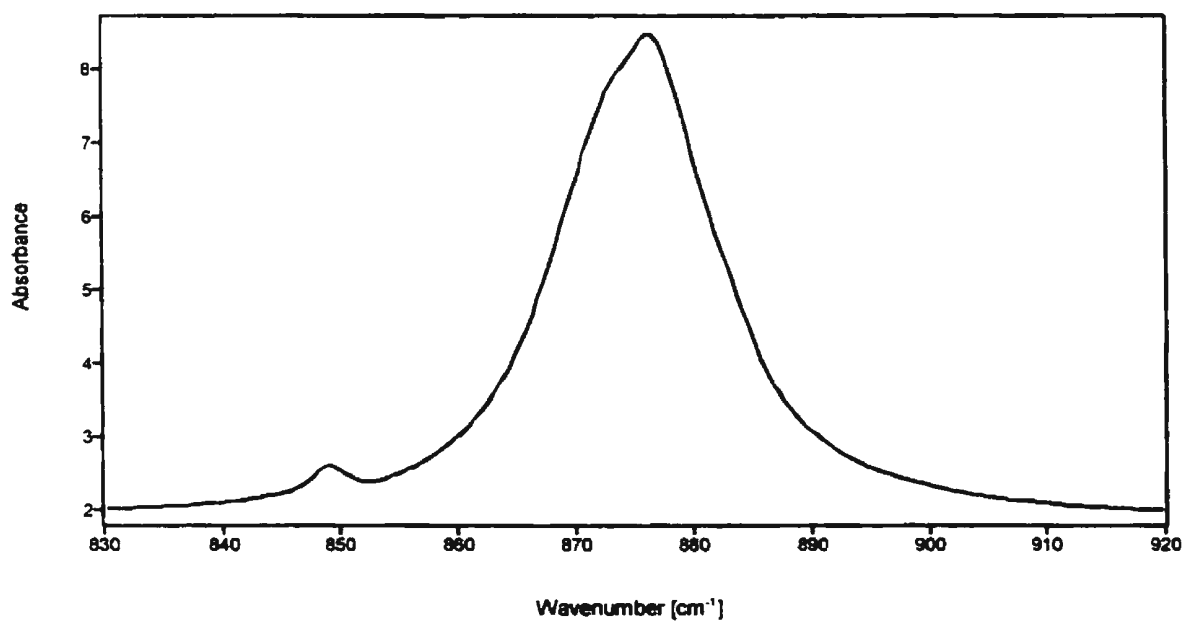


Figure 4.34 Infrared spectrum of the  $\nu_2$  internal vibrational mode region of vaterite at 25 °C.

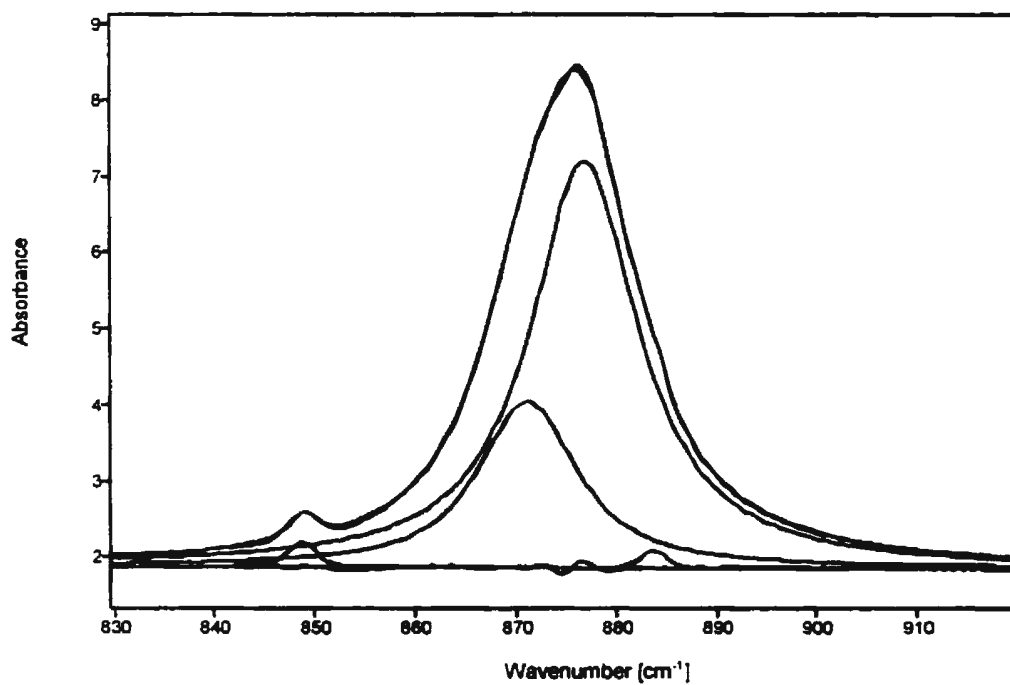


Figure 4.34a Curve fit of the infrared spectrum of the  $\nu_2$  internal vibrational mode region of vaterite at 25 °C.

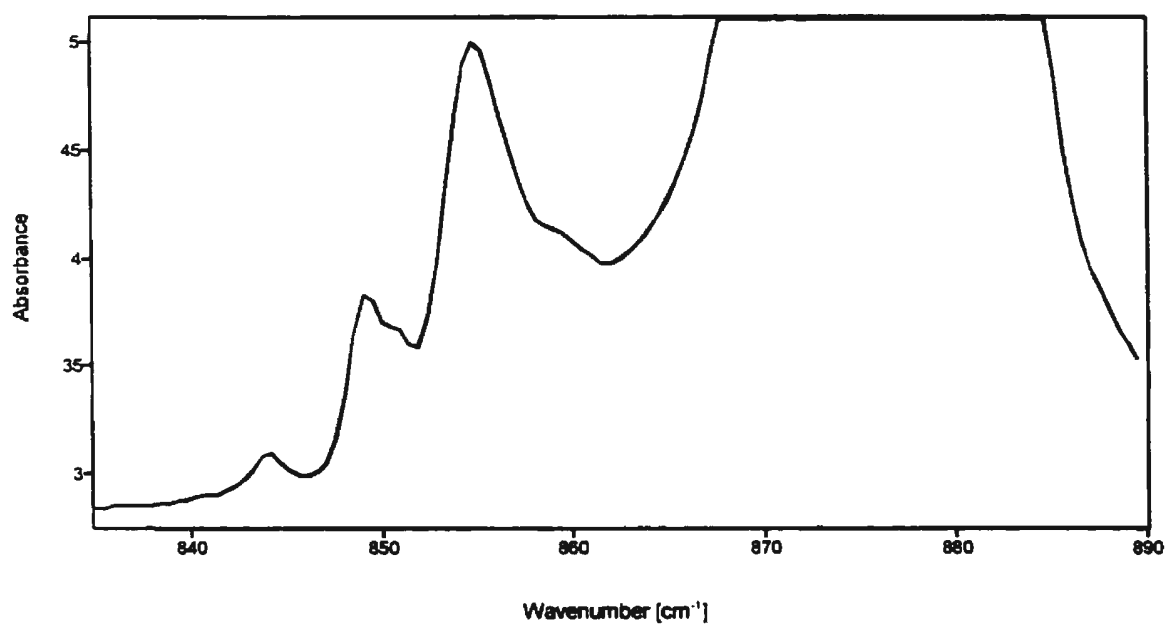


Figure 4.35 Infrared spectrum of the  $^{13}\text{C}$  region of the  $\nu_2$  internal vibrational mode of vaterite at 25  $^{\circ}\text{C}$ .

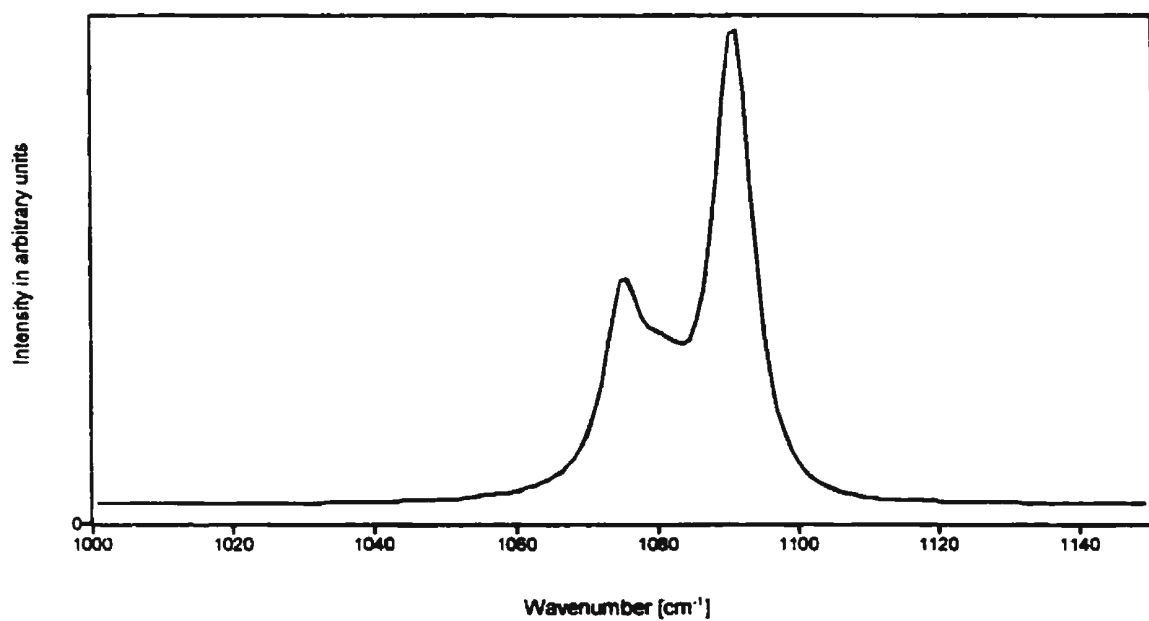


Figure 4.36 Raman spectrum of the  $\nu_1$  internal vibrational mode region of vaterite at 25 °C.

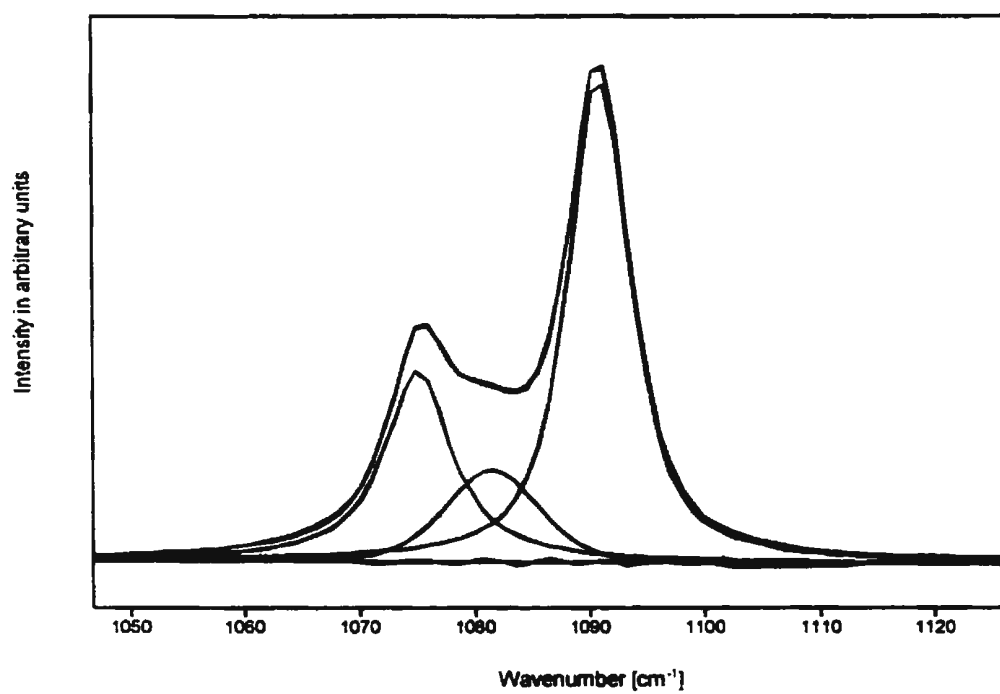


Figure 4.36a Curve fit of the Raman spectrum of the  $\nu_1$  internal vibrational mode region of vaterite at 25 °C.

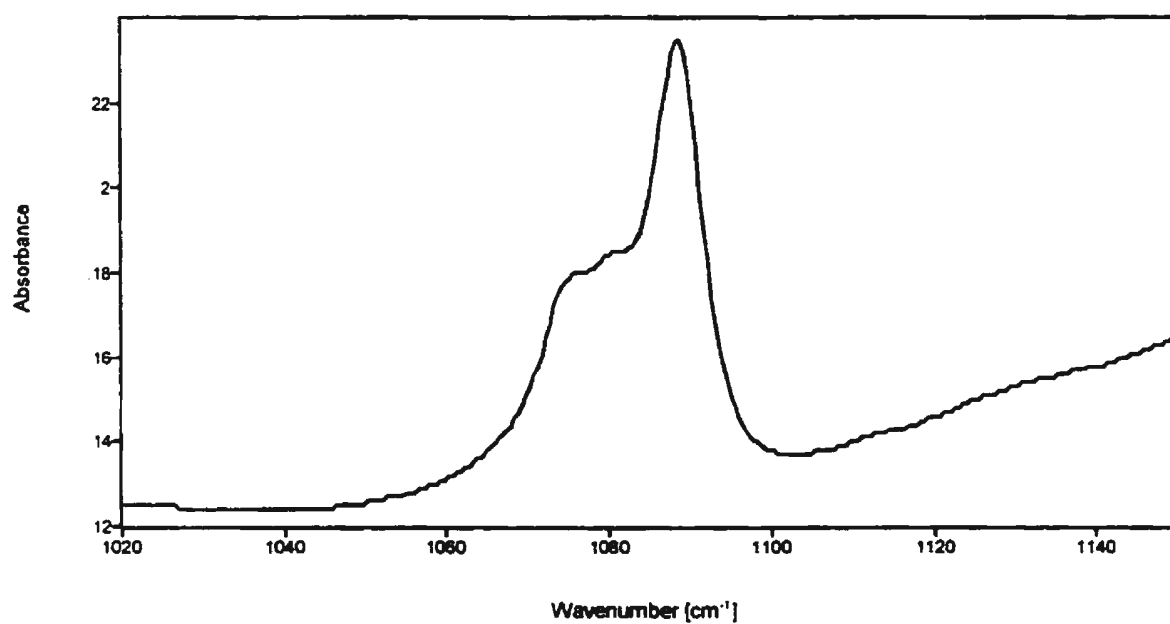


Figure 4.37 Infrared spectrum of the  $\nu_1$  internal vibrational mode region of vaterite at 25 °C.

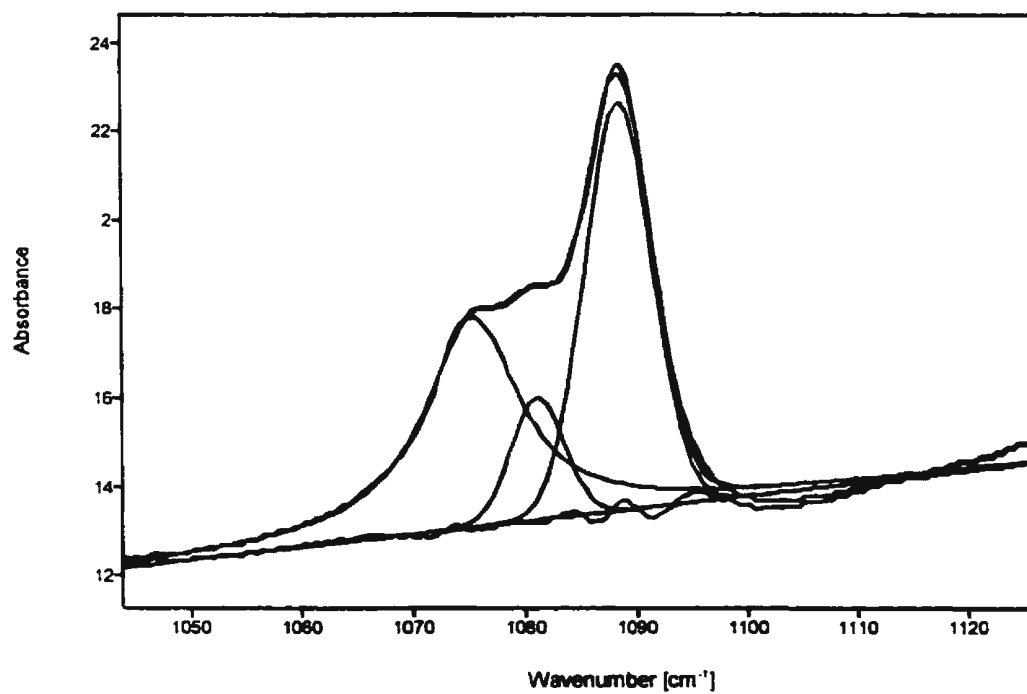


Figure 4.37a Curve fit of the infrared spectrum of the  $\nu_1$  internal vibrational mode region of vaterite at 25 °C.

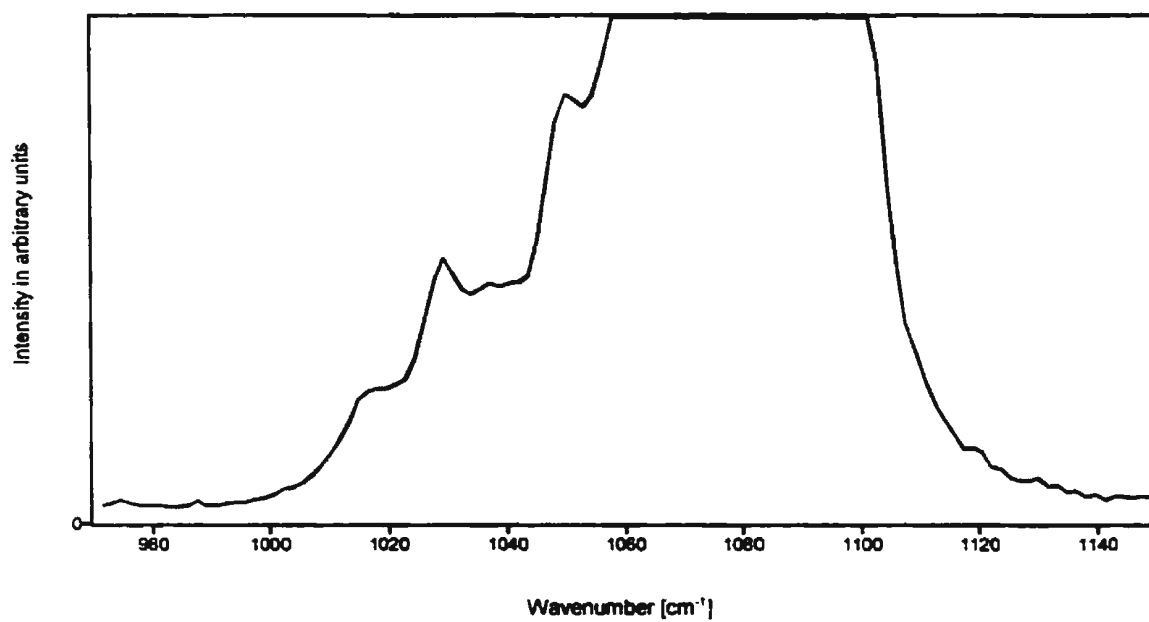


Figure 4.38 Raman spectrum of the  $^{18}\text{O}$  region of the  $\nu_1$  internal vibrational mode of vaterite at 25 °C.

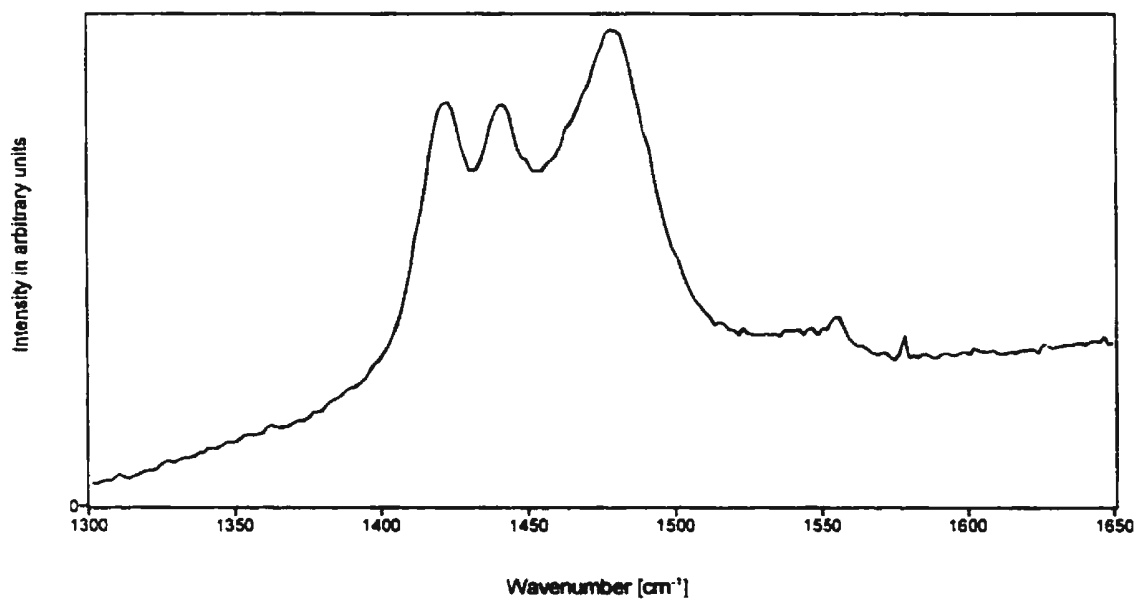


Figure 4.39 Raman spectrum of the  $\nu_3$  internal vibrational mode region of vaterite at 25 °C.

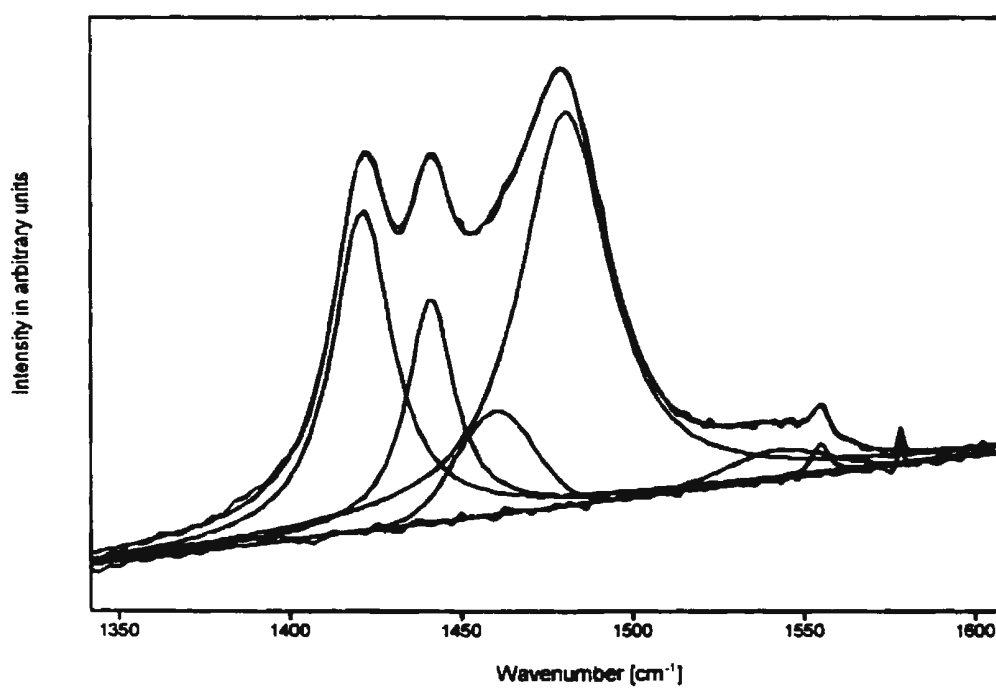


Figure 4.39a Curve fit of the Raman spectrum of the  $\nu_3$  internal vibrational mode region of vaterite at 25 °C.

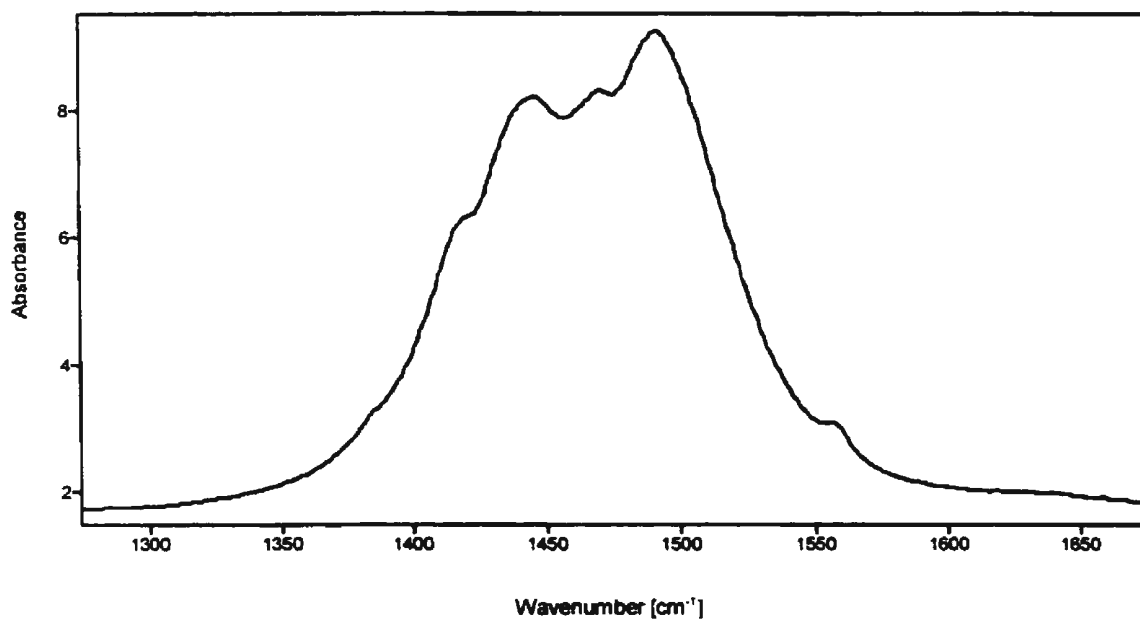


Figure 4.40 Infrared spectrum of the  $\nu_3$  internal vibrational mode region of vaterite at 25 °C.

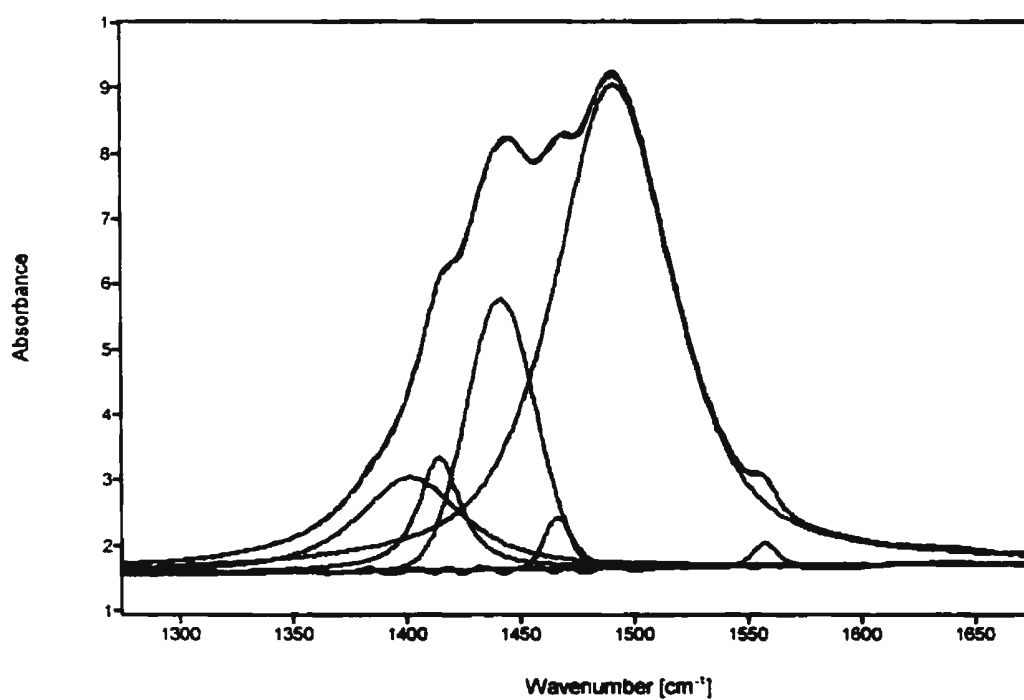


Figure 4.40a Curve fit of the infrared spectrum of the  $\nu_3$  internal vibrational mode region of vaterite at 25 °C.

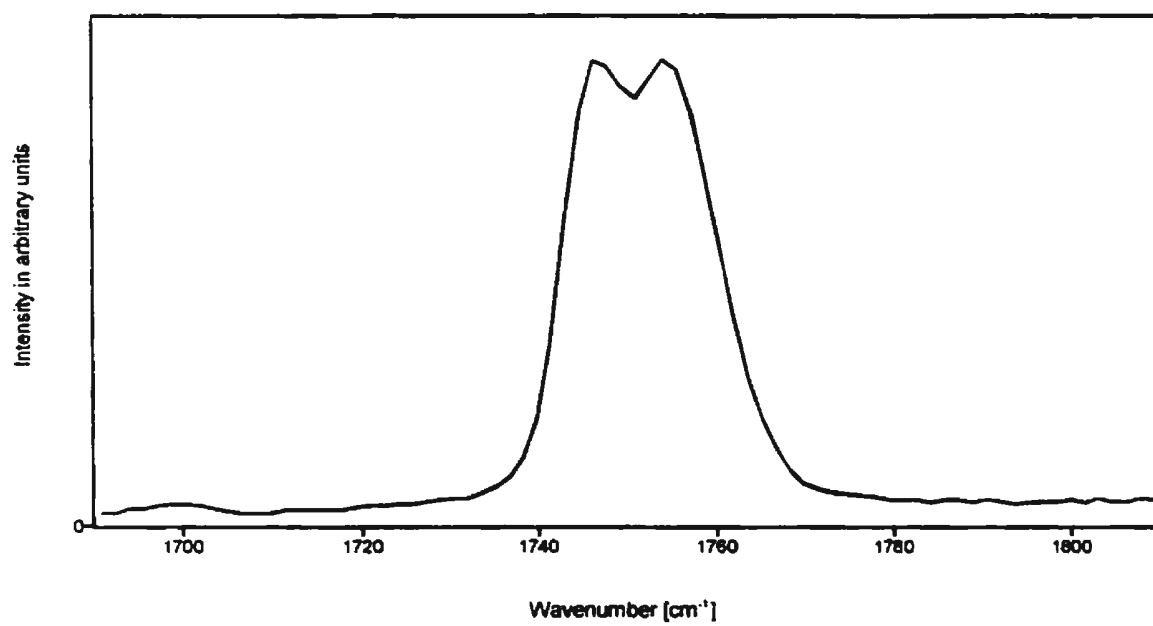


Figure 4.41 Raman spectrum of the  $2\nu_2$  overtone region of vaterite at 25 °C.

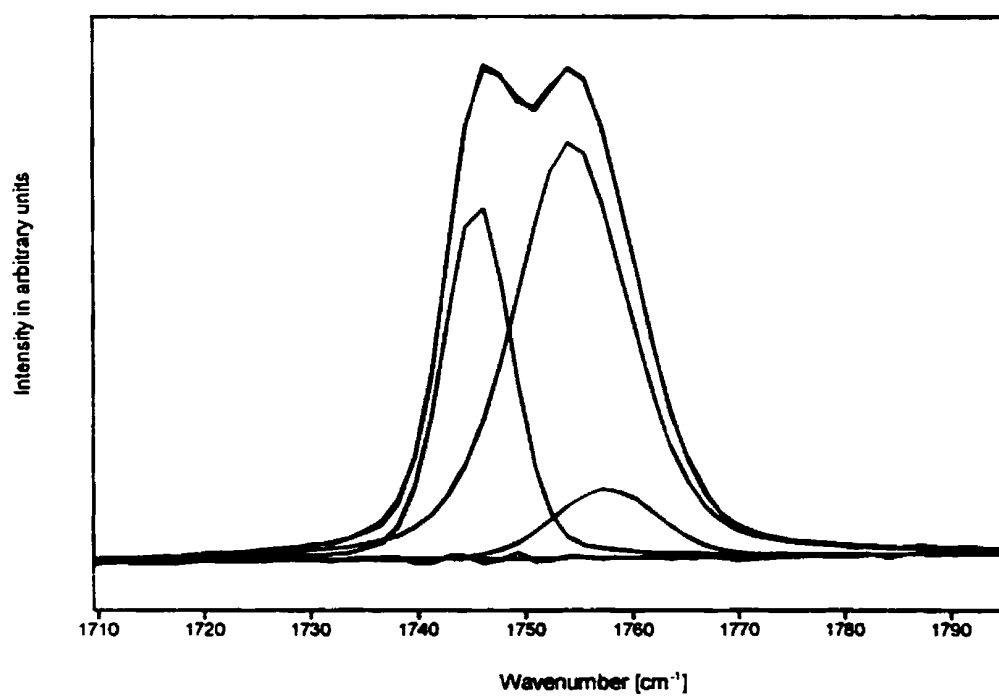


Figure 4.41a Curve fit of the Raman spectrum of the  $2\nu_2$  overtone region of vaterite at 25 °C.

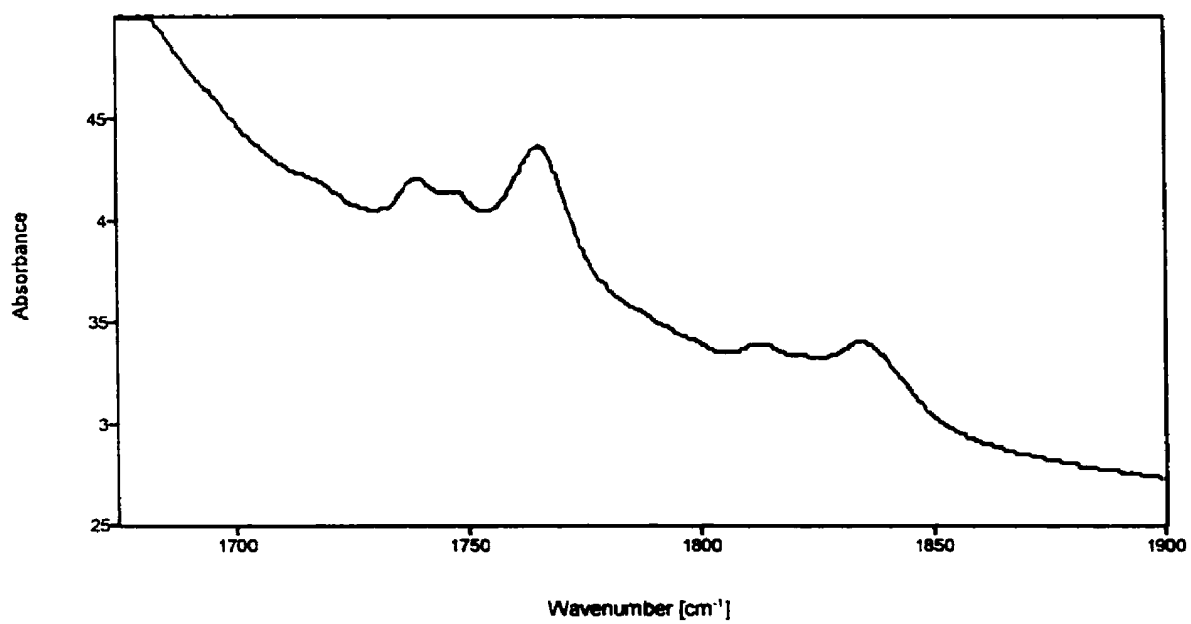


Figure 4.42 Infrared spectrum of the  $[\nu_4 + \nu_1]$  combination band region of vaterite at 25 °C.

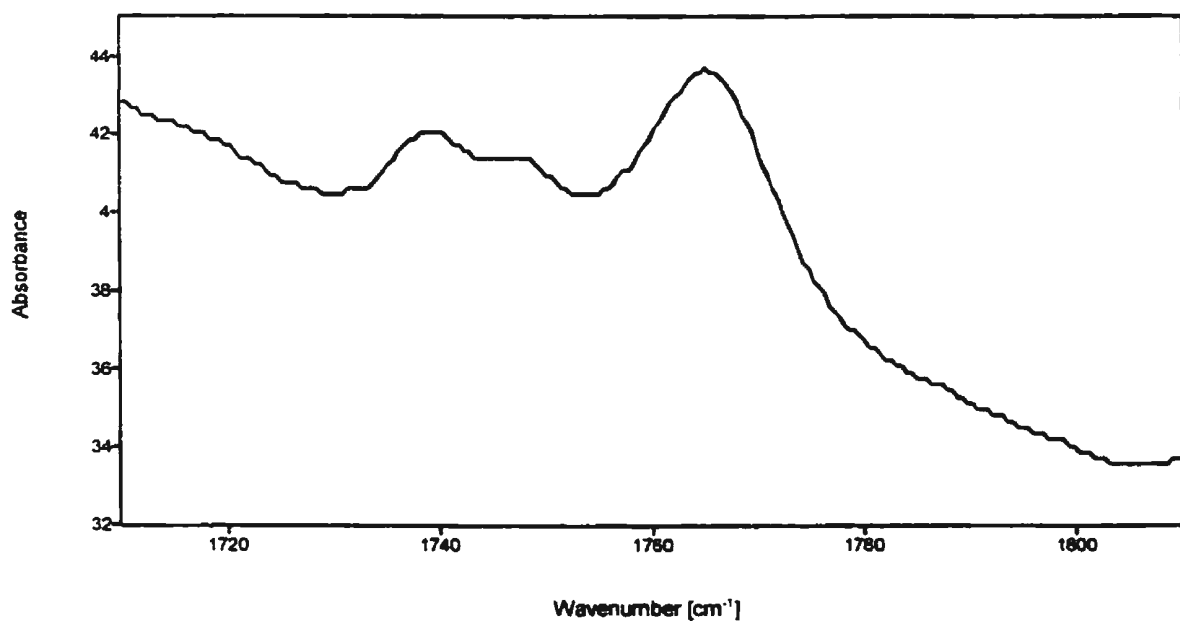


Figure 4.42a Infrared spectrum of the  $[\nu_4 + \nu_1]$  combination band region (lower  $\text{cm}^{-1}$  region) of vaterite at 25 °C.

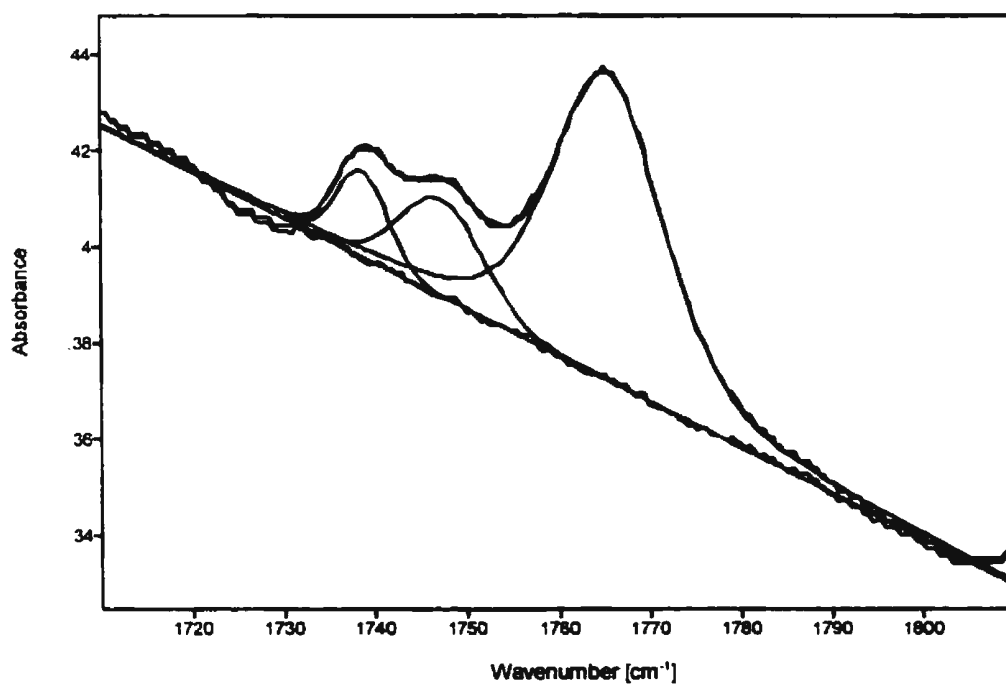


Figure 4.42b Curve fit of the infrared spectrum of the  $[\nu_1+\nu_1]$  combination band region (lower  $\text{cm}^{-1}$  region) of vaterite at 25 °C.

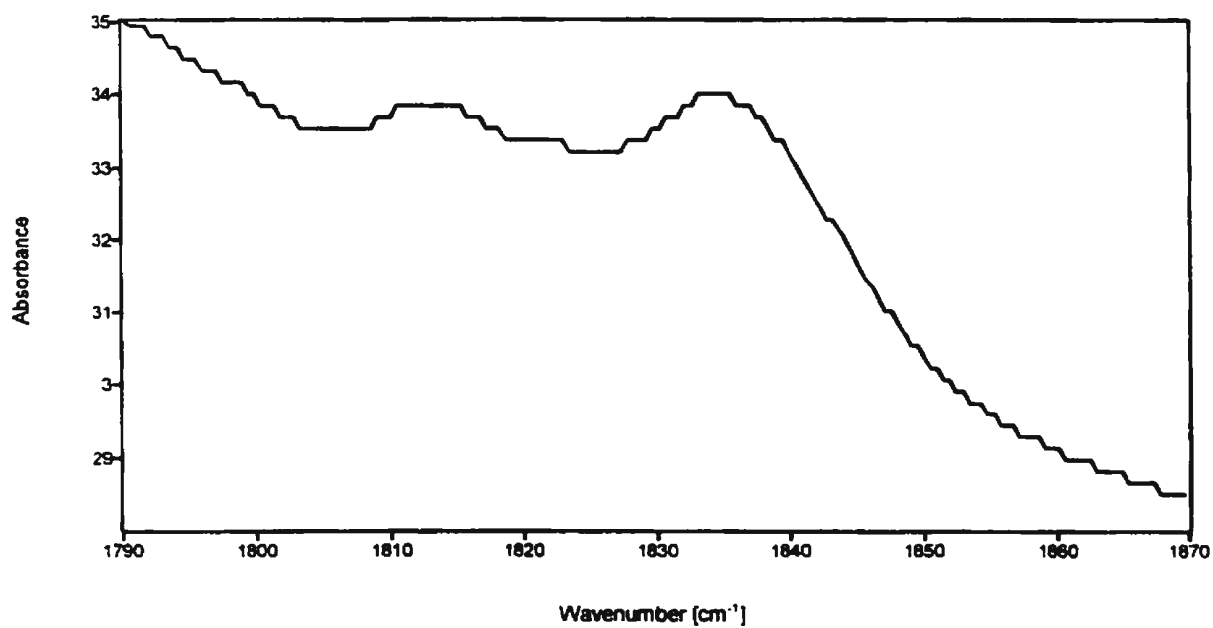


Figure 4.42c Infrared spectrum of the  $[\nu_4+\nu_1]$  combination band region (higher  $\text{cm}^{-1}$  region) of vaterite at 25 °C.

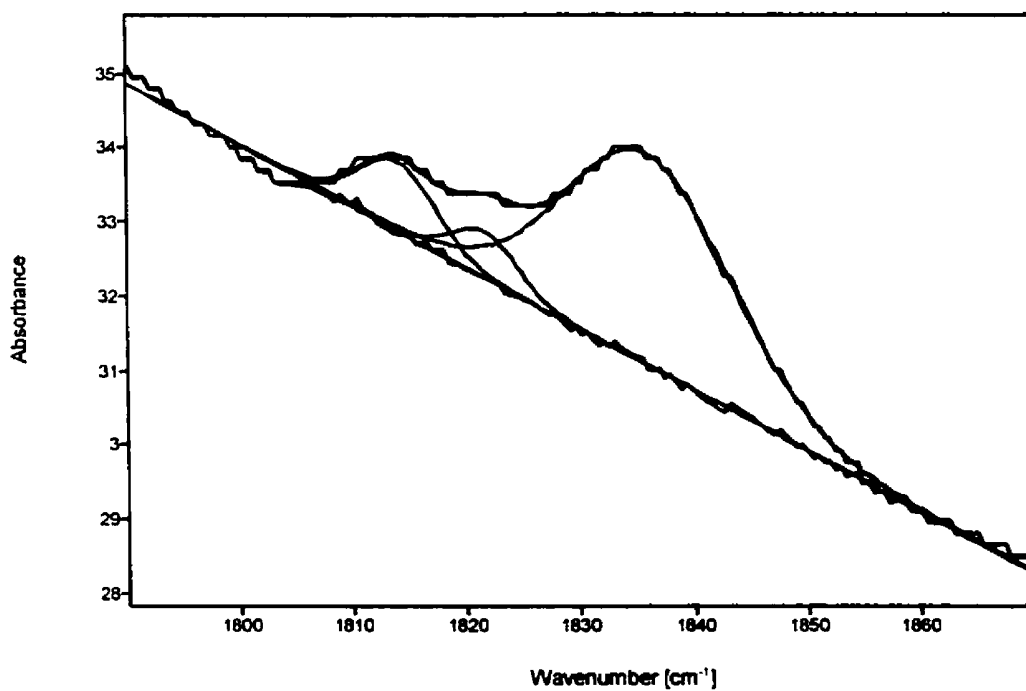


Figure 4.42d Curve fit of the infrared spectrum of the  $[v_4+v_1]$  combination band region (higher  $\text{cm}^{-1}$  region) of vaterite at 25 °C.

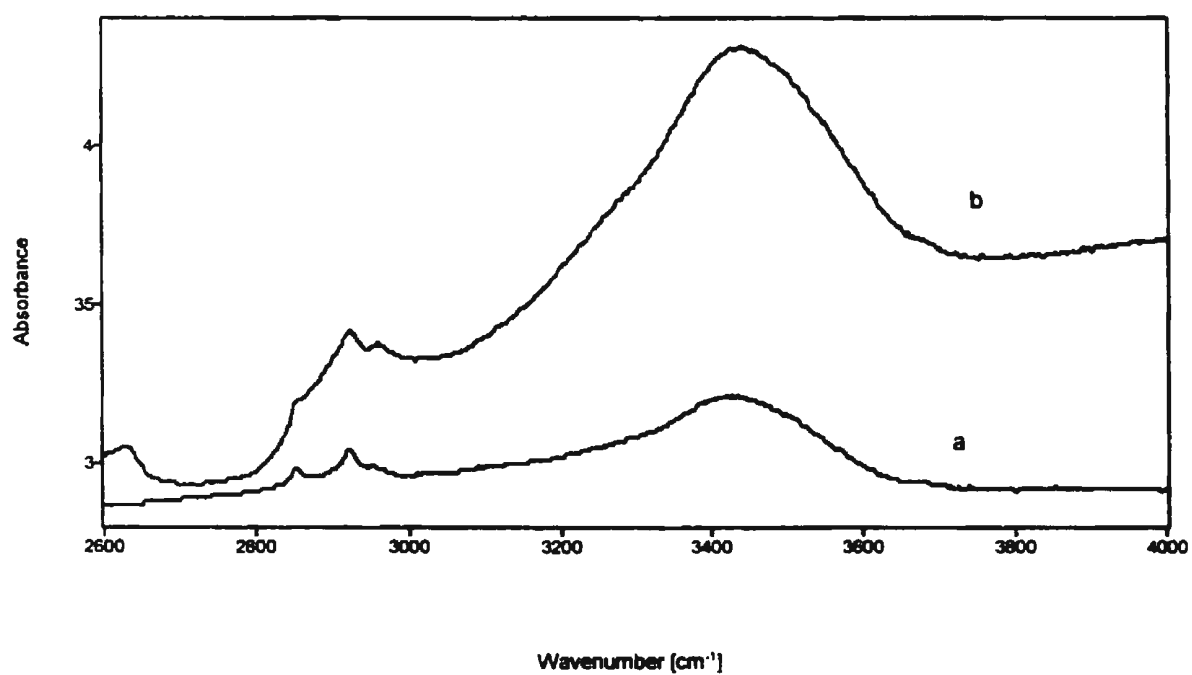


Figure 4.43 Infrared spectra of spectroscopically pure KBr alone [a], and in combination with vaterite [b], showing the presence and relative amount of water impurities.

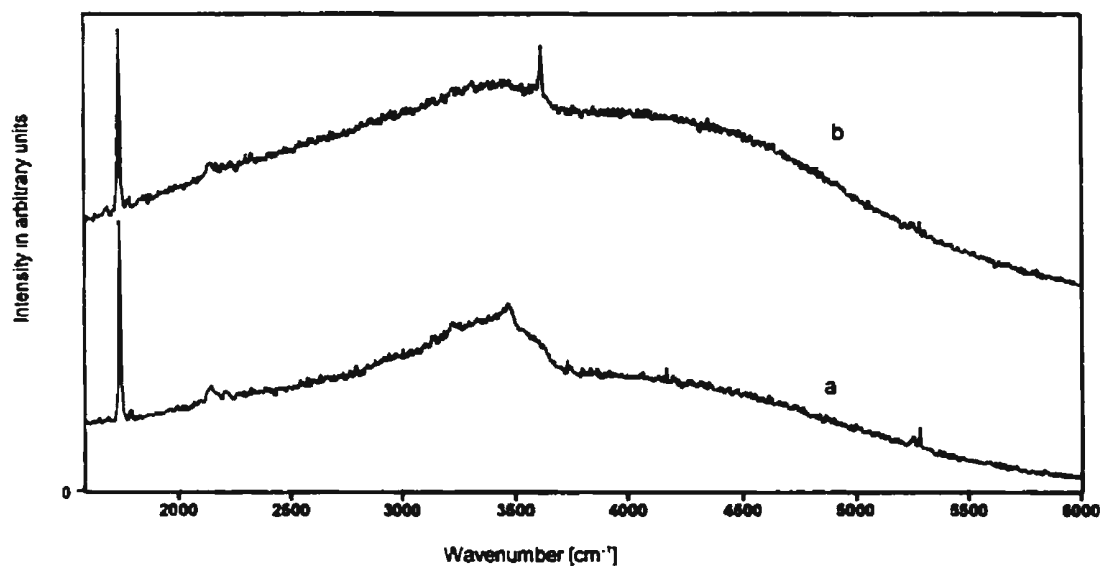


Figure 4.44 Overview Raman spectra of calcite performed before [a] (note the presence of the water band at  $\approx 3400\text{ cm}^{-1}$ ) and after [b] heating to  $220\text{ }^{\circ}\text{C}$ , showing the removal of water and the increase in fluorescence due to manganese(II) impurities.

## **Chapter 5**

### **Conclusions**

The precipitation of  $\text{CaCO}_3$  has been studied using a variety of techniques. Under suitable experimental conditions, it has been found possible to promote the formation of metastable phases of  $\text{CaCO}_3$ , either as single phases or as mixtures. The growth of these metastable phases is governed predominantly by the kinetics of the reactions which can be controlled by differences in reactant concentrations and temperature. The preparations were relatively simple, only involving variations in the temperature, pressure, concentrations of reactants, stirring rates and duration of precipitation. Previous methods tended to be much more complex as they required the use of chemical additives in order to promote the growth of metastable phases.

A DSC analysis of  $\text{CaCO}_3 \cdot 6\text{H}_2\text{O}$  has been obtained for the first time. The dehydration product was found to be exclusively  $\text{CaCO}_3 \cdot 1\text{H}_2\text{O}$  which subsequently dehydrates to either calcite or vaterite. The endothermic reaction rate for the dehydration of  $\text{CaCO}_3 \cdot 1\text{H}_2\text{O}$  was found to be extremely sensitive to temperature, and to the inclusion of small quantities of water and other  $\text{CaCO}_3$  phases which co-precipitated with the original  $\text{CaCO}_3 \cdot 6\text{H}_2\text{O}$ . Raman spectra of  $\text{CaCO}_3 \cdot 6\text{H}_2\text{O}$  have also been obtained for the first time. The presence of an external lattice mode, together with well-defined bands in both the internal vibrational mode regions and O-H stretching region with relatively small FWHH's, all suggest an ordered crystal

structure. These results are in agreement with the well-ordered crystal structure proposed by Adams (Adams, 1974).

Raman spectra of  $\text{CaCO}_3 \cdot \text{H}_2\text{O}$  have also been obtained for the first time. The absence of external lattice modes, together with broad bands in both the internal vibrational mode regions and O-H stretching region with relatively large FWHH's, all suggest a disordered crystal structure. The dehydration product usually consisted mainly of vaterite with small traces of calcite impurities. The reaction rate was found to be largely dependent on the presence of trace impurities of other  $\text{CaCO}_3$  phases which co-precipitated with the  $\text{CaCO}_3 \cdot \text{H}_2\text{O}$ .

Previous studies on vaterite have been inconclusive due to the lack of crystals of sufficient size and purity needed for single crystal analysis (i.e. Raman and infrared spectroscopy, and XRD). Our experimental conditions have led to the formation of vaterite crystals of sufficient size and purity which were subsequently used in obtaining high quality Raman and infrared vibrational spectra with outstanding signal-to-noise ratios. Raman and infrared spectra are reported for vaterite at 77 and 298 K. The presence of nine well-defined, distinct bands in the external lattice mode region of the Raman spectrum is consistent with the large number of formula units proposed for the unit cell of vaterite ( $Z = 12$ ) (Meyer, 1969). An  $^{18}\text{O}$  isotopic study of the  $\nu_1$  internal vibrational mode of the Raman spectrum of vaterite has confirmed the three components of  $\nu_1$  to be genuine and correspond to at least three distinct symmetric stretching modes. A  $^{13}\text{C}$  isotopic study of the  $\nu_2$  internal vibrational mode of the infrared spectrum of vaterite has shown there to be at least five distinct out-of-

plane deformation modes and, accordingly, at least five formula units within the unit cell. Furthermore, the structure was found to be non-centrosymmetric, as proposed by Lippmann (1973), due to the coincidence of band frequencies in the Raman and infrared vibrational spectra. Trace amounts of water and manganese(II) impurities detected within the vaterite crystals are proposed to be a result of the fast precipitation required and its relatively open structure.

The vibrational spectra of vaterite show features similar to those found in the vibrational spectra of  $\gamma\text{-Na}_2\text{CO}_3$ . To date,  $\gamma\text{-Na}_2\text{CO}_3$  is the only known incommensurate phase of the alkali-metal carbonates, but the similarity in vibrational spectra with  $\gamma\text{-Na}_2\text{CO}_3$ , combined with the relatively open structure observed for vaterite and the proposed number of formula units within the unit cell ( $Z = 12$ ), all suggest that vaterite is also an incommensurate phase.

Micro-Raman spectroscopy has been found to be sufficiently sensitive and efficient in the identification of short-lived metastable phases, and in the determination of their relative purities. In conjunction with other methods, such as DSC, FT-IR, TG-EGA and XRD, it acts as an excellent analytical tool in the field of combinatorial chemistry.

## **Bibliography**

- Aalst, W. Van, Hollander, J. Den, Peterse, W. J. A. M. and De Wolff, P. M., 1976. The Modulated Structure of  $\gamma$ -Na<sub>2</sub>CO<sub>3</sub> in a Harmonic Approximation. *Acta Cryst.*, B32, pp. 47-58.
- Adams, D. M., 1974. *Inorganic Solids*, pp. 135-136, Published by John Wiley and Sons.
- Anderson, A., 1996. Group Theoretical Analysis of The  $\nu_1$  (CO<sub>3</sub><sup>2-</sup>) Vibration in Crystalline Calcium Carbonate. *Spectroscopy Letters*, Vol. 29, No. 5, pp. 819-825.
- Bates, J. B., Brooker, M. H., Quist, A. S. and Boyd, G. E., 1972. Raman Spectra of Molten Alkali Metal Carbonates. *The Journal of Physical Chemistry*, Vol. 76, No. 11, pp. 1565-1571.
- Behrens, G., Kuhn, L. T., Ubic, R. and Heuer, A. H., 1995. Raman Spectra of Vateritic Calcium Carbonate. *Spectroscopy Letters*, Vol. 28, No. 6, pp. 983-995.
- Blackburn, W. H. and Dennen, W. H., 1994. *Principles of Mineralogy*, 2nd Edition, Published by Wm. C. Brown Publishers.
- Bradley, R. S., Colvin, J. and Hume, J., 1932. On The Mass Rate Reactions in Solids. *Roy. Soc. Proc., A*, 137, pp. 531-541.
- Bradley, W. F., Graf, D. L. and Roth, R. S., 1966. The Vaterite-Type ABO<sub>3</sub> Rare-Earth Borates. *Acta Cryst.*, 20, pp. 283-287.
- Brooker, M. H. and Bates, J. B., 1971. Raman and Infrared Spectral Studies of Anhydrous Li<sub>2</sub>CO<sub>3</sub> and Na<sub>2</sub>CO<sub>3</sub>. *The Journal of Chemical Physics*, Vol. 54, No. 11, pp. 4788-4796.
- Brooker, M. H. and Chen, J., 1991. Assignment of Transverse Optical-Longitudinal Modes in The Vibrational Spectrum of Solid Sulphur Dioxide. *Spectrochimica Acta*, Vol. 47a, No. 3/4, pp. 315-322.
- Brooker, M. H. and Papatheodorou, G. N., 1983. Vibrational Spectroscopy of Molten Salts and Related Glasses and Vapours. *Advances in Molten Salt Chemistry*, Vol. 5, pp. 26-183.
- Brooker, M. H. and Wang, J., 1993. Raman Studies of a  $\lambda$ -type Phase Transition in Solid Cs<sub>2</sub>CdCl<sub>4</sub>, *Physical Review B*, Vol. 48, No. 18, pp. 13286-13295.

- Brooker, M. H. and Wang, J., 1992. Raman and Infrared Studies of Lithium and Cesium Carbonates. *Spectrochimica. Acta*, Vol. 48a, No. 7, pp. 999-1008.
- Brooks, R., Clark, L. M. and Thurston, E. F., 1950. Calcium Carbonate and Its Hydrates. *Phil. Trans.*, Vol. 243, A. 86I, pp. 145-167.
- Bruce, A. D. and Cowley, R. A., 1981. *Structural Phase Transitions*, Published by Taylor and Francis Limited.
- Buanam-Om-Danvirutai, C. and Luck, W. A. P., 1987. Raman Spectra of Water in Crystalline Hydrates. *Spectroscopy Letters*, 20, pp. 331-341.
- Chakraborty, D., Agarwal, V. K., Bhatia, S. K. and Bellare, J., 1994. Steady-State Transitions and Polymorph Transformations in Continuous Precipitation of Calcium Carbonate. *Industrial Engineering and Chemistry Research*, 33, pp. 2187-2197.
- Copisarow, M., 1923. Heteromorphism of Calcium Carbonate. Marble, Synthetic and Metamorphic. *J. Chem. Soc.*, 123, pp. 785-796.
- Decius, J. C. and Hexter, R. M., 1977. *Molecular Vibrations in Crystals*, Published by McGraw-Hill Incorporated.
- De Wolff, P. M. and Tuinstra, F., 1986. The Incommensurate Phase of  $\text{Na}_2\text{CO}_3$ . In "Incommensurate Phases in Dielectrics 2. Materials", pp. 253-281, Edited by Blinc, R. and Levanyuk, A. P., Published by Elsevier.
- Dubbeldam, G. C. and De Wolff, P. M., 1969. The Average Structure of  $\gamma\text{-Na}_2\text{CO}_3$ . *Acta Cryst.*, B25, pp. 2665-2667.
- Farmer, V. C., 1974. *The Infrared Spectra of Minerals*, Published by the Mineralogical Society.
- Fateley, W. G., Dollish, R., McDevitt, N. T. and Bentley, F., 1972. *Infrared and Raman Selection Rules for Molecular and Lattice Vibrations: The Correlation Method*, Published by John Wiley and Sons.
- Gauldie, R. W., 1993. Polymorphic Crystalline Structure of Fish Otoliths. *Journal of Morphology*, 218, pp. 1-28.
- Gauldie<sup>1</sup>, R. W., 1996. Effects of Temperature and Vaterite Replacements on The Chemistry of Metal Ions in The Otoliths of *Oncorhynchus Tshawytscha*. *Can. J. Fish.*

Aquat. Sci., 53, pp. 2015-2026.

Gauldie<sup>2</sup>, R. W., 1996. Fusion of Otoconia: A Stage in The Development of The Otolith in The Evolution of Fishes. *Acta Zoologica*, Vol. 77, No. 1, pp. 1-23.

Gauldie, R. W., Sharma, S. K. and Volk, E., 1997. Micro-Raman Spectral Study of Vaterite and Aragonite Otoliths of The Coho Salmon, *Oncorhynchus Kisutch*. *Comp. Biochem. Physiol.*, Vol. 118A, No. 3, pp. 753-757.

Gillet, P., Biellmann, C., Reynard, B. and McMillan, P., 1993. Raman Spectroscopic Studies of Carbonates Part I: High-Pressure and High-Temperature Behaviour of Calcite, Magnesite, Dolomite and Aragonite. *Phys. Chem. Minerals*, Vol. 20, pp. 1-18.

Gillet, P., McMillan, P., Schott, J., Badro, J. and Grzechnik, A., 1996. Thermodynamic Properties and Isotopic Fractionation of Calcite From Vibrational Spectroscopy of <sup>18</sup>O-Substituted Calcite. *Geochimica et Cosmochimica Acta*, Vol. 60, No. 18, pp. 3471-3485.

Goldenfeld, Nigel, 1992. *Lectures on Phase Transitions and The Renormalization Group*, Published by Addison-Wesley Publishing Company.

Gremlich, Hans-Ulrich, 1998. *Infrared and Raman Spectroscopy in Combinatorial Chemistry*. *American Laboratory*, Vol. 30, No. 24, pp. 33-39.

Harris, M. J. and Salje, E. K. H., 1992. The Incommensurate Phase of Sodium Carbonate: An Infrared Absorption Study. *J. Phys.: Condens. Matter*, 4, pp. 4399-4408.

Hume, J., 1925. The Hydrates of Calcium Carbonate. *J. Chem. Soc.*, 127, pp. 1036-1039.

Iqbal, Z., 1984. Basic Concepts and Recent Developments in the Study of Structural Phase Transitions. In "Vibrational Spectroscopy of Phase Transitions", pp. 31-34, Edited by Iqbal, Z. and Owens, F. J., Published by Academic Press.

Johnston, J., Merwin, H. E. and Williamson, E. D., 1916. The Several Forms of Calcium Carbonate. *Am. Jour. Sci., Fourth Series*, Vol. XLI, No. 24, pp. 473-512.

Jones, G. C. and Jackson, B., 1993. *Infrared Transmission Spectra of Carbonate Minerals*, Published by Chapman and Hall.

Kamhi, S. R., 1963. On The Structure of Vaterite, CaCO<sub>3</sub>. *Acta Cryst.*, 16, pp. 770-772.

Kassel, L. S., 1929. Reactions With Very Large Apparent Temperature Coefficients. *J. A.*

C. S., 51, pp. 1136-1145.

Kralj, D., Brečević, L. and Kontrec, J., 1997. Vaterite Growth and Dissolution in Aqueous Solution III. Kinetics of Transformation. *Journal of Crystal Growth*, 177, pp. 248-257.

Krauss, F. and Schriever, 1930. Die Hydrate des Calciumcarbonats. *Zeitschrift für Anorganische und Allgemeine Chemie*, 188, pp. 259-273.

Ladd, M. F. C. and Palmer, R. A., 1993. *Structure Determination by X-ray Crystallography*, Third Edition, Published by Plenum Press.

Laidler, K. J. and Meiser, J. H., 1995. *Physical Chemistry*, 2nd Edition, Published by Houghton Mifflin Company.

Laserna, J. J., 1996. *Modern Techniques in Raman Spectroscopy*, Published by John Wiley and Sons.

Levanyuk, A. P., 1986. General Ideas About Incommensurate Phases. In "Incommensurate phases in Dielectrics 1. Fundamentals", pp. 1-41, Edited by Blinc, R. and Levanyuk, A. P., Published by Elsevier.

Lévy, M., LeGuillou, J. and Zinn-Justin, J., 1982. *Phase Transitions*, Published by Plenum Press.

Lippmann, F., 1973. *Sedimentary Carbonate Minerals*, Published by Springer-Verlag.

Maciejewski, M., Oswald, H. and Reller, A., 1994. Thermal Transformations of Vaterite and Calcite. *Thermochimica Acta*, 234, pp. 315-328.

Maciel, A. and Ryan, J. F., 1981. Observation of Coupled Amplitude Modes in The Raman Spectrum of Incommensurate  $\text{Na}_2\text{CO}_3$ . *J. Phys. Chem.: Solid State Phys.*, Vol. 14, pp. L509-L514.

Mackenzie, J. E., 1923. Calcium Carbonate Hexahydrate. *J. Chem. Soc.*, 123, pp. 2409-2417.

Mason, R. A., 1998. The Response of Luminescence in Synthetic Calcite to Laboratory Heating, *The Canadian Mineralogist*, Vol. 36, pp. 1089-1104.

Matsushita, I., Hamada, Y., Moriga, T., Ashida, T. and Nakabayashi, I., 1996. Synthesis of Vaterite by Carbonation Process in Aqueous System. *Journal of the Ceramic Society of*

Japan, Vol. 104, No. 11, pp. 1081-1084.

McConnell, J. D. C., 1959. Vaterite from Ballycraigy, Larne, Northern Ireland. *Min. Mag.*, Vol. XXXII, pp. 535-545.

Meyer, H. J., 1969. Struktur und Fehlordnung des Vaterits. *Zeitschrift für Kristallographie*, Bd. 128, S., pp. 183-212.

Mikkelsen, A., Anderson, A. B., Engelsen, S. B., Hansen, H. C. B., Larsen, O. and Skibsted, L. H., 1999. Presence and Dehydration of Ikaite, Calcium Carbonate Hexahydrate, in Frozen Shrimp Shell. *J. Agric. Food Chem.*, Vol. 47, No. 3, pp. 911-917.

Nassrallah-Aboukaïs, N., Boughriet, A., Gengembre, L. and Aboukaïs, A., 1998. Manganese(II)/Vaterite/Water Systems: Spectroscopic and Thermodynamic Study. *J. Chem. Soc., Faraday Trans.*, Vol. 94, No. 16, pp. 2399-2405.

Northwood, D. O. and Lewis, D., 1968. Transformation of Vaterite to Calcite During Grinding. *American Mineralogist*, 53<sup>2</sup>, pp. 2089-2092.

Patashinskii, A. Z. and Pokrovskii, V. L., 1979. *Fluctuation Theory of Phase Transitions*. Published by Pergamon Press Limited.

Perić, J., Vučak, M., Krstulović, R., Brečević, Lj. and Kralj, D., 1996. Phase Transformation of Calcium Carbonate Polymorphs. *Thermochimica Acta*, 277, pp. 175-186.

Putnis, Andrew, 1992. *Introduction to Mineral Sciences*. Published by Cambridge University Press.

Rowlands, D. L. G. and Webster, R. K., 1971. Precipitation of Vaterite in Lake Water. *Nature Physical Science*, vol. 229, p. 158.

Schmahl, W. W., Swainson, I. P., Dove, M. T. and Graeme-Barber, A., 1992. Landau Free Energy and Order Parameter Behaviour of The  $\alpha/\beta$  Phase Transition in Cristobalite. *Zeitschrift für Kristallographie*, Vol. 201, pp. 125-145.

Simpson, L. J., 1998. Short Communication: Electrochemically Generated CaCO<sub>3</sub> Deposits on Iron Studied with FTIR and Raman Spectroscopy. *Electrochimica Acta*, Vol. 43, Nos. 16-17, pp. 2543-2547.

Stout, G. H. and Jensen, L. H., 1968. *X-Ray Structure Determination: A Practical Guide*,

Published by Macmillan Publishing Company, Incorporated.

Tarits, C., Leroy, P., Letolle, R. and Blanc, P., 1990. Rapid Vaterite/Calcite Transformation from Supersaturated Solution in Calcium Carbonate. *Academie Des Sciences. Comptes Rendus. Serie II. Mechanique-Physique Chimie*, Vol. 311, Nos. 7-13, pp. 1297-1301.

Tolédano, Jean-Claude and Tolédano, Pierre, 1987. *The Landau Theory of Phase Transitions: Application to Structural, Incommensurate, Magnetic and Liquid Crystal Systems*, pp. 215-227, Published by World Scientific.

Topley, B. and Hume, J., 1928. The Kinetics of The Decomposition of Calcium Carbonate Hexahydrate. *Roy. Soc. Proc., A*, 120, pp. 211-221.

Turrell, G., 1972. *Infrared and Raman Spectra of Crystals*, Published by Academic Press.

Visintin, A., 1996. *Models of Phase Transitions*, Published by Birkhäuser.

Yukhnovskii, I. R., 1987. *Phase Transitions of The Second Order: Collective Variables Method*, Published by World Scientific.

Wells, A. F., 1975. *Structural Inorganic Chemistry, Fourth Edition*, Published by Clarendon Press.

White, W. B., 1974. *The Infrared Spectra of Minerals*, Edited by V. C. Farmer, Published by Mineralogical Society of London, pp. 232-247.

Zhou, D., Anoshkina, E. V., Desai, V. H. and Casey, K. J., 1998. Synthesis and Characterization of Calcium Carbonate Whiskers. *Electrochemical and Solid-State Letters*, Vol. 1, No. 3, pp. 133-135.





